EVALUATION OF UNSTEADY AERODYNAMIC FORCES AND PRESSURE IN WINGS AND TURBINES AT LOW REYNOLDS NUMBER BY COMBINING PARTICLE IMAGE VELOCIMETRY AND PROPER ORTHOGONAL DECOMPOSITION

By

ARTURO VILLEGAS VAQUERO

A dissertation submitted to the

Graduate School—New Brunswick

Rutgers, The State University of New Jersey

in partial fulfillment of the requirements

for the degree of

Doctor of Philosophy

Graduate Program in Mechanical and Aerospace Engineering

written under the direction of

F. Javier Diez

and approved by

_____

_____

_____

_____

New Brunswick, New Jersey

May, 2014

ABSTRACT OF THE DISSERTATION

Evaluation of unsteady aerodynamic forces and pressure in wings and turbines at low Reynolds number by combining particle image velocimetry and proper orthogonal decomposition

By ARTURO VILLEGAS VAQUERO

Dissertation Director:

F. Javier Diez

Aerodynamic unsteady forces in stationary and rotating wings are analyzed in this dissertation by using a combination of time-resolved particle image velocimetry (TR-PIV) and proper orthogonal decomposition (POD) techniques. Recent progress in experimental measurements has demonstrated the use of TR-PIV to calculate forces by applying the integral conservation of momentum equation in its different forms. However, a more accurate and robust method is needed for unsteady forces calculations. With this in mind, a modified pressure Poisson method is developed and applied in this work, showing its superior behavior compared to other methodologies described in the past. The independence of the calculated forces shows the robustness

and stability of the method.

Whereas force calculations have been recently considered, the role of flow structures in force fluctuations has not been revealed yet and it is the main focus of this study. To elucidate these relations, a hybrid PIV-POD analysis is applied to reconstruct the velocity field from the most energetic modes of the flow. A model describing the vortex-force relations is proposed in terms of lift and drag variations during the vortex shedding process. A spectral analysis of the calculated forces suggests symmetric periodic lift, drag and circulation variations at the shedding frequency. Moreover, lift, drag and circulation signals are in phase, which supports lift-circulation proportionality. However, non-symmetric drag fluctuations are found at double the shedding frequency within a shedding cycle. For instance, when a positive or negative circulation vortex detaches, different values in the maximum and minimum drag are obtained.

The data and physical relations obtained in this work such as main frequencies, vortex-force fluctuations and behavior of reduced-order models can aid in the development of CFD applications at low *Re*. The methodology described can be applied to any moving or stationary wing at different Reynolds numbers and angles of attack which would provide additional data for numerical codes. Furthermore, accurate measurements of unsteady forces allow determining narrower and more precise safety margins. Moreover, these measurements could be of application in flow control since forces are related to flow features simultaneously.

Acknowledgments

I would like to thank my advisor, Professor F. Javier Diez. Five years ago, he showed me the importance of research and took me under his tutelage. He has always spent the time and discussed all my questions and concerns which I truly appreciate. He has always been there for me during my doctoral years. I also learned from him many experimental fluid methods as well as how to properly write technical papers. Thank you again for believing in me and transferring many of the skills I have acquired at Rutgers.

I would also like to thank Professor J. Shan, Professor G. Drazer and Professor F. Muzzio for being part of my committee. I would also like to thank Professor W. J. Bottega for his help in the beginning of the first year and Professor A. Cuitino who also helped me in several occasions. Many thanks to Mr. Petrowski, he also was there for me when I needed assistance and spent his time building my models. It was also of great help all the assistance and advice received from the secretaries of the department, I will always be thankful to Ms. Carmen, Ms. Cynthia and Ms. Shefali.

I would also like to thank all my labmates Ye, Tom R., Mariusz, Jon, Andrew, Josh, Dan, Tom H., Mena, Merhnaz, Srinivas, David, Ravi, Ayaz and Marco. They all contribute to expand my knowledge in the field of fluids dynamics. Thank you Ye Cheng for showing me almost everything I know about PIV and becoming a good friend. Many thanks to my good friend Tom Reesbeck for all the good moments we spent together inside and outside the lab, I missed you when you left and still do.

I am very thankful to my departmental mates and friends Billy, Matthew, Marlon,

Mohamed and Sunny. They made my hours inside and outside the department more enjoyable and helped me in many occasions.

Also from the department, I would like to thank Julian, Alina, Herminia and Ruben. I spent some of my breaks having very valuable conversations with them (especially Julian). I will always be in debt with my friends and almost family Julian and Altagracia for their support and all the love they have showed to me.

I want to thank the Spanish Armada (Alberto, Alvaro, Guillermo and Joaquin) for the amazing first year we had at Rutgers. They have always been very good friends of mine and hope this last forever. We had many good times in Spain and US before and many others to come. A special thank is reserved to one of my best friends Joaquin Miranda who first encouraged and brought me to the United States.

I would like to thank all my friends outside the department who were and still are part of my life (Joe, Valerie, Georgina, Jeanette, Arthur, Jorge, Amy, Cristiano, Young, Yasmin, Bomina, Jack, Eva, Jordan, Shannon, Maria, Sarah, Richard, Andrei, Andy, Saltuk, Gokhan...). We had good times indoors (Colony House, Buell apartments, Yosko Dr, poker nights) and outdoors (BBQ's, skiing, beach, trips to NYC and other parts of the US, nights out in NB, Rutgers games). This made my doctorate years incredibly entertaining and fun. A special thank to my best friends and my family here Cevat and Yasir. I cannot imagine a life in Rutgers without you guys. We are and will be brothers forever. I feel so lucky I met Cevat at the beginning of the first year. Many stories since then... All these years, we had infinite talks about courses, research and other non-academic topics of course, but always supporting each other, thank you.

Finally I want to show my biggest gratitude to my family. I could have never been able to reach that far without the love and help from my parents Laureano Villegas and Maria Jesus Vaquero and my sister Sheila Villegas. They have always believed

in me and supported all my dreams. Words are not enough to explain how proud I am of my family.

Dedication

To my parents and sister, who are my source of motivation and inspiration

Table of Contents

List of Tables

List of Figures

Chapter 1

Introduction

1.1 Motivation and goals

Unsteady forces from wings and bluff bodies are of great interest in aerodynamics. Fixed and rotating wings are found in many systems such as airplanes, wind and water turbines, airplane propellers and rotorcrafts among others. The performance of these systems can be characterized by the mean aerodynamic forces and pressure fields created by the wings. Accurate knowledge of these parameters can be used during design and optimization for creating more efficient systems. In some instances, information about the mean forces and pressure might not be sufficient to define the working conditions, especially in cases with time variations in lift and drag. In those cases, instantaneous forces and pressures differ from the mean values and they need to be resolved. Those time variations can occur due to vortex shedding, stall conditions and flow separation among others. Measurement of instantaneous forces could capture these processes and provide an accurate estimation of the wing or blade load fluctuations. Particle image velocimetry (PIV) is suitable to perform this task after post-processing the data acquired. Some authors have recently attempted to calculate instantaneous forces around different objects by using this technique. However, all different methodologies are more or less suitable depending on the application and a more general and accurate method is needed. The first goal of this dissertation is to provide a methodology to accurately calculate instantaneous and mean pressure and

forces in fixed and rotating wings.

The knowledge of the amplitude and dominant frequencies of those force fluctuations is important when designing and sizing unsteady systems and allows determining more accurate safety margins and materials for the structure. However, knowing the phenomenon that causes those fluctuations is more important in order to predict force behaviors. In addition, flow control could be used more efficiently when the physical relations between forces and flow features can be associated simultaneously. More specifically, at low Reynolds numbers (Re), the laminar boundary layer separation is common due to the flow's inability to resist adverse pressure gradients (Fitzgerald & Mueller, 1990), generating vortex shedding in the wake such as the Kármán vortex street. The separated boundary layer is highly unstable and will initiate transition quickly, generating vortex shedding. Some authors have experimentally studied the unsteady wake of different airfoils in the presence of vortex shedding and shear layer separation at high (Bourgoyne *et al.*, 2005) and low (Yarusevych *et al.*, 2006, 2009; Boutilier & Yarusevych, 2012) Re for fixed airfoils and starting wings (Huang *et al.*, 2001). In addition, numerical simulations have been performed over cylinders (Dong *et al.*, 2006), circular disks (Shenoy & Kleinstreuer, 2008) or spheres (Rodriguez *et al.*, 2011) to describe the near wake flow structures. Power spectral density (PSD) of the velocity components is often used to detect structures and frequencies in the separated shear layer and wake of the airfoil (Pope, 2000). Moreover, these studies extract and represent coherence structures by using different vortex identification methods such as Q -method (Hunt *et al.*, 1988), Δ -method (Chong *et al.*, 1990) or λ -method (Jeong & Hussain, 1995). However, the three methods are identical for planar measurements and just the first one is considered in this manuscript. While previous work (Bourgoyne *et al.*, 2005; Yarusevych *et al.*, 2009; Boutilier & Yarusevych, 2012) have focused in identifying flow structures and dominant frequencies in a selected range of Re and angle of attacks (α), they do not account for any relation between

vortices and force fluctuations. The study of that relationship is the second goal of this dissertation.

Additionally, aerodynamics and wake structure of wind turbines have been widely studied numerically and experimentally. However, mid- to high-Re number wind turbines are the main object of those studies and few data is available at low-Re. Low-Re can be found in water turbines as well as small wind turbine for urban areas. These are products in a market that is currently expanding and more information is needed. The third goal of this dissertation is to provide useful data such as vortex shedding frequencies, force fluctuations and behavior of low-dimensional models at low Re.

1.2 Review of aerodynamic theory and force calcualtions

1.2.1 Fundamental aerodynamics

Aerodynamic forces on bodies are due to the interaction between the body and the fluid. Physically, the aerodynamic force on the body is only due to pressure (p) and shear (τ) distribution on the surface of the body. Figure 1.1a shows the pressure and shear at a point B on the surface of an airfoil. The pressure acts perpendicular to the surface, while the shear acts tangent to it. The integration of pressure and shear around the surface (s) of the body gives the resultant aerodynamic force. The total normal (N) and tangential (A) forces per unit length (see Fig. 1.1b) are given by

$$N = -\int_{LE}^{TE} (p_u \cos\theta + \tau_u \sin\theta)\, ds_u + \int_{LE}^{TE} (p_l \cos\theta - \tau_l \sin\theta)\, ds_l \tag{1.1}$$

$$A = \int_{LE}^{TE} (-p_u \sin\theta + \tau_u \cos\theta)\, ds_u + \int_{LE}^{TE} (p_l \sin\theta + \tau_l \cos\theta)\, ds_l \tag{1.2}$$

where subscripts u and l mean upper and lower respectively and θ is the angle between the chord of the body and a point at the surface measured clockwise. When the airfoil pitches at certain angle of attack (α), the lift (L) and the drag (D) are then given by (see Fig. 1.1b)

$$L = N\cos\alpha - A\sin\alpha \tag{1.3}$$

$$D = N\sin\alpha + A\cos\alpha \tag{1.4}$$

Even though pressure and shear on the surface are the only mechanism that causes aerodynamic forces, the generation of those distributions are influenced by the flow surrounding the body. The understanding of how forces are affected by instabilities such as vortex shedding is of great interest and it is studied in this manuscript.

To calculate instantaneous forces and observe vortex shedding patterns simultaneously, a technique such as PIV can be used after the right treatment of the obtained velocity data. Forces are calculated from velocity and its temporal and spatial gradients by using the conservation of momentum equation. Experimentally, instantaneous measurements of the whole pressure and shear distributions at the surface of the airfoil are not available most of the time due to the resolution needed to capture the boundary layer. Moreover, the calculation of forces using this method (Eqs. 1.1 and 1.2) do not reveal the role of the flow surrounding the airfoil with the instantaneous forces. However, from the Newton's second law, the integral momentum equation can be derived for a Newtonian fluid flow over a fluid control volume (Anderson, 2001)

$$\frac{\partial}{\partial t}\iiint_V \rho\vec{u}dS + \iint_S \rho\vec{u}\left(\vec{u}\cdot\vec{n}\right)dL = -\iint_S \left(p\cdot\vec{n}\right)dL + \iint_S 2\mu\overline{\overline{\sigma}}\vec{n}dL \tag{1.5}$$

where ρ is the fluid density, μ is the kinematic viscosity, $\vec{u}$ is the velocity vector, p

is the pressure, $\overline{\overline{\sigma}}$ is the stress tensor, V is the volume of fluid and S is the surface of the control volume. In Sec. 2.6, this equation is applied to a control volume surrounding the airfoil to obtain the instantaneous forces. In addition, the differential momentum equation can be obtained by applying the gradient and divergence theorems (Anderson, 2001)

$$\nabla p = -\rho \left(\frac{\partial \vec{u}}{\partial t} + \vec{u} \cdot \nabla \vec{u} \right) + \mu \nabla^2 \vec{u} \tag{1.6}$$

This is the Navier-Stokes equation and relates variables at every point of the flow field. It can be used to determine the pressure gradient only from velocity and velocity gradient measurements.

1.2.2 Blade element momentum theory

The blade element momentum theory (BEMT) is widely used for estimating aerodynamic forces during the wind turbine design (Burton, 2011). It is the result of coupling the *1D* momentum theory (MT) and the blade element theory (BET). Several corrections to the theory have been incorporated to address some 2D and 3D effects such as Prandtl correction (Prandtl & Betz, 1927) for tip- and hub-losses as well as the Glauert correction (Glauert, 1935) for differences observed between theory and experiments beyond a certain axial induction factor number. There are also finer corrections developed more recently which are modifications of the two corrections mentioned above (Shen *et al.*, 2005). BEMT is used in this dissertation to design an aerodynamically optimum wind turbine for maximum power extraction. However, the BEM theory does not provide information about the variations of instantaneous forces or pressure fields when vortex shedding is present and previous information about the lift and drag coefficients of the airfoil is needed to solve for these forces.

The BEMT is briefly presented in this dissertation and a complete derivation can be found in Burton (2011). By equating the MT normal force per unit length to the BET normal force and also equating the MT torque per unit length to the BET torque, a system of two-equations and two unknowns is obtained

$$\frac{a}{1-a} = \frac{\sigma_r}{4f}\left[\frac{C_l\cos\phi + C_d\sin\phi}{\sin^2\phi}\right] \tag{1.7}$$

$$\frac{a_t}{1+a_t} = \frac{\sigma_r}{4f}\left[\frac{C_l\sin\phi - C_d\cos\phi}{\sin\phi\cos\phi}\right] \tag{1.8}$$

where the two unknowns variables are the axial velocity induction factor (a) and the tangential velocity induction factor (a_t). Also, σ_r is the local solidity of the blade, C_l is the local lift coefficient, C_d is the local drag coefficient, ϕ is the inflow angle and f is the Prandtl correction factor. In addition, Glauert correction is introduced for axial induction factors higher than the critical value $a_c = 0.4$. An iterative process is applied to solve for a and a_t. For all cases, the least-squared method is used to resolve the 2-equations system and the relative residual is less than $1e^{-10}$. Figure 1.2a shows the angles and velocities on a blade radial station. The total velocity W at every radial section of the blade is given by

$$W = \sqrt{U_\infty^2(1-a)^2 + \Omega^2 r_z^2(1+a_t)^2} \tag{1.9}$$

where U_∞ is the upstream velocity, Ω is the rotor rotational speed and r_z is the radial location along the blade span. As shown by Fig. 1.2b, the local tangential (F_t) and normal (F_n) forces per unit length can expressed as a function of the lift (L) and drag forces (D)

$$F_t = L\sin(\phi) - D\cos(\phi) \tag{1.10}$$

$$F_n = L\cos(\phi) + D\sin(\phi) \tag{1.11}$$

$$L = 1/2\rho c W^2 C_l \tag{1.12}$$

$$D = 1/2\rho c W^2 C_d \tag{1.13}$$

where ρ is the density of the fluid and c is the cord of the airfoil. Results from Eqs. 1.10 and 1.11 are used for comparison with experimental measurements in their non-dimensional form as the local tangential (C_t) and normal (C_n) force coefficients

$$C_n = \frac{2F_n}{\rho c\left(U_\infty^2 + (\Omega r_z)^2\right)} \tag{1.14}$$

$$C_t = \frac{2F_t}{\rho c\left(U_\infty^2 + (\Omega r_z)^2\right)} \tag{1.15}$$

The turbine used in the present study was design for optimal rotor blade twist and cord distribution for maximum power using BEMT and it is discussed elsewhere (Villegas *et al.*, 2010). In addition, lift and drag coefficients were calculated using XFOIL (Drela, 1989).

XFOIL (Drela, 1989) is a simulation module especially suitable for analysis of Low *Re* number airfoil flows with separation bubbles (which is the case of study in this dissertation). An inviscid linear-vorticty panel method is used to calculate the potential flow. The effect of the viscous layers on the potential flow are modeled by a 2-equation lagged method represented by a superimposed distribution of sources in the airfoil and the wake. Additionally, the laminar and turbulent boundary layers

are addressed as well as the transition point with an $e^9 -$ type amplification formulation. Both boundary layer and transitional equations are solved simultaneously by a global Newton method. A full description of the method is discussed elsewhere (Drela, 1989).

1.3 Review of numerical evaluation of forces

Numerically, full simulations are only available for very small number of simplified cases due to the high computational cost of direct numerical simulation (DNS). Approximate numerical models such as Reynolds-Averaged Navier-Stokes (RANS) models are typically used to calculate the mean velocity and mean pressure field (Hansen *et al.*, 2006). For three-dimensional flow with moving elements (i.e. blades in wind turbines), these computations become more expensive in terms of code, mesh, and calculations. Sezer-Uzol & Long (2006) simulated a full scale 2-bladed wind turbine using a 3D time accurate algorithm, in which they show the pressure distribution on the surface of the blades. Bazilevs *et al.* (2011*a*,*b*) performed a 3D simulation of a wind turbine at full spatial scale and validating it against published experimental data from the National Renewable Energy Laboratory (NREL).

A current DNS study performed by Wang *et al.* (2013), investigated the differences between instantaneous lift from a derived momentum equation formula and the quasi-steady Kutta-Joukowski formula for a stationary and flapping rectangular flat plate, neglecting pressure effects just for very large control volumes.

In addition, Wu *et al.* (2007) analyzed two numerical solutions of unsteady and viscous circular-cylinder flows. The vorticity momentum approach is used in this study in both advective and diffusive forms. Results confirm the suitability of keeping all the derivative terms inside the integral to find relations between flow structures and

forces for numerical simulations. However, as we will see in the result sections, this approach is not suitable for experiments due to error propagation and a barely satisfied continuity equation. In addition, the phase of the forces is unclear when using this methodology for different control volume sizes for these experiments, which makes the relationship between forces and vortices ambiguous.

1.4 Review of experimental evaluation of forces

Experimentally, considerable work has been done in designing and testing wind turbines (Hansen *et al.*, 2006; Burton, 2011; Hand *et al.*, 2001; Simms *et al.*, 2001). In terms of pressure measurements, Hand *et al.* (2001) and Simms *et al.* (2001) compared results from tap sensors to the predicted numerical simulations. In addition, Tangler (2002) performed an evaluation of the BEM theory against a lifting-surface model and experiments. Forces are usually measured with a balance and the pressure is measured with arrays of pressure taps embedded in the turbine surface in the past. These are both intrusive instruments which are mounted on the turbine and can affect the flow. Furthermore, force balances are generally limited to wind tunnel applications, and pressure gauges are intrusive and often single point measurements, which limits its application. For the wake of the airfoil, a widely used technique for measuring the pressure is the hot wire anemometry. However, it is also an intrusive single point measurement technique difficult to implement for rotating wind turbines. Therefore, although there has been a significant amount of progress in evaluating forces and the pressure field for turbines, their performance characteristics are still not fully resolved due to the lack of non-intrusive 2D and 3D high spatial and temporal resolution measurement techniques.

Recently, non-intrusive PIV technique (Westerweel, 1997; Adrian, 2005) has been used to evaluate forces around objects. PIV is suitable to calculate flow velocity

fields and corresponding spatial and temporal derivatives with high resolution. These derivatives can be used in the differential and integral formulation of the momentum and mass conservation equations to solve for the pressure field and forces. Unsteady forces in fixed and moving airfoils and bluff bodies have been calculated by some authors from time resolved particle image velocimetry (TR-PIV) velocity fields. Most of the theoretical work was initiated by Wu (1981) and Lighthill (1986) with the introduction of the vorticity moment concept for calculating forces without the need of calculating the pressure term and applied experimentally by Lin & Rockwell (1996). That work was further developed by Noca *et al.* (1999) to account for finite control volumes and used in several PIV applications. One of his major findings was the evaluation of forces without the need of volume integrals. However, the moment of velocity and vorticity introduced in these methods suffers from moment arm errors, giving inconsistent results for small force coefficients and large control volumes (Noca *et al.*, 1999). At the same time, Unal *et al.* (1997) used the integral momentum approach to calculate the pressure term through spatial integration of the pressure gradient. Nevertheless, this later approach also produces large source of errors, due to error propagation in the integration path. Since an accurate calculation of the pressure was needed, many authors started looking for other ways of obtaining the pressure. Gurka *et al.* (1999) calculated the pressure by solving the pressure Poisson equation (PPE) from PIV measurements. Another method of calculating the pressure term was proposed by Baur & Kngeter (1999) through spatial integration of the pressure in 4 directions and taking the averaged value to decrease the directional error. Liu & Katz (2006) used an omnidirectional virtual boundary integration scheme of the material acceleration to calculate the instantaneous pressure. Charonko *et al.* (2010) discussed the challenges in obtaining pressure from time dependent flows and showed the differences between the omnidirectional and PPE approaches in their different ways for different flows. The effects of grid resolution, sampling frequency,

velocity error and out-of-plane velocities were tested in this work for synthetic flows. In addition, they found that the PPE method was more accurate for external flows and the omnidirectional integration more suitable for internal flows. Additionally, de Kat & van Oudheusden (2011) determined instantaneous pressure fields from PIV measurements in turbulent convected flows and gave some guidelines for temporal and spatial resolution to successfully determine the pressure. A synthetic flow and an experiment over a stationary square cylinder were tested to validate these proposed guidelines. In de Kat & Ganapathisubramani (2013), a new approach for pressure estimation in convective turbulent flows is proposed by a combination of volumetric or time-resolved cross-plane measurements with Taylor's hypothesis. In this study, the elimination of the time derivative when obtaining the pressure gradient reduces the error in the calculated pressure.

Recent studies use the methods described above to calculate forces from PIV measurements. Mean forces from PIV have been calculated for many cases such as cylinders (Fujisawa *et al.*, 2005; Oudheusden *et al.*, 2007), airfoils (Ragni *et al.*, 2009; Lee & Su, 2012), propellers (Ragni *et al.*, 2011) or wind turbines (Murai *et al.*, 2007; Villegas & Diez, 2014*b*). However they do not account for fluctuations of the forces. Moreover, Villegas & Diez (2014*b*) showed the importance of the local acceleration term in moving frames of reference when calculating mean forces. Instantaneous forces have been also calculated by considering the acceleration term from TR-PIV measurements over fishlike swimming bodies (Wu *et al.*, 2005), square cylinders (Kurtulus *et al.*, 2006), asymmetric hovering flapping wings (Jardin *et al.*, 2009), flat plates (Mohebbian & Rival, 2012). In these studies, the pressure term is calculated from direct integration of the pressure gradient. Furthermore, Mohebbian and Wu used a derived momentum equation which only needs to be evaluated at the boundaries of the control volume. However, they found large sources of error when the vortices passed across the boundaries. A recent study by Villegas & Diez (2014*a*) shows the capabilities of

a modified PPE in calculating instantaneous unsteady forces in rotating wings with vortex shedding.

1.5 Dissertation outline

The present work investigates the experimental evaluation of unsteady aerodynamic forces from PIV measurements and POD analysis as well as the relations between those forces and flow structures.

The introduction chapter (Ch. 1) reviews the different theoretical, numerical and experimental methods used in the literature to calculate mean and instantaneous forces in aerodynamics.

The methodology chapter (Ch. 2) describes the different theories, mathematical tools and error analysis in calculating pressure and forces from PIV measurements. It also explains the design of the water turbine and experimental conditions. Three different experiments are conducted in this work, a high-rpm water turbine, a low-rpm water turbine and a stationary wing. They will be referred as *Case 1*, *Case 2* and *Case 3* respectively.

Results are shown in chapters 3-6 for all three cases and for both raw and POD data. Chapter 3 shows and analyzes velocity and vorticity fields in the presence of vortex shedding. Chapter 4 shows and analyzes local and convective acceleration fields for both stationary and moving frames of reference. Chapter 5 shows and analyzes the pressure obtained by the modified pressure Poisson equation and it is compared to both spatially integrated pressure and Bernoulli methods. Chapter 6 contains the evaluation of unsteady forces. This chapter analyzes in detail the contribution of each term to the total force contribution as well as the independence and robustness of the method compared to other approaches in the literature. In addition, the relationship

vortex-force is disclosed in this chapter too.

The last chapter (Ch. 7) states the main contributions of this work and gives some future work guidelines.

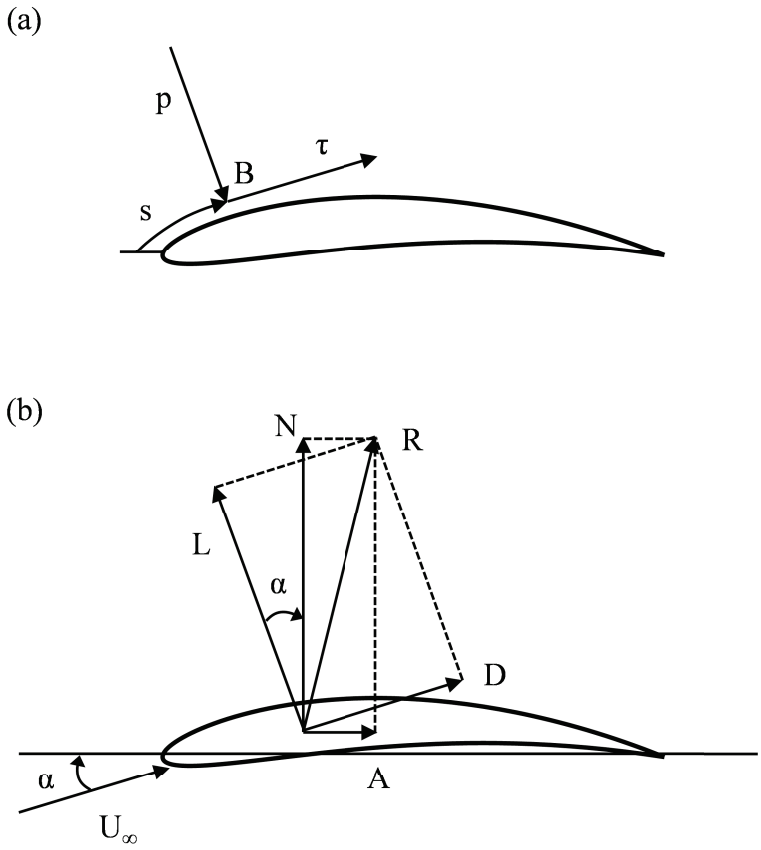

Figure 1.1: (a) Pressure and shear on an airfoil and (b) components of the aerodynamic force

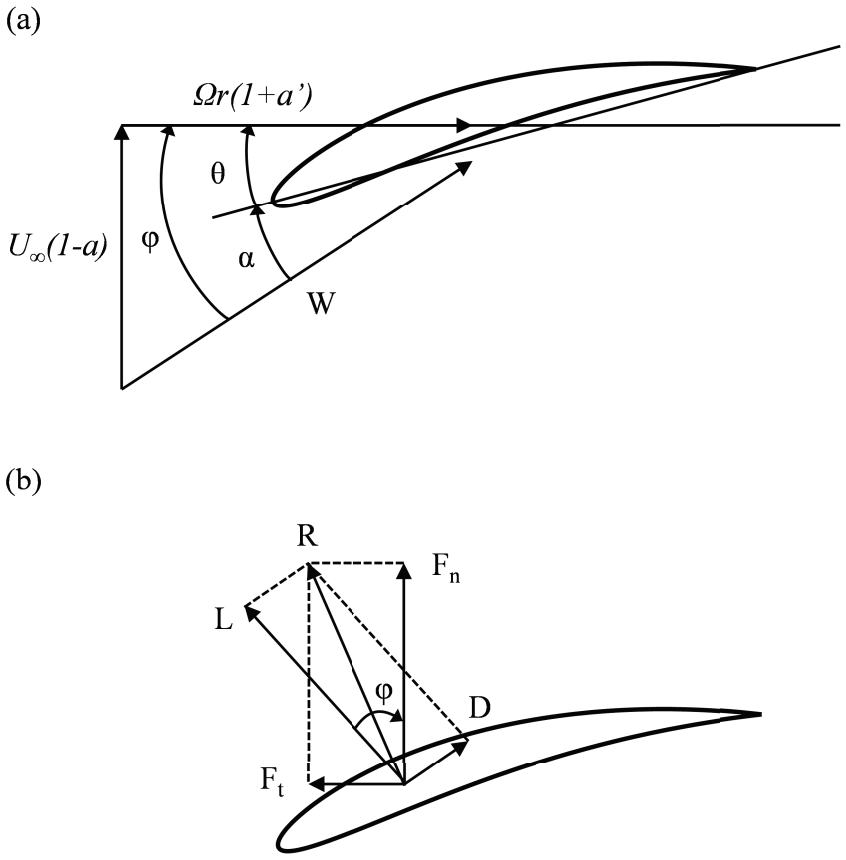

Figure 1.2: (a) Angles and velocities on a blade radial station used in the BEM theory and (b) components of the aerodynamic force

Chapter 2

Methodology

2.1 Wind turbine design

As explained in Sec. 1.2.2, BEM theory is used to design the turbine model that will be tested during the present work as well as to predict mean forces. The theory was implemented in Maltlab and the code was validated by comparing the results to the experimental data (Giguere & Selig, 1999) from one of the National Renewable Energy Laboratory wind turbine designs (Hand *et al.*, 2001). This validation is shown in Fig. 2.1, where the thrust force is shown for both theory and experiments versus change in the upstream velocity. The theoretical thrust is obtained by two different methods. The classic curve is the BEM theory without any corrections. The Prandtl-Glauert curve accounts for tip and hub loss corrections as well as the Glauert correction for a critical axial induction factor value $a_c = 0.4$. There is an excelent agreement between theory and experiments up to high values in the upstream velocity, where stall conditions may be presented and the breakdown of the theory may occur. Other corrections such as Viterna & Corrigan (1982) could improve the behavior of the theory at higher free stream velocities.

After validation of the code, the new turbine was designed for maximum power extraction (inverse design). The process involved several iterations and surface optimization by a parametric study of the different variables involved. The NACA8512 airfoil was selected. The twist angle distribution along the blade span was optimized

for $U_\infty = 0.1\,m/s$ and $\Omega = 1.8\,s^{-1}$, giving a design tip speed ratio $\lambda = 4$. The design lift coefficient based on the maximum lift to drag ratio at $Re = 11000$ is $C_l = 0.66$ at the angle of attack $\alpha = 5\,^\circ$. The drag coefficient at the same angle of attack is $C_d = 0.12$. Table 2.1 shows the optimized twist distribution.

2.2 Experimental analysis

Experiments in this paper are conducted in a recirculating water tunnel with a 0.9×0.5 m^2 test section. Two sets of honeycombs and flow straighteners are placed upstream of the test section to ensure laminar flow conditions with turbulence levels below 0.1%. The water is seeded with 8-12 μm neutrally-buoyant hollow glass spheres with a 1 g/cm^3 density. For these studies, a low Reynolds number water turbine is designed with a NACA8512 airfoil-shaped blade as well as a fixed wing with the same airfoil. The two-bladed turbine has a 188 mm radius (R) with a varying blade chord length and twist angle for improved efficiency. The turbine is mounted on a low-friction bearing facing the flow direction.

A PIV system is used to measure the velocity field around the blade. The system, sketched in Fig. 2.2, consists of a Nd:YAG laser, a set of cylindrical and spherical lenses and mirrors to deliver the laser sheet to the test section and a low or high speed camera to capture the PIV image. PIV images are analyzed using Insight 3G v.10 software by TSI Inc. The main parameters for processing the images include using a 24×24 px^2 interrogation window with 50% overlap. As part of the post-processing of the calculated velocity field we applied a typical local median 5×5 vector replacement filter and a local mean 3×3 vector filling filter to replace any bad vectors. The percentage of outliers and replaced vectors was less than 1.5% for all instantaneous velocity fields. The PIV data acquisition is phase-locked with a fixed azimuthal blade position so that PIV images are always taken at the same exact

location. This is achieved by an optical laser light switch being triggered by the blade crossing its beam path.

To solve for the pressure field and forces created by the turbine, the velocity field needs to be resolved simultaneously around the entire cross-section of the blade. This presented a challenge when illuminating the field of view with the laser sheet since the wind turbine blade partially blocks the light and a shadowed region appear in the field of view. To minimize shadows in the complex areas of the flow, the laser sheet was oriented to fully resolve the wake but produced a small shadow region near the leading edge of the blade as sketched in Fig. 2.2. The velocity in that region is calculated by linear interpolation from surrounding vectors. In addition, reflections from the laser affected the results close to the airfoil. This was notably reduced by painting the rotor blades with a mix of Rhodamine 6G, ethanol and urethane in combination with placing a narrow band 532 nm filter in front of the camera.

Three different experiments are conducted in this work. Table 2.2 shows the main differences between the three experiments. In the first experiment (*Case 1*), the turbine is driven at 52 rpm and the flow Reynolds number based on the mean cord (c) is $Re_c = 25000$. *Case 1* is performed by using a regular 2D-PIV system and, therefore, no time-resolved velocity fields are obtained. However, a new methodology to calculate the acceleration term in stationary frames of reference for steady airfoils is developed in this study. This methodology is explained by the timing diagram shown in Fig. 2.3. Briefly, the PIV system captures, after a known trigger time delay, two images at t_1 and t_2. This generates the first velocity field $\vec{v}_1$. Next the PIV system captures, after a slightly larger trigger time delay, another two images at t_1' and t_2'. This generates the second velocity field $\vec{v}_1'$. As a result of this variation in trigger delay ($\Delta t = 0.0036\,s$), the blade position appears displaced a few pixels between the field of views for $\vec{v}_1$ and $\vec{v}_1'$ which are used to obtained the local acceleration. In the

second experiment (*Case 2*), the turbine is driven at 20 rpm and the flow Reynolds number based on the mean cord is $Re_c = 11000$. *Case 2* uses a time-resolved 2D-PIV system and time-resolved velocity fields are obtained. In addition, the wake of this turbine shows a developed periodic instability, forming the vortex shedding street. The high temporal resolution of the TR-PIV resolves the vortex shedding. Since the airfoil is moving through the field of view, the spectral analysis of the velocity signal is limited in frequency range and resolution. Therefore, weak peaks in the PSD analysis does not precisely reveal vortex structures. However, a phase-averaged POD analysis of the flow identifies those structures as well as creates continuous functions in time for the calculated forces. In the third experiment, a fixed wing is immersed in a flow with $Re_c = 3900$. *Case 3* also uses the TR-2D-PIV system. In this case, the spectral analysis is available since longer time series can be recorded and vortex structures are obtained. A full POD analysis is applied to this case to identify structures and main frequencies.

2.3 Frame of reference

The governing equations of the flow over a rotating wind turbine can be written either in a reference frame that moves with the blade (moving frame) or in a reference frame fixed with the ground (stationary frame). In a moving frame and in the absence of unsteady effects, the quasi-steady hypothesis applies and the time derivative of the velocity field can be neglected from the equations (Ragni *et al.*, 2009). On the other hand, in a laboratory frame such as in the present work, even in the absence of unsteady effects, the unsteady acceleration term cannot be ignored. The reason for the differences observed in the unsteady accelerations between the two reference frames can be explained (Kundu *et al.*, 2012) as discussed by relating the accelerations

in inertial and non-inertial ($'$) frames of reference as

$$\frac{\partial \vec{u}}{\partial t} + \vec{u} \cdot \nabla \vec{u} = \frac{\partial \vec{u}'}{\partial t} + \vec{u}' \cdot \nabla \vec{u}' + 2\vec{\Omega} \times \vec{u}' + \vec{\Omega} \times \left(\vec{\Omega} \times \vec{r}' \right) \tag{2.1}$$

where $\vec{x}$ and $\vec{u}$ are the fluid particle position and velocity respectively, $2\vec{\Omega} \times \vec{u}'$ is the Coriolis acceleration and $\vec{\Omega} \times \left(\vec{\Omega} \times \vec{r}' \right)$ is centripetal acceleration. An observer in the rotating frame would need to consider the four terms in the right hand side of the equation, but the first one is negligible for steady flows as shown in Appendix A. On the other hand, an observer in the fix frame only needs to consider the two terms in the left hand side of the equation, the convective acceleration and the unsteady acceleration. However, this last term requires the evaluation of the time derivative of the velocity which is not zero as shown in Appendix A. This proof the importance of the unsteady acceleration in the inertial reference frame (fix frame) when fluid motion over a rotating wind turbine is considered. Additionally, the proposed method opens the possibility to experimentally evaluate the instantaneous flow pressure field and forces in wind turbines in unsteady flow cases such as stall conditions, flow separation, and strong wake vortex shedding among others. This would not be possible without calculating the unsteady acceleration even if measurements were performed in a non-inertial reference frame (rotating frame).

2.4 Proper orthogonal decomposition

As stated by Charonko *et al.* (2010) and observed in the present manuscript, errors in the measured velocity makes instantaneous pressure and force calculations a very difficult task for any of the method described earlier. Therefore, unsteady forces calculations will be affected by those errors, sometimes leading to a difficult interpretation of the results. In their paper, the authors tested different techniques to

filter the velocity fields before the calculation of the pressure. They found the smallest errors when using the proper orthogonal decomposition method (POD), which is the method used in the present work. POD (Lumley, 1967; Sirovich, 1987; Berkooz *et al.*, 1993) has been applied successfully in many TR-PIV applications to identify flow patterns and extract low dimensional representations of the dynamics of the flow such as swirling flows (Graftieaux *et al.*, 2001), jets (Bi *et al.*, 2003; Schmid *et al.*, 2012), cylinders under jet control (Feng *et al.*, 2011) or engine flows (Chen *et al.*, 2012).

In fluid dynamics, the Proper Orthogonal Decomposition is generally used to extract the most energetic modes of the flow in terms of kinetic energy. These modes represent unsteady structures in the flow and they are physically related to their fluctuating kinetic energy. Velocity fluctuations are used to calculate the fluctuating kinetic energy. POD modes form a new orthogonal base that maximizes the projection of the kinetic energy into a new coordinate system which is mathematically optimal in terms of energy to represent the velocity. POD is often used to partially reconstruct the flow field by just using the most energetic modes, filtering out the noise and small perturbances contained in less energetic ones. The snapshot POD method (Sirovich, 1987) is commonly used for PIV data sets and briefly reproduced here. The correlation matrix C contains the cross-correlation of all instantaneous velocity fluctuation fields

$$C = V^T V \tag{2.2}$$

where V is the matrix containing N instantaneous fluctuating velocity fields. Then, the eigenvalue problem is solved by diagonalizing C

$$C \cdot e = \lambda \cdot e \tag{2.3}$$

where e and λ are the eigenvectors and eigenvalues of C respectively. All eigenvectors are ordered by decreasing value of their respective eigenvalues to ensure the appropriate choice of the modes with the highest energy. Basis functions are obtained by the transformation of the data with the n^{th} mode

$$\phi_n = \sum_{j=1}^{N} V^j e_j^n, \quad n = 1, ..., N \tag{2.4}$$

Basis functions just depend on the position, being independent of time. If a partial reconstruction of the flow is required, time dependent POD coefficients are calculated by

$$a_n^j = \phi^n V^j, \quad n = 1, ..., N, \quad j = 1, ..., N \tag{2.5}$$

Then, each fluctuating velocity field can be reconstructed by just using the first M most energetic modes

$$V_j^* = \sum_{n=1}^{M} a_n^j \phi^n \tag{2.6}$$

Typically, more than 90% of the cumulative energy and modes with no less than 1% relative energy should be included when representing low order estimations of the flow dynamics (Holmes *et al.*, 1998). Once the velocity field is reconstructed, the airfoil forces originated from both original and reconstructed fields are calculated as shown in Section 2.6.

Additionally, a reconstruction in time is possible from non time-resolved PIV data by using a POD analysis. This temporally resolves the flow when the first two modes are dominant such as the case of vortex shedding (Oudheusden *et al.*, 2005). By comparing a Fourier expansion of the phase averaged velocity and the POD reconstruction

by using the first two modes, velocity fluctuations can be modeled as

$$\vec{u}\left(\vec{x},\varphi\right) = a_1\left(\varphi\right)\phi_1\left(\vec{x}\right) + a_2\left(\varphi\right)\phi_2\left(\vec{x}\right) \tag{2.7}$$

where POD coefficients are now given by

$$a_1\left(\varphi\right) = \sqrt{2\lambda_1}\sin\varphi \tag{2.8}$$

$$a_2\left(\varphi\right) = \sqrt{2\lambda_2}\cos\varphi \tag{2.9}$$

where λ_1 and λ_2 are the first and second eigenvalues respectively, and φ is the phase angle. Since the calculation of forces involves temporal derivatives, the corresponding time can be calculated from the shedding frequency as

$$t = \frac{\varphi}{2\pi f_{shed}} \tag{2.10}$$

This methodology is just suitable when one shedding frequency is dominant. In addition, this low order model is continuous in time (phase), allowing time interpolation of the data and increasing the time resolution. However, any information about higher or smaller frequencies is lost in the process. This model reconstructs the velocity field from POD for the case of the water turbine, since the temporal information is limited even when TR-PIV is applied due to rotation of the blades. Once the velocity field is approximated by this model, airfoil forces are calculated as explained in Sec. 2.6.

2.5 Pressure calculation

Calculation of pressure is needed before computing forces by using the integral momentum equation. Pressure fields are obtained by solving the pressure Poisson equation (PPE) given by the divergence of the Navier-Stokes equation (Eq. 1.6), where

all the terms are known from TR-PIV measurements. The PPE can be written as

$$\nabla^2 p = -\rho \left(\nabla \left(\vec{u} \cdot \nabla \vec{u} \right) + \frac{\partial}{\partial t} \left(\nabla \cdot \vec{u} \right) \right) \tag{2.11}$$

Considering that a 2D-like flow is observed along most of the blade and only near the tip the flow is fully 3D, the out of plane component of the velocity (z-direction in Fig. 2.2) is expected to be small. Nevertheless, the continuity equation is not satisfied when missing the small contribution of that third velocity component. In addition, the continuity equation is unlikely to be exactly satisfied experimentally even for a 2D flow. For accuracy in the convergence, the PPE needs the continuity equation to be satisfied for incompressible flows. As discussed by Abdallah (1987) and Sotiropoulos & Abdallah (1991), this can be achieved by including the time derivative of the continuity equation, given by the last term in Eq. 2.11.

To solve the instantaneous pressure field from Eq. 2.11, the equation is first discretized onto a 2-dimensional rectangular grid using a 5 point stencil finite difference scheme. Neumann boundary conditions are used for both external and immersed boundary conditions. These boundary conditions are given by the pressure gradients at the outer edges of the image domain and at the inner edge near the blade surface. They are obtained from the Navier-Stokes equation

$$\nabla p = -\rho \left(\frac{\partial \vec{u}}{\partial t} + \vec{u} \cdot \nabla \vec{u} \right) + \mu \nabla^2 \vec{u} \tag{2.12}$$

The inner boundary near the blade needs to be properly identified before resolving Eq. 2.11. This is done by masking the blade in the images before PIV processing so that the area inside the mask is assigned zero value after PIV processing. Then, Eq. 2.11 can be resolved everywhere within the discretized 2D rectangular grid except where the mask was defined by the zero value. The edges of the mask correspond

to the geometry of the inner boundary condition. This process allows defining inner boundary for complex geometry such as turbine blades.

Neumann boundary conditions are obtained by calculating the pressure gradient from Eq. 2.12 since all velocity terms in the right hand side are derived from TR-PIV measurements. First two terms in the right hand side representing the local and convective acceleration provide the largest contribution to the pressure gradient. The third term is the viscous diffusion and is negligible compared to the other two terms (two orders of magnitude smaller).

Once boundary conditions are known, the instantaneous pressure field is solved from the discretized Eq. 2.11. An iterative least-squared method is used to solve the system of linear equations

$$\begin{pmatrix} a_{11} & \dots & a_{1n} \\ \vdots & \ddots & \vdots \\ a_{m1} & \cdots & a_{mn} \end{pmatrix} \begin{pmatrix} p_1 \\ \vdots \\ p_n \end{pmatrix} = \begin{pmatrix} b_1 \\ \vdots \\ b_n \end{pmatrix} \tag{2.13}$$

where $\vec{p}$ is the pressure vector containing all elements (n) in the discretized domain. Boundary conditions are included in the right hand side $(\vec{b})$. A is the matrix containing the coefficients of the second order derivatives of the Laplace operator. The least-squared method attempts to find $\vec{p}$ that minimizes norm$(\vec{b} - A \cdot \vec{p})$. The pressure field calculated by this method is referred as p_{lsqr} in this manuscript.

To validate the numerical procedure in obtaining the pressure field from the PPE, a comparison with an exact known solution is performed. The next PPE for a rectangular domain is known to have an exact solution

$$\nabla^2 p = -8\pi^2 \cdot \cos(2\pi \mathrm{x}) \cdot \cos(2\pi \mathrm{y}) \quad 0 \leq x \leq 1 \quad 0 \leq y \leq 1 \tag{2.14}$$

where x and y are the position coordinates of the grid element. Neumann boundary conditions are applied to the external boundaries ($\nabla p = \vec{0}$). In addition the domain is discretized by a 48×48 elements to simulates experimental conditions. Numerical solutions are compared to the exact solution given by

$$p_{exact} = \cos(2\pi x) \cdot \cos(2\pi y) \tag{2.15}$$

Since the domain does not contain any inside boundaries, the solution can be calculated from the direct inversion method as well. The direct inversion method for a rectangular domain calculates the pressure by diagonalizating the next problem

$$[Dx][p] + [p][Dy]^T = [rhs] \tag{2.16}$$

where Dx refers to the second order derivative operator in the x-direction and Dy refers to the second order derivative operator in the y-direction. The pressure field calculated by this method will be referred as p_{direct}.

To test the influence of error propagation, the pressure is also calculated after adding noise to the right hand side of Eq. 2.14 (simulating noise in the velocity gradients). Results from the two methods and the exact solution are shown in Fig. 2.4. Figures 2.4a and 2.4b show the pressure obtained from the least-squared method for the original case and the case in which a random 5% noise is added to the right hand side respectively. Figures 2.4c and 2.4d show the pressure obtained from the direct inversion method for the original case and the case in which a random 5% noise is added to the right hand side respectively. Figure 2.4e shows the exact solution (Eq. 2.15). If no noise is added to the right hand side, the two methods provide a solution that is almost identical to the theory. However, the addition of noise slightly modifies the solution even though is unclear from these plots. To quantify this error,

the relative error in the calculated pressure as well as the relative residual error in solving the system of linear equations is shown in Table 2.3. In this table, the error due noise addition to the right hand side is also consider for 2, 5, 10% noise. The relative residual error is similar for the two methods, being slightly smaller for the lest-squared method. Additionally, the relative residual increases rapidly for small amount of noise, going from about $1e^{-13}$ to $1e^{-4}$, and remain almost constant above 5% noise ($1e^{-4}$). However, the relative error increases linearly with the addition of noise. The error in the least squared method is greater than the error obtained from the direct inversion method. Nevertheless, the relative error does not propagate more than 10% for any noise added within 10% as shown in Table 2.3. Additionally, the least-squared method is faster compared to the direct inversion, since no matrix inversion is needed (especially for large grids). In addition, increasing the number of elements in the grid decreases the relative error. However, the time needed to solve it increases rapidly. Moreover, the direct inversion method is not implementable when having internal boundaries. To further validate the procedure, the author tried different methods to solve for the PPE by using other iterative algorithms such as GMRES or SOR methods, obtaining similar but less accurate results as well as increased time performance. These methods were also tested for the experiments, obtaining the more accurate and fast results by using the least-squared method.

In the results section, pressure fields obtained from the PPE are compared with two other methods. These two methods have been used in the past to calculate pressure fields (and forces) and will be briefly presented here, later discussed and compared to the PPE method. The first method uses the Bernoulli equation to obtain the pressure from the velocity field. For a barotropic, steady, irrotational and inviscid flow, the Bernoulli equation becomes

$$p_{Ber} - p_{ref} = \frac{1}{2}\rho\left(|\vec{u}_{ref}|^2 - |\vec{u}|^2\right) \tag{2.17}$$

where p_{ref} and $\vec{u}_{ref}$ are the reference pressure and velocity at the lower left corner of the control volume, respectively (unless otherwise specified). In the second method, the pressure gradient from the Navier-Stokes equations is spatially integrated to obtain the pressure along the boundaries of the selected control volume within the image domain. Just the pressure at the boundaries of the control volume is needed when calculating forces by this method. To perform the integration, a forward difference scheme is constructed by evaluating the gradients at the mid-points of the grid using linear interpolation of the known gradients from the points before and after. The scheme is given by

$$p_{i+1} = p_i + \Delta q \cdot (\nabla p)_{i+1/2} \tag{2.18}$$

where Δq is the spatial grid resolution along the boundary. The integration proceeds by starting at one of the corners of the control volume.

2.6 Force calculation

To calculate the force per unit length produced by the blade, the integral momentum equation (Eq. 1.5) is applied to the control volume per unit length in Fig. 2.5, where $L = \sum_{i=1...7} L_i$ is the outer contour of an arbitrary volume per unit length S, and $\vec{n}$ is an outward normal vector to these control surfaces. Then, the integral momentum equation is written as

$$\vec{F}_{\text{airfoil}} = -\iint_S \rho \frac{\partial \vec{u}}{\partial t} dS - \int_L \rho \vec{u} \left(\vec{u} \cdot \vec{n}\right) dL + \int_L \left(-p \cdot \vec{n}\right) dL + \int_L 2\mu \bar{\bar{\sigma}} \vec{n} \, dL \tag{2.19}$$

The first integral term contains the local acceleration which is in general neglected for calculating mean forces in quasi-steady flows but for the present work is significant and cannot be ignored. The second integral in Eq. 2.19 is zero along L_4 due to the

non-slip condition and no flow penetration at the airfoil. In addition, the surface force along L_4 is equal in magnitude but opposite to the force produced by the airfoil. Moreover, all the integrals along L_3 and L_5 cancel each other out since they have opposite outward normal, and the values of the variables are the same along the two lines. Thus, the force generated by the airfoil can be written in terms of the integral momentum equation as

$$\vec{F}_{\mathrm{PPE}} = -\iint_S \rho \frac{\partial \vec{u}}{\partial t} dS - \int_{L_1,L_2,L_6,L_7} \rho \vec{u} \left(\vec{u} \cdot \vec{n}\right) dL + \int_{L_1,L_2,L_6,L_7} \left(-p_{\mathrm{PPE}} \vec{n}\right) dL \quad (2.20)$$

It is called F_{PPE} since the pressure term is calculated from the PPE as explained in Section 2.5. The last integral on the right hand side of Eq. 2.19 has been neglected since the viscosity term is about two orders of magnitude smaller than the other terms. A trapezoidal integration is performed for all the line integrals. An extension of the trapezoidal rule for 2D is applied to calculate the surface integral.

The original form of the momentum equation as explained above is also compared to 6 other forms of the same momentum equation. The second and third forms are identical to the original momentum equation (Eq. 2.20), but deriving the pressure term (see Section 2.5) from the spatially integrated pressure

$$\vec{F}_{\mathrm{Intp}} = -\iint_S \rho \frac{\partial \vec{u}}{\partial t} dS - \int_L \rho \vec{u} \left(\vec{u} \cdot \vec{n}\right) dL + \int_L \left(-p_{\mathrm{Intp}} \cdot \vec{n}\right) dL \quad (2.21)$$

and the Bernoulli equation

$$\vec{F}_{\mathrm{Ber}} = -\iint_S \rho \frac{\partial \vec{u}}{\partial t} dS - \int_L \rho \vec{u} \left(\vec{u} \cdot \vec{n}\right) dL + \int_L \left(-p_{\mathrm{Ber}} \cdot \vec{n}\right) dL \quad (2.22)$$

A forth method uses the impulse momentum equation derived by Noca *et al.* (1999) that avoids the use of the pressure term by transforming the momentum equation into the impulse equation (Wu, 1981; Lighthill, 1986) for finite domains. For a 2D

flow, neglecting viscous terms, considering the object moving at constant velocity inside a fixed control volume and non-slip condition at the body surface, the impulse momentum equation becomes

$$\begin{aligned}\vec{F}_{\text{Noca}} =& -\rho\frac{d}{dt}\iint_S \vec{x}\wedge\vec{\omega}dS \\ &+\rho\int_L \vec{n}\cdot\left[\frac{1}{2}|\vec{u}|^2\overline{\overline{I}}-\vec{u}\,\vec{u}-\vec{u}\,(\vec{x}\wedge\vec{\omega}\,)+\vec{\omega}\,(\vec{x}\wedge\vec{u}\,)\right]dL\end{aligned} \tag{2.23}$$

The fifth method was first derived by Noca *et al.* (1999) and then by Wu *et al.* (2005). This equation is just valid if the flow is incompressible, this is, the continuity equation has to be satisfied everywhere. The integrals in this "flux" momentum equation are evaluated at the boundaries of the control volume alone. For an incompressible and inviscid 2D flow in a fixed control volume around a non-accelerating body the "flux" momentum equation becomes

$$\begin{aligned}\vec{F}_{\text{Bound}} =&\rho\int_L \vec{n}\cdot\left[\frac{1}{2}|\vec{u}|^2\overline{\overline{I}}-\vec{u}\vec{u}-\vec{u}\,(\vec{x}\wedge\vec{\omega})+\vec{\omega}\,(\vec{x}\wedge\vec{u})\right]dL \\ &-\rho\int_L \vec{n}\cdot\left[\left(\vec{x}\cdot\frac{\partial\vec{u}}{\partial t}\right)\overline{\overline{I}}-\vec{x}\frac{\partial\vec{u}}{\partial t}+\frac{\partial\vec{u}}{\partial t}\vec{x}\right]dL\end{aligned} \tag{2.24}$$

The sixth and seventh methods are derived in Wu *et al.* (2007) in terms of vorticity diffusion (Eq. 2.25) and advection (Eq. 2.26) terms respectively

$$\vec{F}_{\text{Diff}} = -\mu\iint_S \vec{x}\wedge\nabla^2\vec{\omega}dS + F_L \tag{2.25}$$

$$\vec{F}_{\text{Adv}} = -\rho\iint_S\left(\vec{x}\wedge\frac{\partial\vec{\omega}}{\partial t}+\vec{\omega}\wedge\vec{u}\right)dS-\rho\int_L \vec{x}\wedge[\vec{n}\wedge(\vec{\omega}\wedge\vec{u})]\,dL+F_L \tag{2.26}$$

$$\vec{F}_L = -\mu\left(\int_L[\vec{x}\wedge[\vec{n}\wedge(\nabla\wedge\vec{\omega})]-(\vec{\omega}\wedge\vec{n})]\,dL\right) \tag{2.27}$$

In the force section, the circulation is also calculated and given by

$$\Gamma = -\int_L \vec{u} \cdot d\vec{L} = -\iint_S \omega dS \tag{2.28}$$

where the minus sign is due to the positive clockwise value of the circulation and the positive counterclockwise value of the vorticity by convention in aerodynamics.

In the forces evaluation section (Sec. 6) all the forces calculated by the different methods are compared and discussed. Some of these methods are not suitable for small force coefficients or experimental data, neither consistent with the size of the control volume.

2.7 Error analysis

For all three experimental cases an error analysis of the variables involved in force calculations is performed and summarized in Table 2.4. The three main systematic errors when estimating the velocity field from TR-PIV analysis are due to cross-correlation, peak-locking and spatial-temporal resolution. For a three-point Gaussian peak estimator, the error is less than 0.1 pixels. For *Case 1*, the separation between images is $4ms$, therefore, the estimated error in the velocity is about $0.0015m/s$ or 1.3% of the free stream velocity, being 9.25% and 2.5% for *Case 2* and *Case 3* respectively. The peak-locking error is estimated from the sub-integer velocity histograms and the mean value is about 0.1 pixels, giving a relative error of about 1.3% of the free stream velocity, being 9.25% and 2.5% for *Case 2* and *Case 3* respectively. The uncertainty due to spatial (Eq. 2.29) and temporal (Eq. 2.30) resolution is

estimated from Hart (2000). In the case of a sinusoidal signal, the gain is given by

$$|G_{FFT}|_s = \left|\frac{V_{calc}}{V_{true}}\right| = \left|\frac{\sin\left(\pi\frac{WS}{\lambda_x}\right)}{\pi\frac{WS}{\lambda_x}}\right| = \left|\mathrm{sinc}\left(\frac{WS}{\lambda_x}\right)\right| \tag{2.29}$$

$$|G_{FFT}|_t = \left|\frac{V_{calc}}{V_{true}}\right| = \left|\frac{\sin\left(\pi\frac{f_{shed}}{f_{samp}}\right)}{\pi\frac{f_{shed}}{f_{samp}}}\right| = \left|\mathrm{sinc}\left(\frac{f_{shed}}{f_{samp}}\right)\right| \tag{2.30}$$

where sinc refers to the normalized sinc function. For an interrogation window size (WS) of $1mm$ and a typical mean structure size (λ_x) of $5mm$ in the wake, the gain is about 0.91, in other words, the maximum expected error in the wake is about 9%. For *Case 2*, an interrogation window size of $1.9mm$ and a typical mean structure size of $8mm$ give an expected error of 9%. For *Case 3*, an interrogation window size of $2.3mm$ and a typical mean structure size of $9mm$ give an expected error of 10%. The uncertainty due to temporal resolution in *Case 1* is not calculated since the non-TR method does not resolve time-evolving flow features. For *Case 2*, the sampling frequency of 500 Hz and a typical shedding frequency f_{shed} in the wake of 15 Hz give an error about 0.2%. The shedding frequency in this case is calculated from the average of the shedding frequencies from all instantaneous vorticity fields. The frequency is obtained by calculating the distance between the center of two vortices and the mean traveling velocity of the center of vortex. Since the airfoil is moving through the field of view, the spectral analysis of the velocity signal is not accurate as explained in Section 2.2. For *Case 3*, the sampling frequency of 250 Hz and a typical shedding frequency in the wake of 3.9 Hz give an error about 0.1%. The shedding frequency is calculated from the spectral analysis in the wake as it is shown in Sec. 3.

In addition, the error in truncating the gradients by central differences can be obtained

by the response function (de Kat & van Oudheusden, 2011)

$$T_{CDs} = \mathrm{sinc}\left(\frac{2\mathrm{h}}{\lambda_x}\right) \tag{2.31}$$

$$T_{CDt} = \mathrm{sinc}\left(\frac{2\Delta\mathrm{t}}{t_{shed}}\right) \tag{2.32}$$

where h is the spatial grid resolution and Δt is the temporal step. This results in an uncertainty of 6.4%, 9.0% and 10.4% in the spatial gradients for *Case 1*, *Case 2* and *Case 3* respectively, and 8.2% and 2.6% in the temporal gradients for *Case 2* and *Case 3* respectively. In addition, the response function for the Poisson solver is given by (de Kat & van Oudheusden, 2011)

$$T_{PS} = \frac{1 + \cos\left(\pi\frac{2h}{\lambda_x}\right)}{2\,\mathrm{sinc}\left(\frac{2h}{\lambda_x}\right)} \tag{2.33}$$

This results in an uncertainty of 4.7% for *Case 2* and 6% for *Case 3*.

The random uncertainty of the PIV will be shown in the next sections in terms of the root mean square (RMS) of the velocity, RMS of the acceleration and RMS of the pressure. For instance, the RMS of the axial velocity outside the wake is less than 2% ($u'/U_{ref} < 0.02$) for both *Case 2* and *Case 3*, while the RMS of pressure is up 8% ($(P - P_{ref})'/P_{ref} < 0.08$) for *Case 2* and 10% for *Case 3*. However, to obtain the RMS of the error, the present measurements would need to be compared to an exact numerical solution (such as the study by Charonko *et al.* (2010)) which is not available for the present experiment. Nevertheless, it is possible to use the method by de Kat & van Oudheusden (2011) to estimate the RMS of the pressure from the RMS of the velocity from linear error analysis (Taylor, 1997; Bevington & Robinson,

1969). From this analysis, the error in the derived quantity (pressure) δp is

$$\delta p = \rho\, \delta u \sqrt{\frac{h^2}{2\Delta t^2} + |\nabla u|^2 h^2 + \frac{|u|^2}{2}} \tag{2.34}$$

where δu is the error in velocity and Δt is the temporal step. In a non-dimensional form

$$\frac{\delta p}{p_{ref}} = 2\,\frac{\delta u}{U_{ref}^2} \sqrt{\frac{h^2}{2\Delta t^2} + |\nabla u|^2 h^2 + \frac{|u|^2}{2}} \tag{2.35}$$

where $U_{ref} = \sqrt{U_\infty^2 + (\Omega r_z)^2}$ and $p_{ref} = \frac{1}{2}\rho\left(U_\infty^2 + (\Omega r_z)^2\right)$. For *Case 3*, the rotational speed is zero ($\Omega = 0$). From this analysis, the estimated RMS of the pressure in the wake of the airfoil is 22% and 11% for *Case 2* and *Case 3* respectively, for a 10% RMS in velocity.

Another error can arise from 3D effects. The 3C effects are not evaluated in this work since the system does not allow for 3D or 3C measurements. However, the third component of the velocity is just important close to the tip of the blade where radial velocities up to $0.2U_\infty$ are expected. In addition, as stated by de Kat & van Oudheusden (2011), even for 3D flows, the solution to the 2D Poisson equation requires mostly in-plane measurements.

Measured velocity fields can also be affected due to tunnel blockage. From Barlow *et al.* (1999), a maximum aspect ratio (AR) of 7.5% should be used to neglect errors due to tunnel blockage, where AR is defined as the ratio of rotor to tunnel cross sectional area. For this work, the ratio is 27.7%, which generates a significant wake blockage. As an approximate correction, Barlow *et al.* (1999) suggest $\Delta u/u = AR/4$, which results in a correction factor of 1.07 for the velocity. Additional correction models are developed for global coefficients in water turbines as discussed by Bahaj *et al.* (2007). Even though the blockage affects the results and the accuracy of the

comparison with BEM theory, it should not affect the capabilities of the proposed method to obtain instantaneous pressure and forces in rotors.

Table 2.1: Cord (c) and twist (θ) distribution along the radial direction of the blade

$z(m)$	$c(m)$	$\theta(^\circ)$
0.053	0.057	23.46
0.061	0.056	21.46
0.069	0.054	19.58
0.077	0.053	17.82
0.085	0.051	16.16
0.093	0.049	14.63
0.101	0.048	13.21
0.109	0.046	11.90
0.118	0.044	10.71
0.126	0.043	9.63
0.134	0.041	8.67
0.142	0.039	7.82
0.150	0.038	7.08
0.158	0.036	6.46
0.166	0.035	5.96
0.174	0.033	5.57
0.182	0.031	5.29
0.190	0.030	5.13
0.198	0.028	5.09
0.200	0.028	5.09

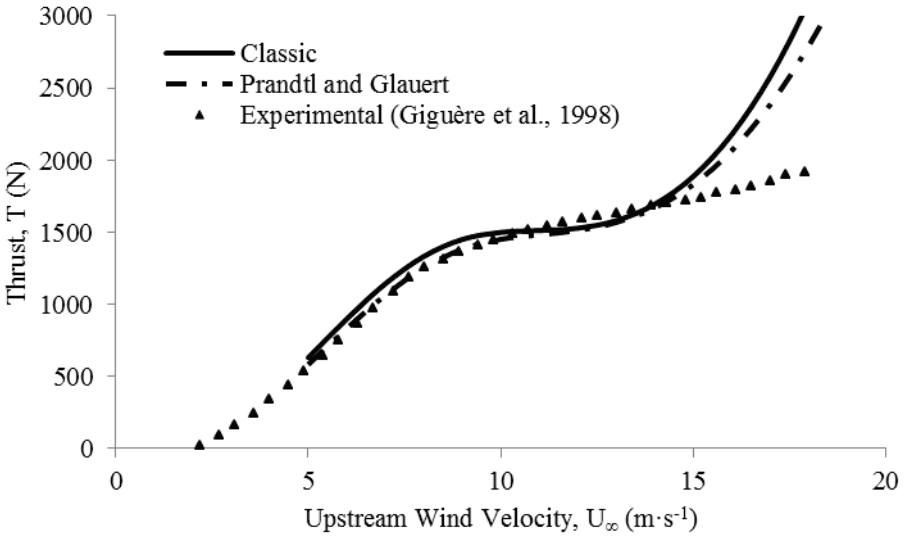

Figure 2.1: Thrust variations with the upstream velocity

Table 2.2: Differences in the experimental setup for the 3 cases of study

Parameter	*Case 1*	*Case 2*	*Case 3*
Device	Water turbine	Water turbine	Fixed wing
$U_\infty\,(m/s)$	0.12	0.10	0.10
$\Omega\,(rpm)$	52	20	-
Re_c	25000	11000	3900
PIV method	2D-PIV	2D-TR-PIV	2D-TR-PIV
Camera resolution (mpx)	2	1	1
Laser power $(mJ/pulse)$	100	10	10
$f_{samp}(Hz)$	14.5	500	250

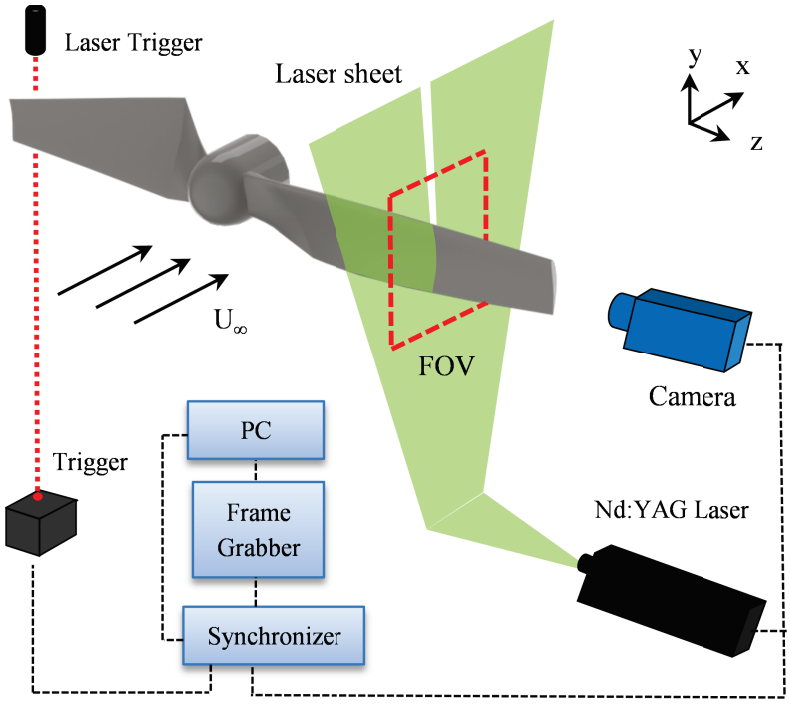

Figure 2.2: Sketch of the PIV setup showing laser/camera system and turbine field of view

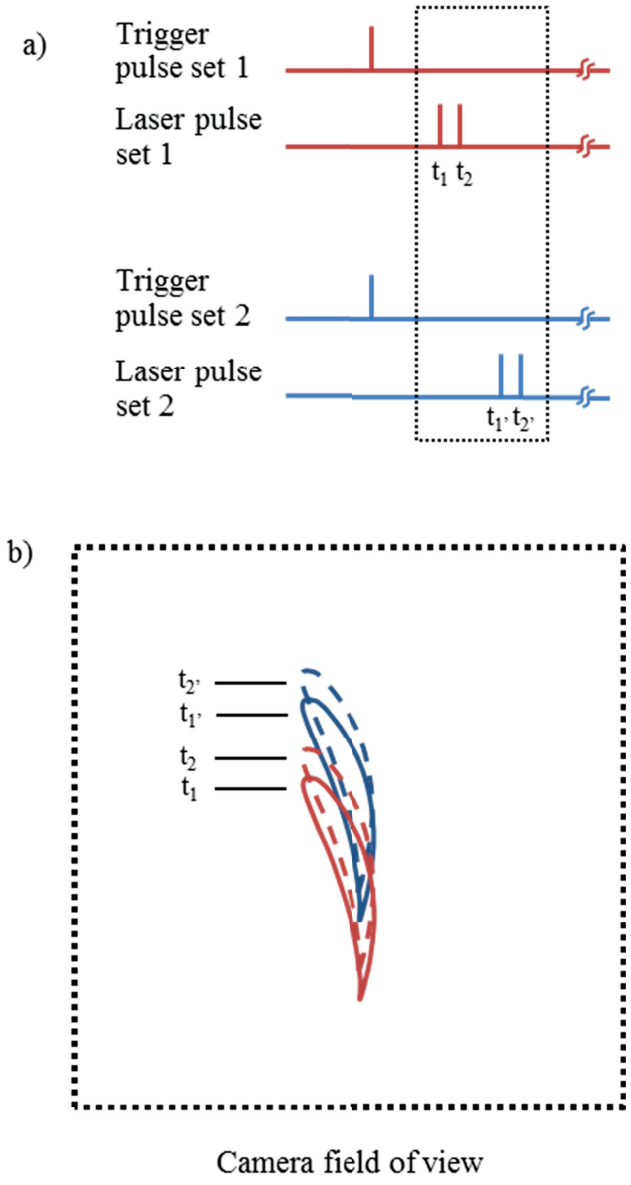

Figure 2.3: a) Timing diagram for the external triggers and laser pulses used for the PIV system and b) sketch of the blade position at the times used to calculate the local acceleration.

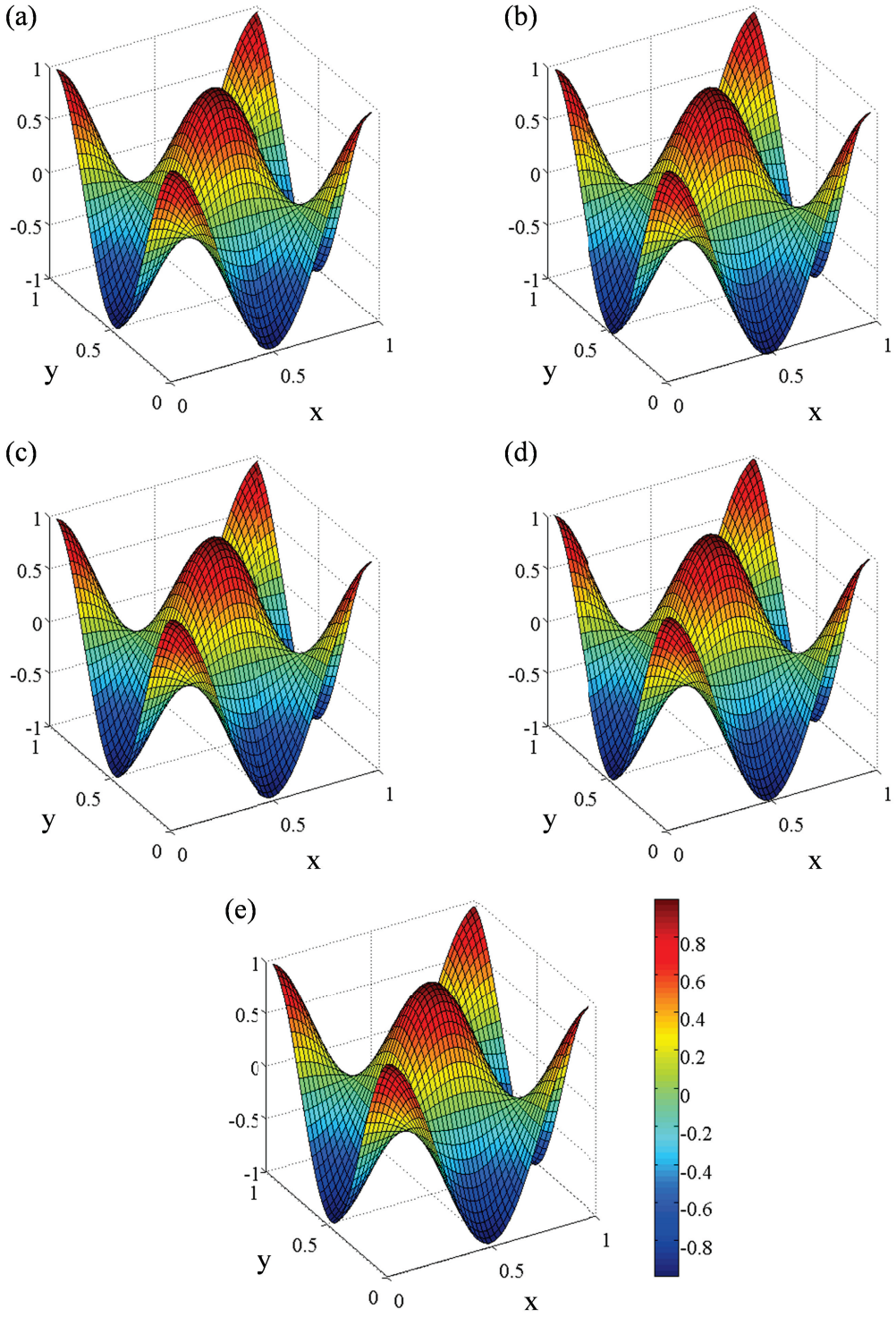

Figure 2.4: Pressure (p) obtained from (a) least-squared method without noise, (b) least-squared method with 5% noise, (c) direct inversion method without noise, (d) direct inversion method with 5% noise and (e) exact solution

Table 2.3: Residual and relative errors in calculating the pressure from the PPE. Solution from the leas-squared and direct inversion methods are compared to the exact known solution

	$\frac{\|A\cdot p-b\|}{\|b\|}$	$\frac{\|p-p_{exact}\|}{\|p_{exact}\|}$
P_{direct}	$8.7e^{-12}$	0.006
$P_{\text{direct}},\ \epsilon = 2\%$	$3.1e^{-4}$	0.019
$P_{\text{direct}},\ \epsilon = 5\%$	$7.6e^{-4}$	0.038
$P_{\text{direct}},\ \epsilon = 10\%$	$1.5e^{-3}$	0.069
P_{lsqr}	$2.1e^{-13}$	0.003
$P_{\text{lsqr}},\ \epsilon = 2\%$	$1.2e^{-4}$	0.023
$P_{\text{lsqr}},\ \epsilon = 5\%$	$3.1e^{-4}$	0.052
$P_{\text{lsqr}},\ \epsilon = 10\%$	$6.1e^{-4}$	0.096

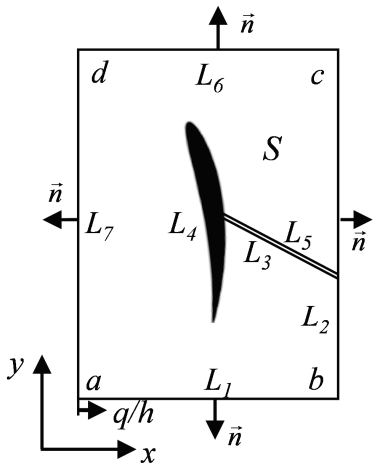

Figure 2.5: Sketch of a control volume per unit length around the NACA8512 used to solve the integral momentum equation. The origin is at a which corresponds to $q/h = 0$

Table 2.4: Error analysis in calculating forces for the three different cases of study. Errors are shown as percentages (%) of the reference values U_{ref} or P_{ref}

Error source	*Case 1*	*Case 2*	*Case 3*
Peak estimator	1.3	9.2	2.5
Peak-locking	1.3	9.2	2.5
Spatial resolution	6.5	9.0	10.4
Temporal resolution	-	0.2	0.1
Spatial gradient truncation	6.5	9.0	10.4
Temporal gradient truncation	-	8.2	2.6
Poisson response	-	4.7	6.0
RMS(u) outside the wake	-	1.8	1.9
RMS(p) outside the wake	-	8.1	9.9
RMS(p) estimated inside the wake	-	21.9	11.3

Chapter 3

Flow features

Before considering instantaneous loads and pressure fields, the time-resolved flow features around the blade will be explained first since these will have a large impact on the loads and pressure fluctuations. All results are presented in a stationary reference frame (unless otherwise specified) in which the blade moves vertically up through the field of view for *Cases 1* and *2*. In such an inertial frame, the results can be evaluated directly from the PIV measurements without the need to subtract the rotation velocity or include the extra inertial terms in the Navier-Stokes and integral momentum equations.

3.1 *Case 1*: High-rpm water turbine

A typical instantaneous and mean velocity fields measured around the blade is shown in Fig. 3.1. Measurements are taken at the radial distance $r_z = 0.85R$ (85% of the rotor radius). Results in Fig. 3.1 correspond to contour plots of the axial (U) and tangential (V) velocity field components for instantaneous and ensemble averaged measurements. The axial velocities in Fig. 3.1a and 3.1b show the velocity increasing in the concave part of the airfoil close to the leading edge and the velocity decreasing close to the trailing edge. The tangential velocities in Fig. 3.1c and 3.1d show the highest value at the leading edge and the velocity increasing along the concave part in the negative direction of the y-direction. Larger differences between instantaneous

and mean values are shown in the wake, since a small vortex shedding street is formed. This variations causes fluctuation in the calculated forces as shown in Sec. 6 by analyzing the contribution of each term to the total force.

For this case of study, the moving frame of reference was also tested. As shown in Appendix A, the two frames of reference led to a very similar solution of the pressure field. In addition, the mean forces calculated by the two methods agree within 15% and always within one standard deviation.

3.2 *Case 2*: Low-rpm water turbine

3.2.1 Raw data

The time-resolved instantaneous flow field characteristics around the blade are shown in figure 3.2. In this case, the vortex shedding street shows flow structures about double the size of the ones found in *Case 1*. Results are non-dimensionalized using a characteristic time, velocity, and length for a more general comparison. Since the vortex shedding is the main feature observed in force fluctuations, the characteristic time is given by the inverse of the vortex shedding frequency ($t_{ref} = 1/f_{shed}$). The characteristic velocity is given by the total free stream relative velocity as

$$U_{ref} = \sqrt{U_{\infty}^2 + (\Omega r_z)^2} \tag{3.1}$$

The position in the x- and y-axis is non-dimensionalized by

$$h = U_{ref} t_{ref} \tag{3.2}$$

Results are shown for six time steps where time has been non-dimensionalized ($t^* = t/t_{ref}$) by the time between the average shedding of two vortices with the same circulation direction (t_{ref}). For a given time, each row in figure 3.2 contains the instantaneous axial (x-direction) and tangential (y-direction) velocity, the velocity magnitude and the vorticity. The time evolution of the flow features around the blade shows that these remain constant with time except in the wake where vortex shedding occurs and in the upper side of the blade (extrados) where a recirculating region is formed. For instance, the contour plots of the axial velocity field show regions in the wake of high velocities in the positive (red) and negative (blue) directions that are being convected with time. Similarly, the contour plots of the vorticity field show regions in the wake of positive (red) and negative (blue) circulation being shed from the trailing edge and from the end of the upper part of the blade respectively. The location of the separation of the shear layer that causes the vortex shedding in the airfoil upper region can be elucidated from the tangential velocity field where there is region of positive velocity (red) that detaches from the trailing edge. The time series shows nearly a full cycle of the vortex shedding where two vortices of opposite circulation are being shed.

Also of interest is the recirculating region in the upper side of the blade. For instance, the contour plot of the tangential velocity field shows a region in the upper side of the airfoil where the velocity changes from a negative to a positive direction indicating the beginning of the recirculating region. That region ends near the trailing edge where the vortex shedding occurs. This region can also be extracted from vorticity contour plots where a large clock-wise circulation (blue) is present. The time series shows how this circulation area slightly grows and decreases in size. This is the result of the evolution of the combine recirculation region and a vortex shedding region.

The time evolution of flow features in the airfoil's wake indicates that the quasi-steady

flow approximation cannot be used when calculating instantaneous forces. This can be observed by the differences between the instantaneous measurements and ensemble averages. For instance, figure 3.3a shows contour plots of the ensemble average axial and tangential velocity, velocity magnitude and vorticity fields around the blade. For conciseness ensemble averages are only shown for one of the five blade locations from figure 3.2 since they are all nearly identical. As expected, the differences between the mean and the instantaneous fields are mainly in the wake. This is also shown by the contour plots of the standard deviation in figure 3.3b with the major fluctuations occurring in the wake due to vortex shedding and inside the recirculation bubble. Figure 3.3a shows that the detail information about the vortex shedding is lost in the ensemble averages. For instance, the axial velocity shows a region of low velocity and a region of high velocity where the vortex detaches from the upper part of the blade and from the trailing edge of the blade respectively. But the details about alternating high and low velocity regions observed in the instantaneous measurements downstream in the wake are not visible. Similarly, the normal velocity does not present the type of flow variations present in the wake in the instantaneous plots, rather it shows a continuous region of high velocity (shown in red) indicating general flow retardation. Perhaps, the only places where one can observe some details about the vortex shedding is in the vorticy field region where the vortices of opposite circulation separate from the airfoil. This is expected after evaluating in the instantaneous plots that the vortex detachment from the airfoil takes a large part of the full shedding cycle.

A more quantitative description of the flow can be obtained by evaluating the instantaneous flow velocity components around the external boundary as shown in figure 3.4. The external boundary is given by the labeled a-b-c-d red box in figure 3.4. This is represented in the x-axis in figure 2.5 by the normalized line path q/h where the boundary lines corresponding to a-b, b-c, c-d and d-a are $0 < q/h < 1.5$, $1.5 < q/h < 4.2$, $4.2 < q/h < 5.7$, and $5.7 < q/h < 8.4$ respectively. Three main

regions are identified along the external boundary which are labeled as wake, low pressure and high pressure. The wake region covers the vortex shedding and expands the a-b and part of the b-c boundary. The low pressure region covers the upper part of the blade and expands part of the b-c and c-d boundaries. The high pressure region covers the lower part of the blade and expands parts of the c-d and d-a boundaries. Results are shown in figure 3.4 for three consecutive instantaneous velocities ($t^* = 0.61, 0.67, 0.73$). It shows that time variations are centered in the wake area ($0 < q/h < 1.5$). When comparing instantaneous and ensemble averages in figure 3.4, the differences are again observed in the wake region. The ensemble average shows that the high and low peaks observed in the instantaneous measurements due to vortex shedding in the wake are filtered as the result of averaging the variations of 100 instantaneous sets. No noticeable variations are observed in the low and high pressure regions marked in figure 3.4 as shown by the near 0 standard deviation in the region of $1.5 < q/h < 8.4$ while there is up to $\sim 35\%$ standard deviation in the wake region.

3.2.2 POD analysis

Since the temporal information is limited in this case, the POD phase-averaged technique is applied to the raw data as explained in Sec. 2.4. In this formulation of the problem, a rotating frame of reference is selected so the airfoil remains stationary in the field of view. A comparison between the original raw data and the reconstructed data from the first 2 most energetic modes is shown in Fig. 3.5. The velocity fields (Figs. 3.5a and 3.5b) from POD are filtered; however, it preserves the main flow features even at the wake of the airfoil. The vorticity field shows a good agreement between raw and reconstructed data around the airfoil (including the recirculating area), with higher differences revealed in the the wake, where more irregular vortex

shapes are found. This is probably due to filtering secondary frequencies that may be presented during the shedding process.

A reconstruction of one whole shedding cycle of the phase-averaged vorticity field (Fig. 3.6) show the alternating pattern of the vortices in the wake. Moreover, the vortices appear to decrease in intensity once they are convected downstream compared to the raw case and more odd shapes are found. This may be due to the frequency filtering. For this reason, the wake edge of the control volume should not be far from the trailing edge of the airfoil when calculating instantaneous forces for this case.

3.3 *Case 3*: Stationary airfoil

3.3.1 Raw data

Time-resolved instantaneous flow field characteristics around the stationary airfoil are shown in figure 3.7. These results are non-dimensionalized using a characteristic time, velocity, and length as described in Sec. 3.2.1.

Results are shown for three time steps where time has been non-dimensionalized by the shedding time. For a given time, each row in figure 3.7 contains the instantaneous axial (x-direction) and tangential (y-direction) velocity and the vorticity respectively. The time evolution of the flow features around the airfoil again shows that these remain constant with time except in the wake where the vortex shedding occurs and in the upper side of the airfoil where the recirculating bubble is formed. In addition, from the axial velocity, the transitional zone where the recirculating flow occurs can be elucidated. Up to $\sim 26\%$ standard deviation in velocity is calculated in the wake region (smaller than *Case 2*).

3.3.2 POD analysis

For this case, flow features are evaluated from the raw velocity fields as well as the POD reconstructed velocity fields. In this case a full POD analysis is performed with a total of $N = 1000$ snapshots taken. The reconstruction of the velocity field is obtained by using the first 2, 4 and 10 most energetic modes ($M = 2, 4, 10$). Fig. 3.8a and 3.8b show the relative energy, $\lambda_n / \sum_{n=1}^{N} \lambda_n$, of each mode and the cumulative energy, $\sum_{n=1}^{N=M} \lambda_n / \sum_{n=1}^{N} \lambda_n$, respectively. Figure 3.8a shows that the first 2 modes are dominant. Just the first 2 modes contribute more than 83% of the total energy content as shown in Fig. 3.8b. The addition of modes 3 and 4 raises that value to about the 90% of the total energy. By including the next 6 modes, the total energy content raises to 93%, which satisfies the restrictions stated by Holmes *et al.* (1998) about the number of modes to be included ($> 90\%$ of the total energy). In addition, the energy content was independent of the number N of instantaneous fluctuating velocity fields used for the POD analysis for $N > 100$, in agreement with Oudheusden *et al.* (2005), ensuring that the data is large enough to provide statistical convergence. The evolution of the first 2 POD coefficients is shown in Fig. 3.8c as well as their power spectral density (Fig. 3.8e and 3.8f). For a stationary random signal, the autocorrelation function of the signal $F(t)$ (Eq. 3.3) and its PSD (Eq. 3.4) are a Fourier transform pair (Pope, 2000)

$$X(\tau) = \langle F(t)F(t+\tau) \rangle \tag{3.3}$$

$$PSD(\omega) = \int_{-\infty}^{\infty} X(\tau) e^{-i\omega\tau} d\tau \tag{3.4}$$

Both modes show the same dominant frequency with a phase difference of $\pi/2$. These two modes are associated with the vortex shedding in the wake since the dominant

frequency is the shedding frequency and, hence, high periodic changes in the flow features are expected within one complete shedding cycle. In addition, the evolution of the POD coefficients of modes 3 and 4 are shown in Fig. 3.8d as well as their power spectral density (Fig 3.8g and 3.8h). Both modes have the same dominant frequency and a phase difference of $\pi/2$. The dominant frequency for modes 3 and 4 is double the shedding frequency; hence, small periodic changes are expected within half shedding cycle. Although not shown for brevity, modes 5, 6 and 8 show the higher peak in their PSD at very low frequency. However, the peaks are not entirely captured since the time series are short due to hardware limitations. In addition, small high frequency peaks ($15f_{shed}$ and $19\mathrm{f_{shed}}$) are found in modes 5, 7 and 8. These modes can be associated to the Kelvin-Helmholtz instability in the separated shear layer (Yarusevych *et al.*, 2006); however, the separated shear layer in the upper side of the airfoil is not fully resolved in this experiment to capture effectively the instability. The remaining POD coefficients are much smaller in energy content and no dominant frequencies were clearly identified except for the shedding frequency. Those modes are said to be turbulent modes and noisy modes. Since the flow is mostly laminar, these low energy modes can be due to small perturbances in the flow and errors in the measurement method and can drain some energy at specific times.

The reconstruction of the velocity field from the most energetic modes (as explained in Section 2.4) results in a cleaner representation of what is important in terms of kinetic energy fluctuations. By removing high frequency noise and other less energetic modes, errors that may propagate through the calculations are reduced. Figure 3.9 compares the original and reconstructed vorticity fields from the first 2, 4 and 10 most energetic modes. The original field (Fig. 3.9a) shows the vortex shedding pattern in the wake as well as the recirculating bubble in the suction side of the airfoil. The POD vorticity fields (Fig. 3.9b, 3.9c and 3.9d) seem filtered from the calculations, keeping the same flow features that the original flow field. Once the velocity fields

are reconstructed, the force calculation analysis follows the same process showed in Secs. 2.5 and 2.6. The next section shows the spectral analysis of the velocity signals to identify main frequencies and structures in the wake of the airfoil, associated to those observed in the most energetic modes.

3.3.3 Coherence structures

For the experimental conditions stated in Sec. 2.2, the wake of the airfoil reveals alternating vortex patterns with opposite circulation at a shedding frequency of $f_{shed} = 3.9$ Hz. The shedding frequency is obtained from the power spectral density analysis of the velocity signal and by fitting the peak using a 3-point Gaussian peak estimator.

The spectral analysis is performed at different x/h and y/h locations as shown in Fig. 3.10a and Table 3.10b. Probes 1 and 2 are situated close to the leading edge in the upper and lower side of the airfoil. Probe 3 is located at the mid-span on the lower side of the airfoil. Probe 4 is located within the recirculating area in the upper side of the airfoil. Probes 6, 7 and 8 are located at the wake of the airfoil. The PSD of the axial velocity u (Fig. 3.11a) and vertical velocity v (Fig. 3.11b) disclose the main shedding frequency as well as a secondary less dominant frequency which is double the shedding frequency at the wake locations. This is in agreement with the dominant frequencies observed in the POD coefficients from the first 4 modes. The secondary frequency seems to have a larger peak in the axial direction (u-direction), which means greater changes every half shedding cycle are expected in the axial direction compared to the vertical direction. In the wake of the airfoil, a lower frequency is also identified which does not show a clear peak (limited by the number of images the camera can store), in agreement with the frequencies found in modes 5, 6 and 8. In addition, Fig. 3.11a and 3.11b reveals that important changes are only occurring in the wake of the airfoil and inside the recirculating bubble, since the peaks of the

PSD in those locations is much greater ($\sim$ 3 order of magnitudes) than the PSD calculated at the other locations. Therefore, fluctuations in derived quantities such as forces are expected to fluctuate almost exclusively due to changes in the wake of the airfoil. Another way of showing that fluctuations just happen on the wake is by showing the RMS of the velocity as in Fig. 3.12a and 3.12b. The higher RMS of the velocity happens in the wake and the beginning of the recirculating area ($\sim$ 26%). However, they do not provide any information about dominant frequencies. A study of how the vortex shedding is affecting the force fluctuation is analyzed in detail in the Section 6.3.

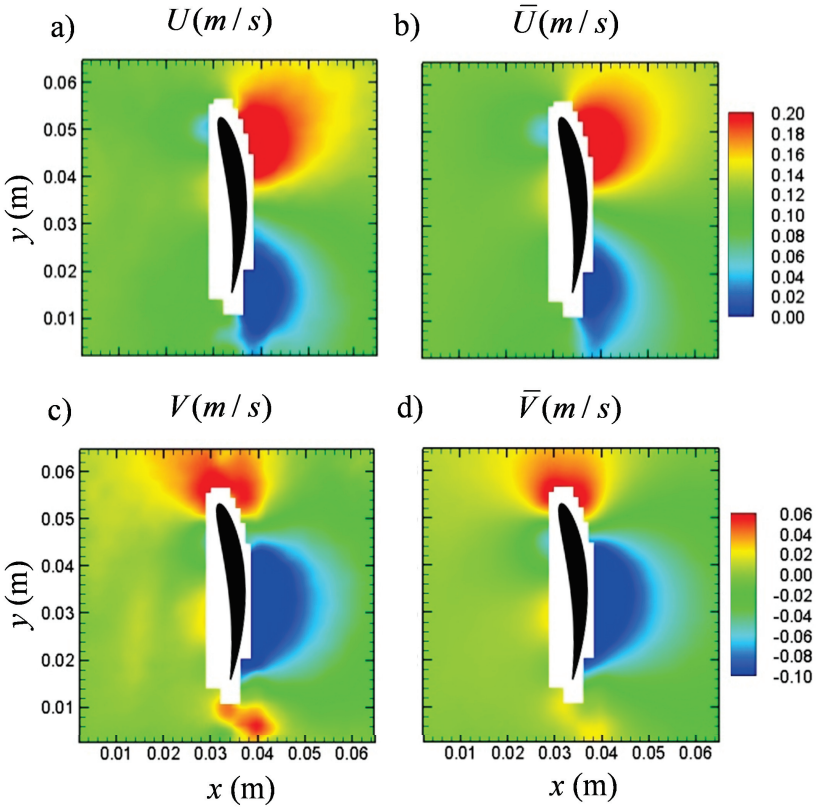

Figure 3.1: Velocity field around the rotating airfoil for *Case 1* at the 85 % of the radius of the rotor for a) the instantaneous axial velocity, b) the ensemble averaged axial velocity, c) the instantaneous tangential velocity and d) ensemble averaged tangential velocity

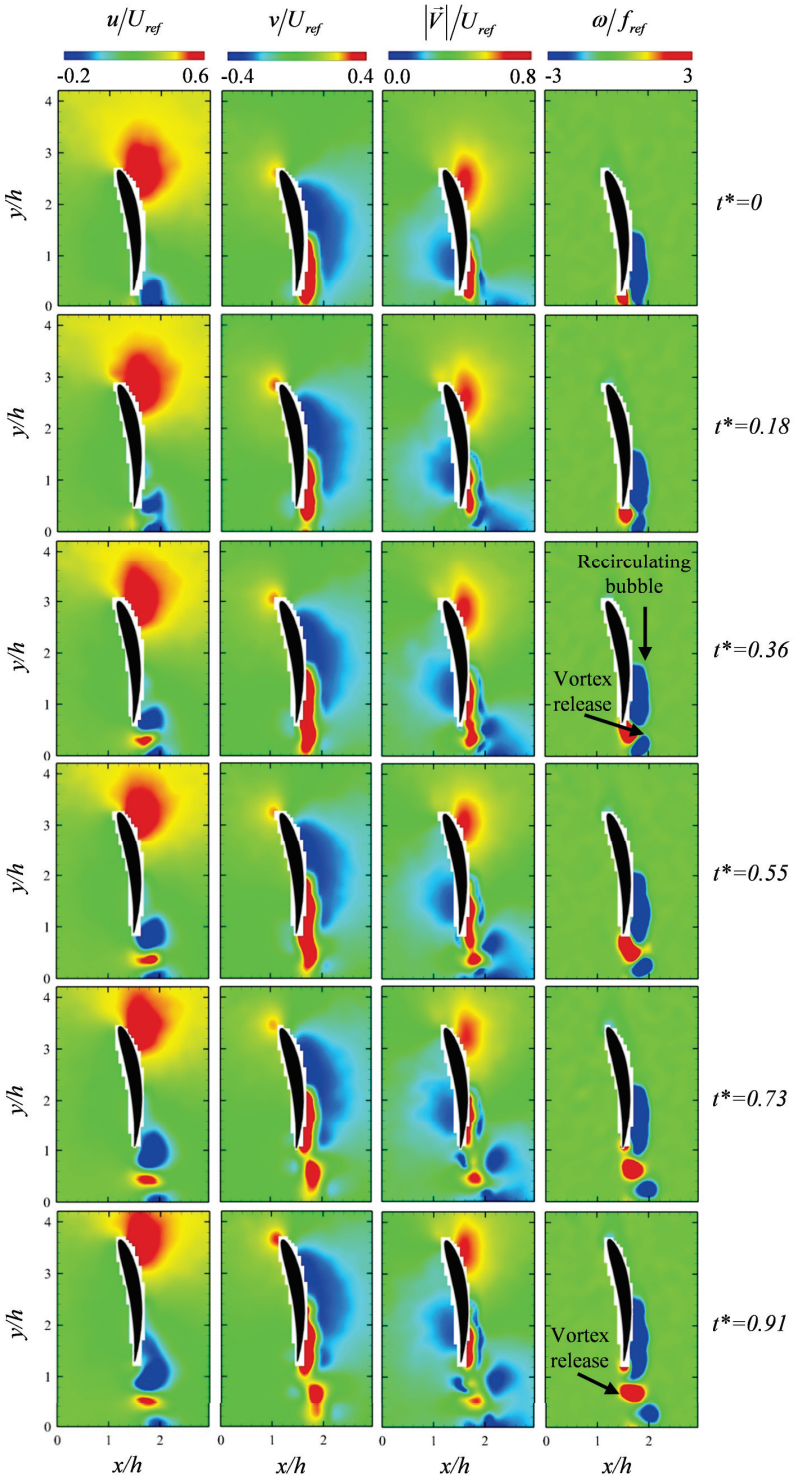

Figure 3.2: Contour plots of six instantaneous time-resolved axial, tangential and total velocity fields and vorticity field at the 75 % radius location of the rotating airfoil for *Case 2*. The x and y-directions are referred throughout as the axial and tangential direction respectively

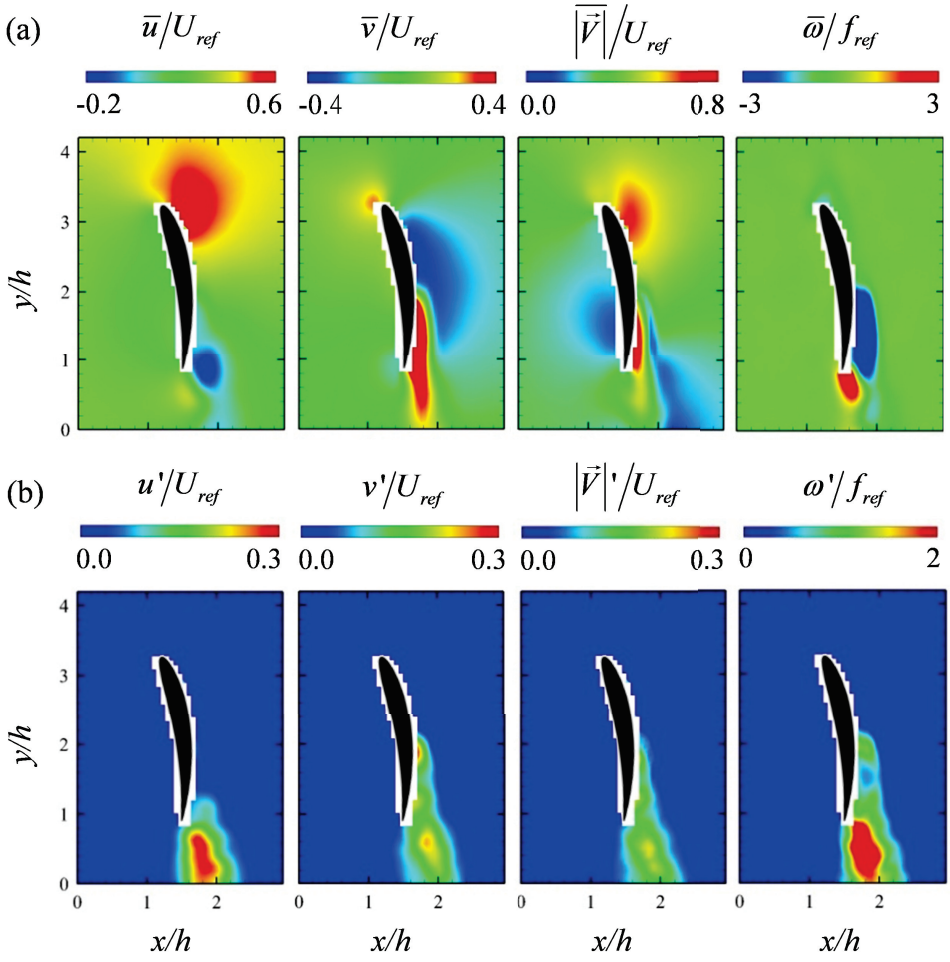

Figure 3.3: (a) Ensemble average and (b) standard deviation contour plots of the axial, tangential and total velocity fields and vorticity fields for *Case 2*

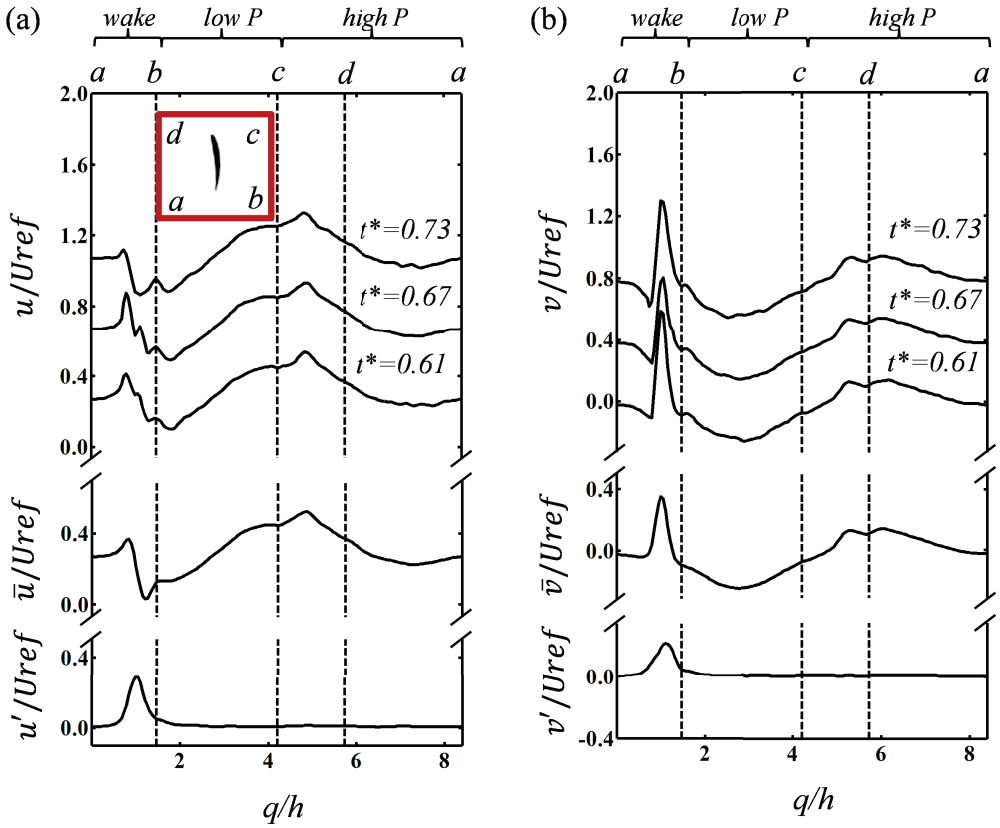

Figure 3.4: (a) Axial and (b) tangential velocity along the boundary of the control volume for *Case 2*. Each plot includes the results for three consecutive instantaneous measurements, the ensemble average and the standard deviation. A 0.4 offset of is used to separate the three instantaneous cases

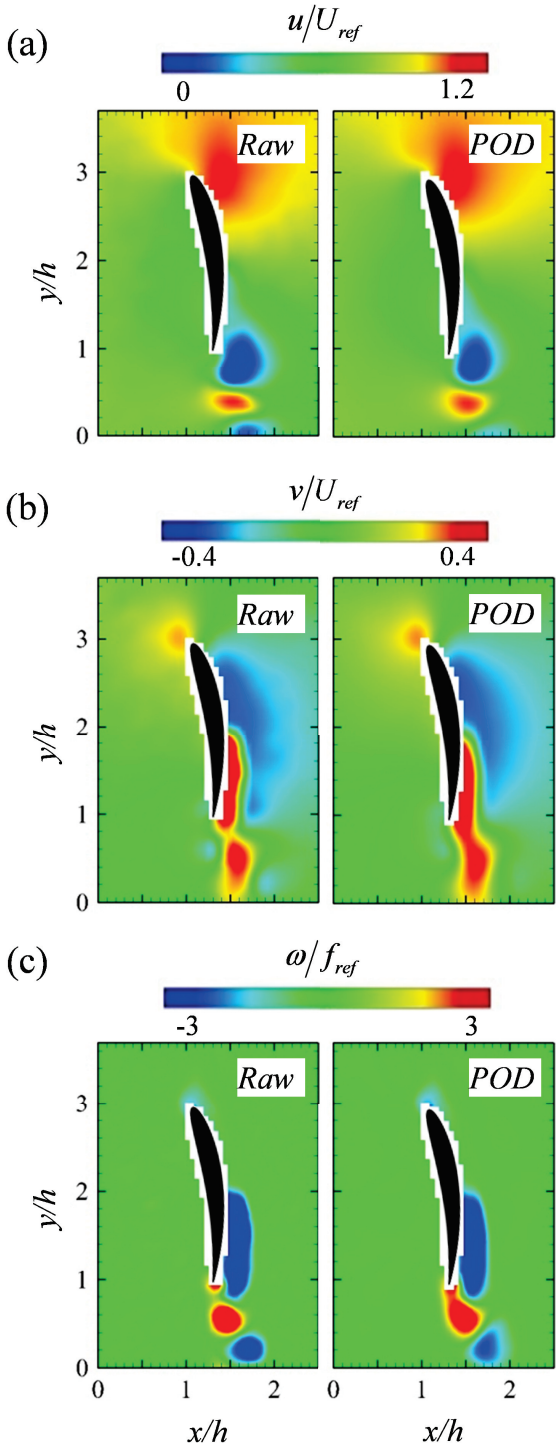

Figure 3.5: Comparison between raw data and phase-averaged POD data for *Case 2*. (a) Axial velocity field, (b) tangential velocity field and (c) vorticity field

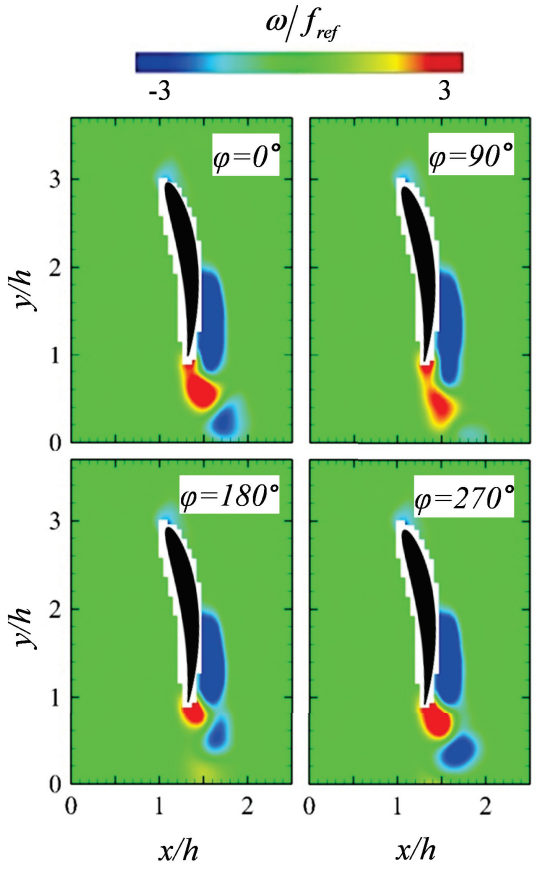

Figure 3.6: Reconstruction of the vorticity field from POD at 4 different phase angles (φ) for *Case 2*

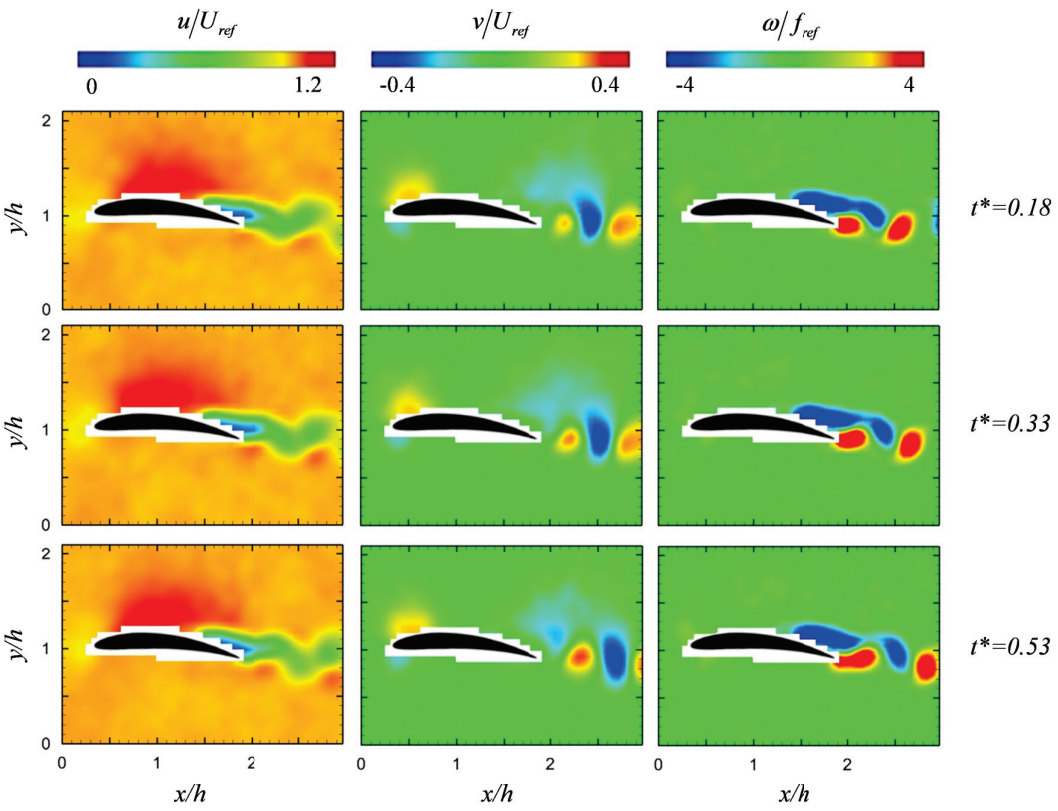

Figure 3.7: Contour plot of three instantaneous time-resolved axial and tangential velocity fields and vorticity field for *Case 3*

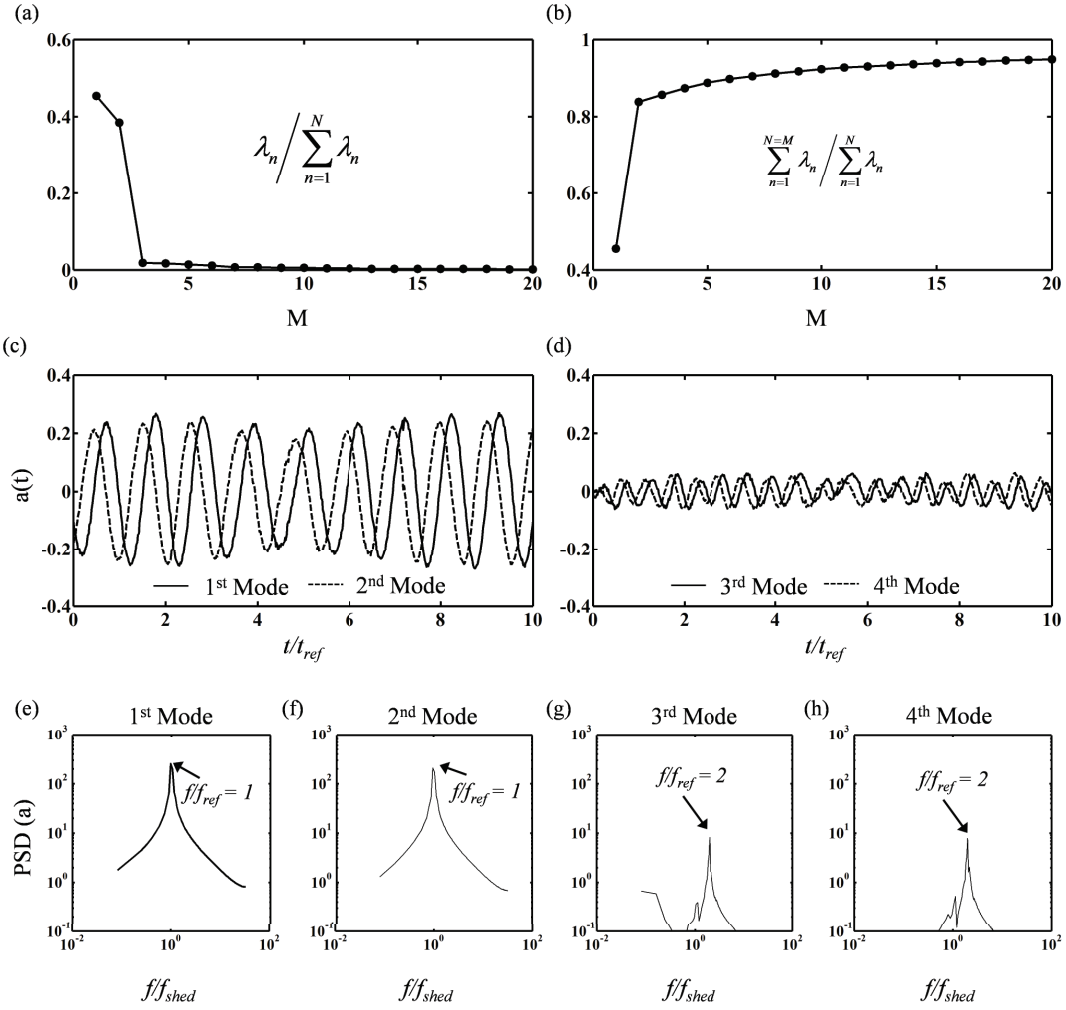

Figure 3.8: POD analysis of the flow for *Case 3*. (a) Relative energy, (b) cumulative energy, (c) time evolution of the first and second most energetic modes, (d) time evolution of the third and fourth most energetic modes, (e) PSD of the 1^{st} mode, (f) PSD of the 2^{nd} mode, (g) PSD of the 3^{rd} mode and (h) PSD of the 4^{th} mode

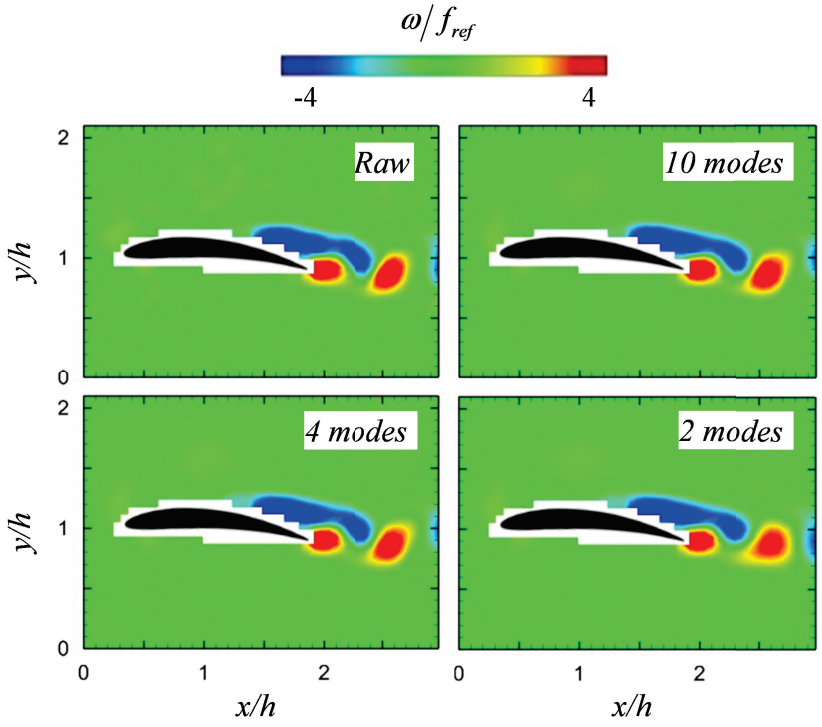

Figure 3.9: Instantaneous vorticity fields of the original field (raw data) and the reconstructed field from POD by taking the first 10 modes, 4 modes and 2 modes containing the highest relative energy for *Case 3*

(a)

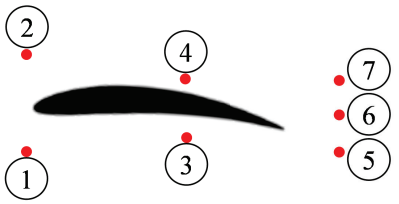

(b)

Location	*x/h*	*y/h*
1	0.31	0.68
2	0.31	1.42
3	1.36	0.74
4	1.36	1.24
5	2.47	0.68
6	2.47	0.93
7	2.47	1.17

Figure 3.10: (a) Probe locations around the airfoil where the PSD analysis is done for *Case 3*. (b) Table showing the probe x/h and y/h locations

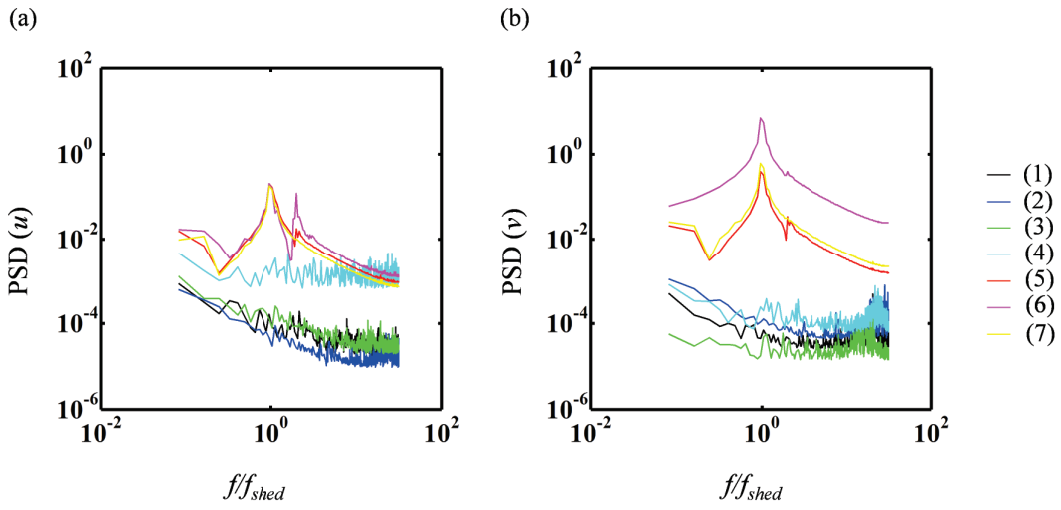

Figure 3.11: Power spectral density of (a) axial velocity, u, and (b) vertical velocity, v, at different probe locations (see Fig. 3.10) for *Case 3*

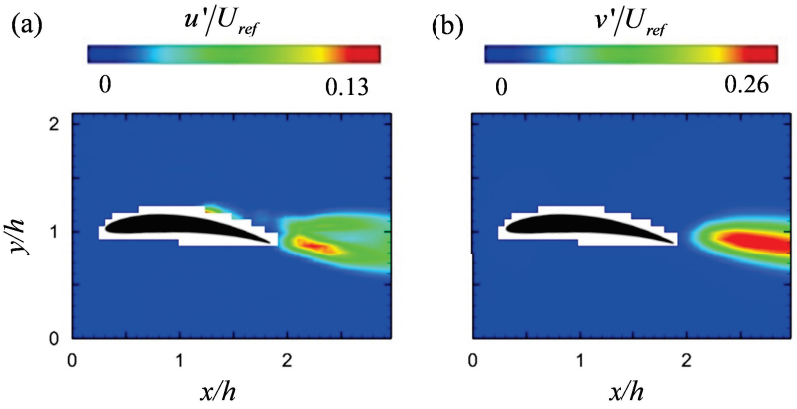

Figure 3.12: Root mean square of the (a) axial and (b) vertical velocity for *Case 3*

Chapter 4

Local and convective accelerations

To solve for the pressure gradient from the Navier-Stokes equations, the local acceleration, convective acceleration and viscous term are needed. They can be calculated from spatial and temporal finite differences of the TR-PIV velocity data. The pressure gradient is then used to solve for the pressure. In addition, the acceleration term is needed when calculating forces since it has an important contribution to the total force fluctuation.

4.1 *Case 1*: High-rpm water turbine

The contribution of each term to the pressure gradient can be evaluated by using the temporal and spatial gradients of the computed velocity fields. For instance, Fig. 4.1 shows contour plots with the x-component contribution from each term. In a stationary reference frame the dominant terms are the local acceleration and the convective acceleration. On the order hand, the diffusive term is about two orders of magnitude smaller and it can be neglected. This is expected since the average Re_c based on the cord of the airfoil is about 25000. By applying the methodology described in Sec 2.3 the local acceleration can be obtained from two non-consecutive velocity fields. However, since regular 2D-PIV is used, the local acceleration at the wake is not properly resolved. The quasi-instantaneous values (as explained in Section 2.3) will serve as a reference where the flow is steady (outside the wake) and only the

mean values and standard deviations are discussed.

4.2 *Case 2*: Low-rpm water turbine

4.2.1 Raw data

Both instantaneous local and convective terms for the x- and y-momentum equations are shown in Fig. 4.2, with the accelerations non-dimensionalized by $a_{ref} = U_{ref}/t_{ref}$. For conciseness the viscous term is not shown as its magnitude is nearly two orders of magnitude smaller than the others and can be considered negligible. This is expected since the average Re_c based on the cord of the blade is ~ 11000.

A direct comparison of all the momentum equation terms in Fig. 4.2 show that their range of magnitudes are comparable and therefore none of them should be neglected. Traditionally, the unsteady term has been neglected for wind turbines with quasi-steady flows (Ragni *et al.*, 2011) through the choice of a rotating reference frame. When a fixed frame is used, the unsteady term cannot be neglected even in regions with quasi-steady flow such as the blade leading edge where strong acceleration and decelerations are observed. There is also a strong deceleration (shown in blue in Fig. 4.2) in the axial-direction in the upper side of the blade from the recirculation zone where high speed fluid is entrained and slowed down. Similarly, there is also acceleration in the tangential-direction near the wall as the recirculating zone moves fluid upstream along the upper side of the blade (shown in red in Fig. 4.2). However, the largest unsteady acceleration magnitudes are observed in the wake due to vortex shedding. But to date, this contribution has been neglected in wind turbines.

The effect of the convective acceleration term is important in regions where there are spatial velocity gradients along the streamline. This includes the leading edge and wake as shown in Fig. 4.2 with the largest magnitudes observed in the wake and the

recirculation area. This is the result of vortices of opposite circulation being shed that generate large velocity changes and accelerations. This is shown in the contour plots of the instantaneous local and convective acceleration field by the alternating patterns of positive (red) and negative (blue) value regions in the wake. These patterns are convected in time which is consistent with that of the shedding.

The time evolution of flow structures in the wake indicates that the quasi-steady flow approximation cannot be used for force and pressure calculations even for rotating frames of reference. This is further observed when comparing the instantaneous measurements to ensemble averages. For instance, Fig. 4.3a shows contour plots of the ensemble average local and convective acceleration field in the x- and y-momentum equations. As expected, the only differences between the mean and the instantaneous fields are in the wake shedding region. This is also shown by the contour plots of the standard deviation in Fig. 4.3b with the major fluctuations occurring in the wake due to vortex shedding and inside the recirculation bubble. Similar to the discussion in reference to Fig. 3.2 and 3.3, the shedding details are partially lost in the ensemble averages. For instance, the mean axial acceleration field shows a region of acceleration but details about the alternating acceleration and deceleration previously observed have been filtered during the averaging. In addition, the vortex detachment from the blade takes a large part of the full shedding cycle. Thus, the mean local and convective acceleration fields show a strong acceleration and deceleration, respectively, attached to the trailing edge.

Further evidence of the time dependence of the flow in the wake can be obtained by evaluating the instantaneous local acceleration around the external boundary as shown in Fig. 4.4. The external boundary is given by the labeled a-b-c-d red box in Fig. 4.4. This is represented in the x-axis in Fig. 2.5 by the normalized line path q/h where the lines corresponding to a-b, b-c, c-d and d-a are $0 < q/h < 1.5$,

$1.5 < q/h < 4.21.5 < q/h < 4.2$, $4.2 < q/h < 5.7$, and $5.7 < q/h < 8.4$ respectively. The three instantaneous local acceleration results in Fig. 4.4 ($t^* = 0.61, 0.67, 0.73$) show that the time variations are centered in the wake area ($0 < q/h < 1.5$) where the large acceleration peak (q/h $\sim$ 1) fluctuates. When comparing instantaneous and ensemble averages values, the differences are again observed around the acceleration peak in the wake. The ensemble average shows a lower acceleration peak than the instantaneous ones as the result of averaging the variations of 100 instantaneous sets. No noticeable variations are observed outside this region of $0 < q/h < 1.5$ as shown by the near 0 standard deviation in the region of $1.5 < q/h < 8.4$ while there is up to $\sim 50\%$ standard deviation in the wake. Thus, these results show that a quasi-steady flow approximation would not be appropriate in the wake region due to the vortices crossing the labeled *a*-*b* line which results in acceleration peak fluctuations.

4.2.2 POD analysis

Local and convective accelerations are also shown for the POD case (Fig. 4.5). A direct comparison to the raw data is not suitable since both methods use two different frames of reference. The local acceleration remains almost zero everywhere around the airfoil (including the recirculating area), except for the wake. Alternating patterns of accelerating fluid are observed in the wake of the airfoil, again consistent with the vortex shedding. In addition, the axial acceleration seems to be more intense than the tangential acceleration. This is maybe due to the lost of information in filtering secondary frequencies, since the tangential acceleration should contain small changes every half shedding cycle as explained in Sec. 3.3 for the case of the fixed airfoil. Convective accelerations are about the same order of magnitude as local accelerations and present similar patterns at the shedding frequency. However, they show some non-zero constant features around the airfoil as shown in Fig. 4.5. Nevertheless, the

higher convective accelerations happen in the wake.

4.3 *Case 3*: Stationary airfoil

4.3.1 Raw data

For the case of the stationary airfoil, the local acceleration shows similar trends as the ones obtained for the phase-averaged POD accelerations in *Case 2* (Sec. 4.2.2) as shown in Fig. 4.6. Almost zero local acceleration values are found around the airfoil (including the recirculating area), except in the wake of the airfoil for both axial and vertical local accelerations. The accelerated flow features observed in the wake are consistent with that of the vortex shedding. An analysis of how the local acceleration term affect the calculated forces is done in Ch. 6.

4.3.2 POD analysis

A comparison between the axial and tangential local accelerations from raw and 4-modes POD data is shown in Fig. 4.7. Both accelerations seems to be slightly filtered from the POD analysis, preserving the same features observed in the raw case.

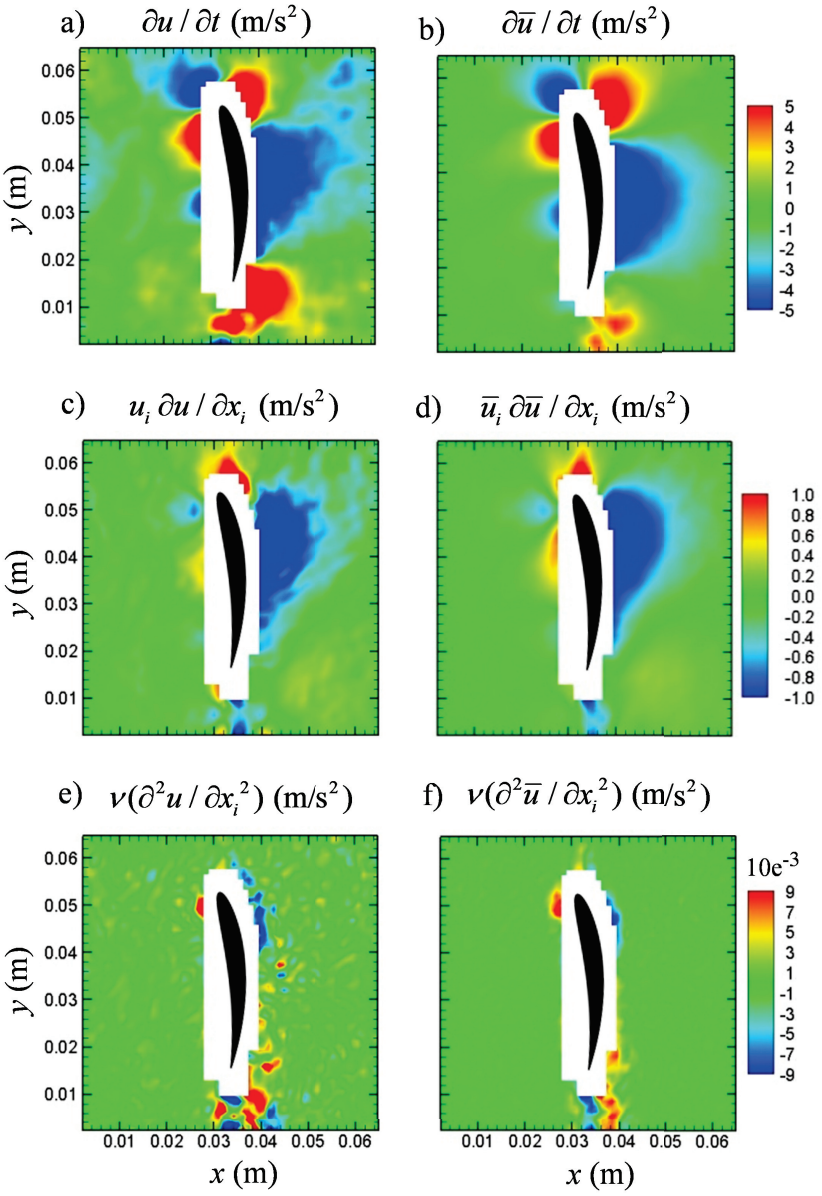

Figure 4.1: Contour plots of the different terms used in the pressure gradient calculation for *Case 1* including a) instantaneous and b) mean local acceleration, c) instantaneous and d) mean convective acceleration and e) instantaneous and f) mean viscous diffusion

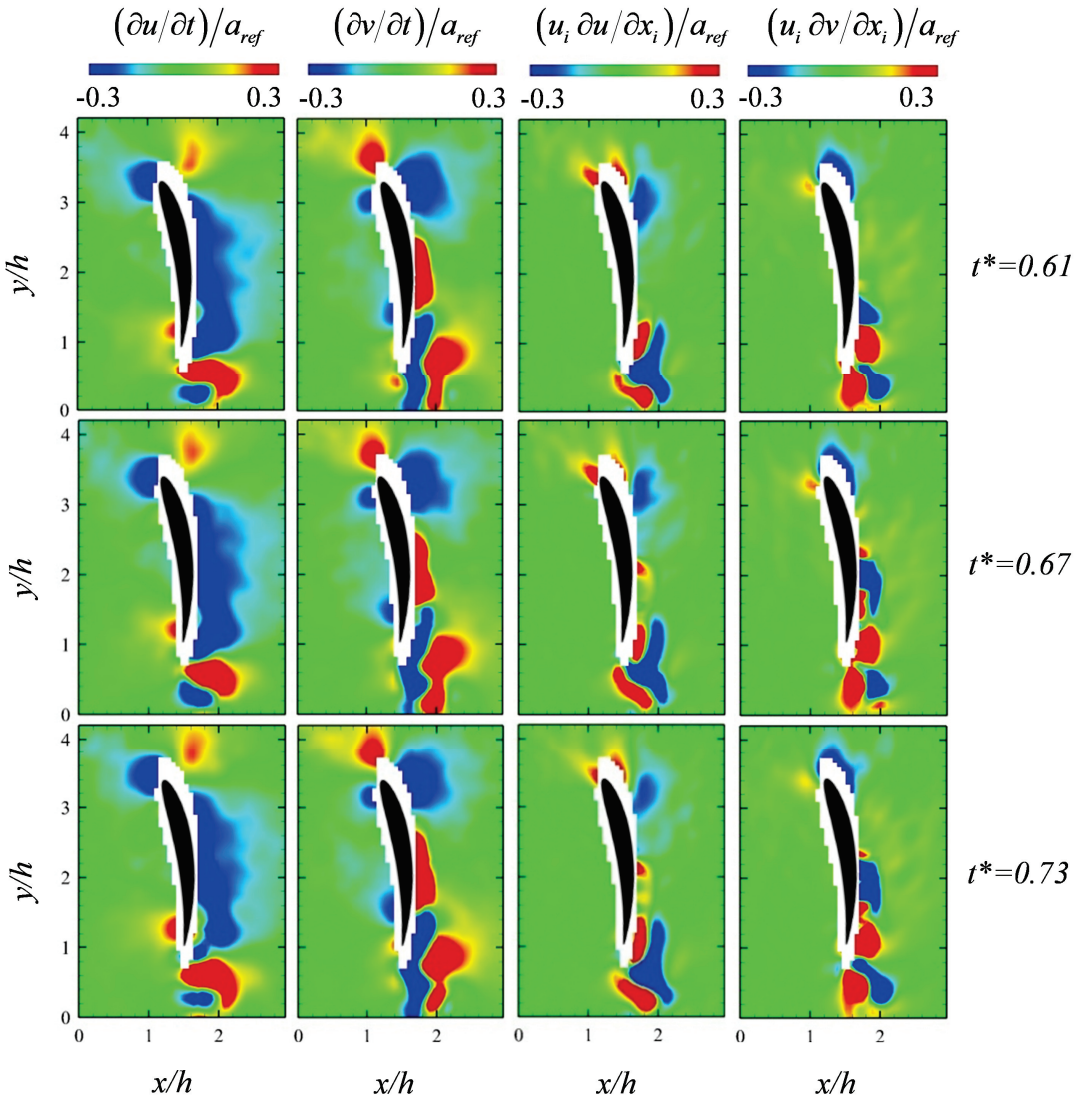

Figure 4.2: Contour plots of three consecutive instantaneous time-resolved axial and tangential local acceleration fields and axial and tangential convective acceleration fields for *Case 2*

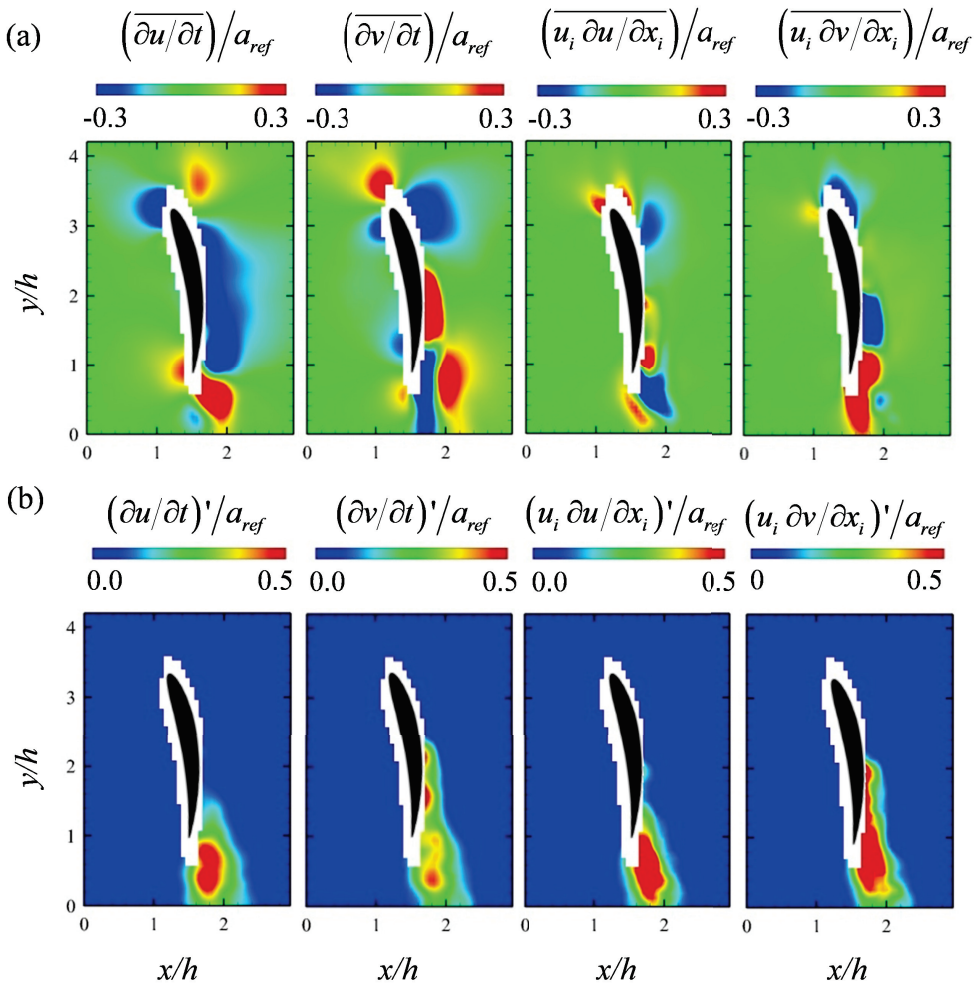

Figure 4.3: (a) Ensemble average and (b) standard deviation contour plots of the axial and tangential local acceleration fields and axial and tangential convective acceleration fields for *Case 2*

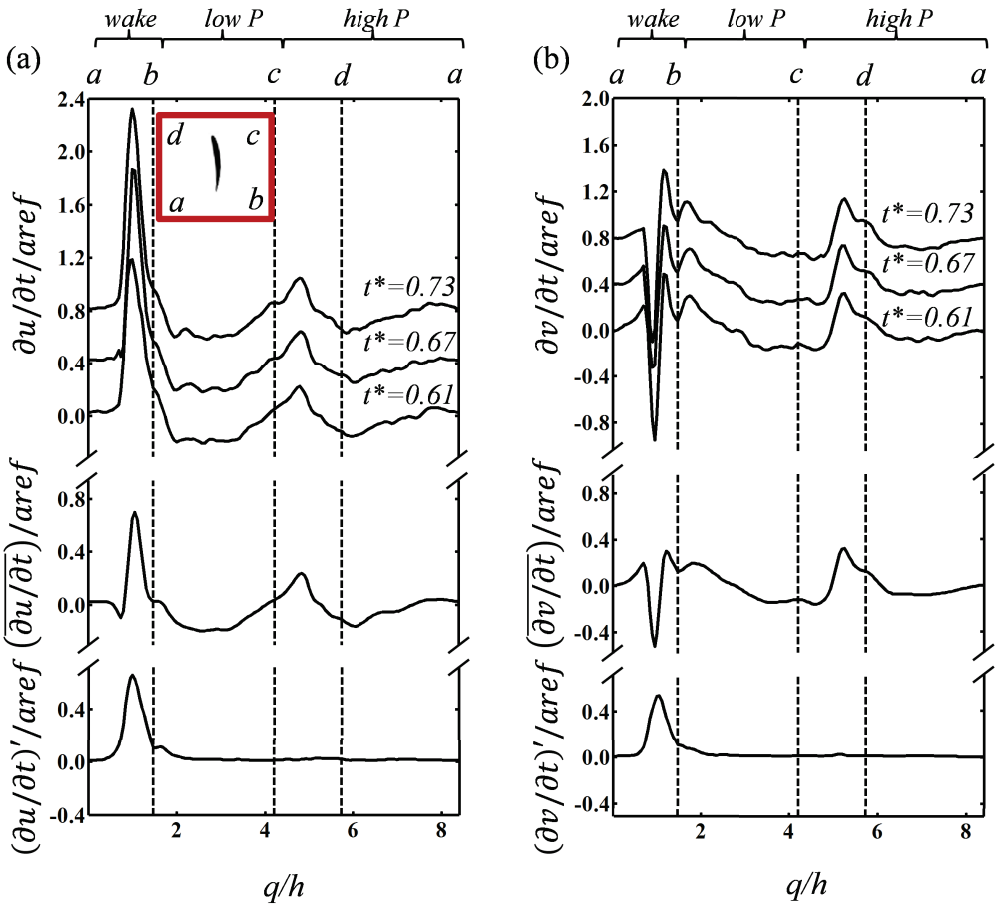

Figure 4.4: (a) Axial and (b) tangential local acceleration along the boundary of the control volume for *Case 2*. Each plot includes the results for three consecutive instantaneous measurements, the ensemble average and the standard deviation. A 0.4 offset of is used to separate the three instantaneous cases

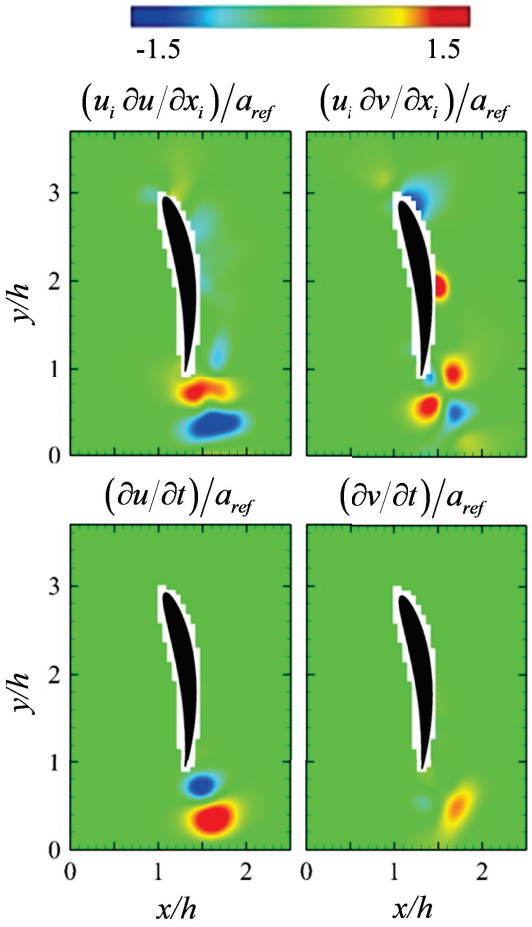

Figure 4.5: Contour plots of the time-resolved axial and tangential local acceleration fields and axial and tangential convective acceleration fields from the time-averaged POD for *Case 2*

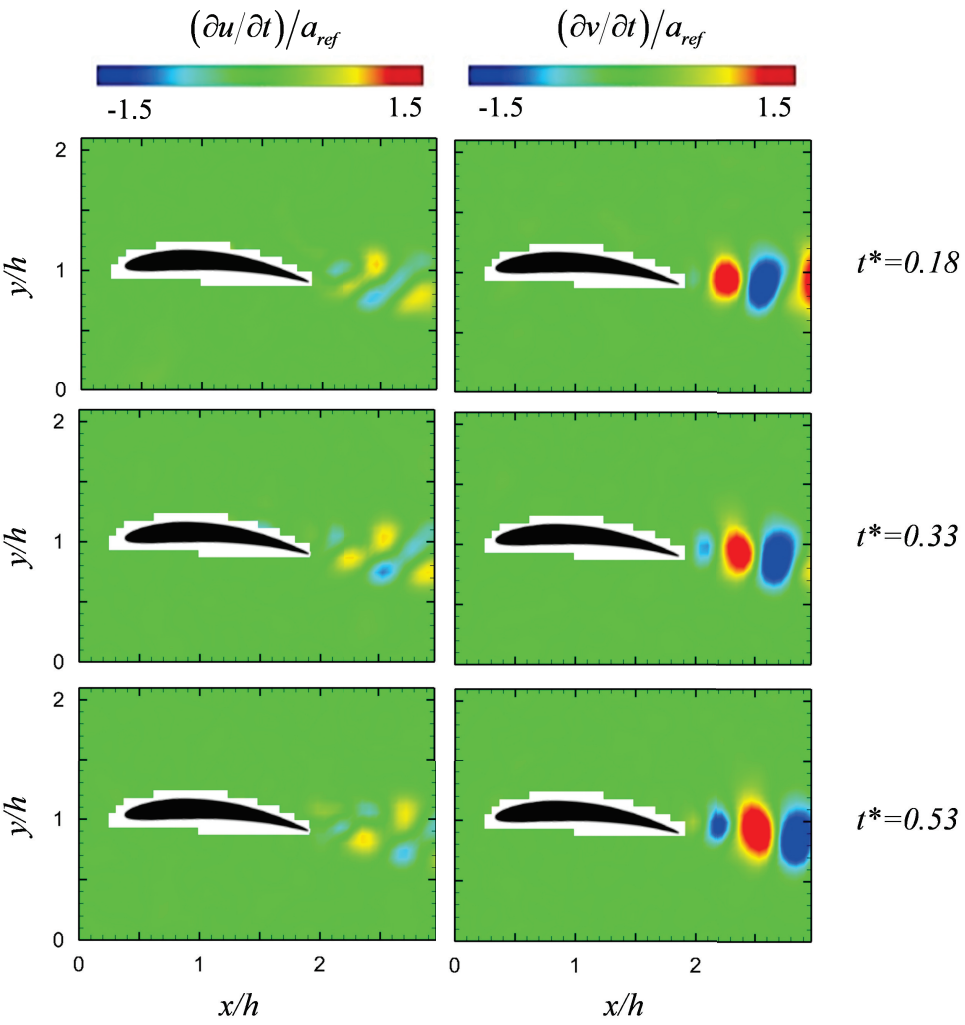

Figure 4.6: Contour plots of three instantaneous time-resolved axial and tangential local acceleration fields for *Case 3*

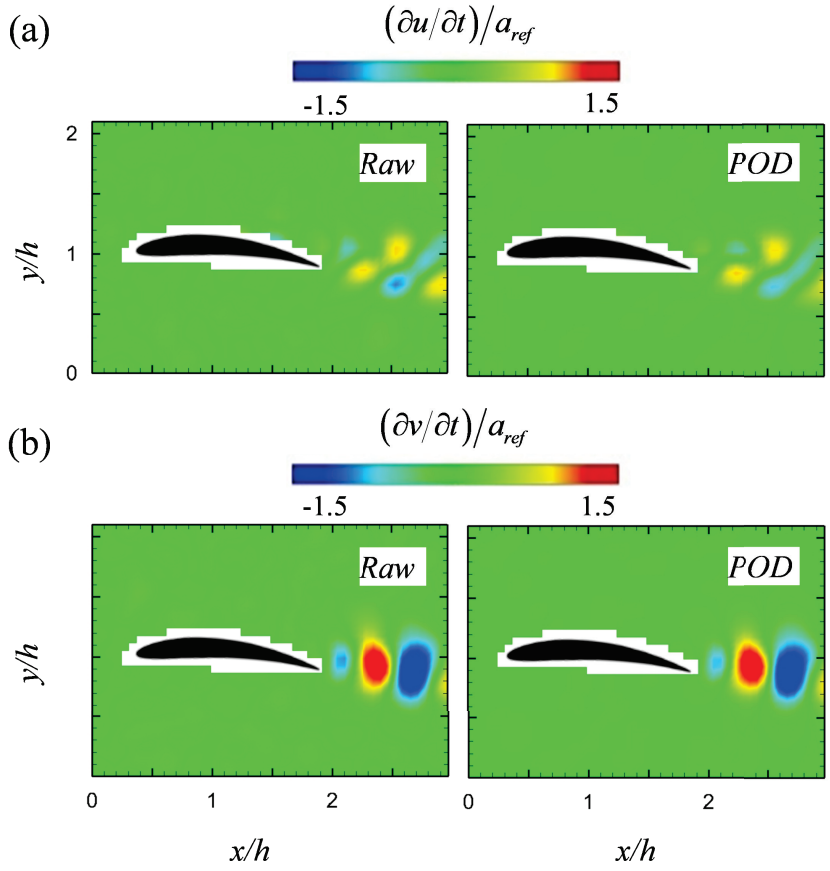

Figure 4.7: Comparison between raw data and 4-modes POD data for *Case 3*. (a) Local axial acceleration and (b) local tangential acceleration

Chapter 5

Pressure evaluation

Having resolved the instantaneous local and convective acceleration, the axial and tangential pressure gradients are simply the negative of the sum of those two accelerations in the axial and tangential direction respectively. For conciseness a time-resolved evolution of the pressure gradients is not included as it is just the sum of those two terms shown in Fig 4.2. Although not presented, it shows the same characteristics already described in Figs. 4.2 and 4.3 with only changes in the wake as the vortex shedding creates regions of alternating high and low pressure downstream of the trailing edge. The calculated pressure gradients at the inner and outer boundaries are used as Neumann boundary conditions to solve for the pressure field from the modified PPE (Eq. 2.11). The pressure term is needed to compute forces from the integral momentum equation.

5.1 *Case 1*: High-rpm water turbine

A typical quasi-instantaneous pressure field calculated using the PPE for the flow around the blade airfoil is shown in Fig. 5.1a. All the terms in the equation are obtained from the derivatives of the velocity fields obtained from the PIV measurements. The pressure differences are non-dimensionalzed by the dynamic pressure at

the radial station $r_z = 0.85R$

$$p_\infty = \frac{1}{2}\rho\left(U_\infty^2 + (\Omega r_z)^2\right) \tag{5.1}$$

The contour plot shows that there is a region of high pressure where the velocity is the smallest at the leading edge. It also shows a region of low pressure corresponding to the flow accelerating in the upper part of the blade. The maximum residual error when solving the Poisson equation was 0.002 which is slightly higher than the residual error found during the validation of the method in Sec. 2.5; however, small compared to the PIV errors. This maybe be due to the inclusion of inner boundaries within the field of view. When comparing the quasi-instantaneous pressure field in Fig. 5.1a to the average pressure field in Fig. 5.1b, the average pressure show the same effects previously discussed but there is an overall reduction in pressure intensity due to the variations in the instantaneous pressure field, especially in the wake.

The quasi-instantaneous and averaged pressure fields calculated from the PPE in Figs. 5.1a and 5.1b can be compared to the pressure fields calculated from the Bernoulli equation in Figs. 5.1c and 5.1d. This later method has been used in the literature for calculating the averaged pressure field from a rotating frame of reference, although it is known to be accurate only far from the blade and outside the wake flow. A comparison shows that the pressure field intensity is smaller near the blade for the Bernoulli method. This is due to the method not taking into account the local acceleration which is important near the blade for stationary frames of reference. This shows that the local acceleration should not be neglected for these measurements, and that the pressure field around a turbine blade calculated from the Bernoulli equation will be underestimated. This finding can be extrapolated to the forces in the blade which should also be underestimated when using the Bernoulli equation as discussed in the next chapter (Ch. 6).

One of the main variables that contributes to the calculated force is the pressure gradient which results from the differences in pressure across the blade surface. The typical instantaneous pressure gradient field in the x-direction calculated using the Navier-Stokes equation for the flow around the turbine is shown in Fig. 5.2a. The contour plot shows a high positive pressure gradient in the upper part of the blade responsible for the acceleration of the flow and a high positive and negative pressure gradient at the leading edge responsible for the stagnation point and where the velocity is the smallest. To validate the results obtained from the PPE, the instantaneous pressure gradient can also be obtained by taking the spatial derivative of the pressure field obtained from the Poisson equation. A comparison between the calculated instantaneous pressure gradient from the Navier-Stokes equation in Fig. 5.2a and the recovered pressure gradient from the Poisson equation in Fig. 5.2c shows a good agreement, which helps validating the numerical calculations. The higher differences are found in the wake since the acceleration term is not properly resolved there. In addition, Figs. 5.2b and 5.2d show the mean pressure gradient calculated from the Navier-Stokes equation and Poisson equation respectively, showing the common characteristics of its typical instantaneous pressure gradients. Although not shown for brevity, similar results are obtained for the pressure gradient in the y-direction as those in the x-direction for the two methods discussed.

The integration of the pressure is performed around the surface of a control volume within the field of view with a size $52 \times 16mm$ that encloses the entire cross section of the airfoil and extends beyond the boundary layer. As part of solving for the forces, an accurate calculation of the quasi-instantaneous pressure around the external control volume boundary is needed. Typical pressure values around the control volume boundary are shown in Fig. 5.3a for the three methods discussed in Section 2.5, Poisson, Bernoulli and spatially-integrated pressure. Results from the proposed Poisson method are much larger in magnitude to those from the Bernoulli method.

As discussed previously, these differences are due to the acceleration term which is properly resolved in the PPE but neglected in the Bernoulli equation. Due to the importance of the acceleration term in a stationary reference frame when considering a rotating blade, Bernoulli cannot be applied. In the other hand, in a rotating reference frame where the unsteady term contribution is not that significant Bernoulli has been commonly used. However, the Bernoulli method is inefficient when unsteady flow or vortical structures are presented in the wake even in the rotating frame and the Poisson method needs to be applied. A comparison between the proposed PPE and the spatially-integrated pressure method show significant differences as well. While qualitatively the results are similar, in the case of the spatially integrated pressure method, different integration paths result in different pressures obtained which for a scalar integration it should be independent of the integration path. Furthermore, this method is unable to recover the reference pressure value at the end of the boundary integration as the result of the marching solution scheme applied to an instantaneous PIV image where any small error is compounded. This justifies that the calculated pressure at the end of the spatially integration in Fig. 5.3a is different from the one it started with, even though it is a closed path and should return to the same point. In addition, this effect becomes larger by increasing the size of the control volume. This shows that the spatially integrated pressure method should not be used to calculate the instantaneous pressure.

A different situation appears when calculating the average pressure around the external boundary. The mean boundary pressure using the Bernoulli method deviates from the Poisson method due to the local acceleration term being neglected as was the case in the instantaneous pressure calculation. However, the mean pressure gives similar results when the spatial-integration is used. In that case, shown in Fig. 5.3b, the spatially integrated pressure and the PPE methods are in good agreement. When comparing the results between the instantaneous and mean integration methods, the

later one seems to almost recover the reference pressure value at the end of the boundary integration due to an averaging of the random error. Furthermore, the results for the instantaneous and mean Poisson methods are very similar which indicates the robustness of the method. A closer look at the error in the recovered pressure for the spatial-integration method is shown in Fig. 5.4 as a function of the control volume size. The figure shows that the error decreases with decreasing the size of the control volume. This is expected since the total propagation error will decrease for smaller number of integration steps.

5.2 *Case 2*: Low-rpm water turbine

5.2.1 Raw data

A typical time-resolved evolution of the instantaneous pressure field around the blade is shown in Fig. 5.5. The pressure is non-dimensionalized by the dynamic pressure (Eq. 5.1). The maximum residual error when solving the PPE was 0.0018, which is similar to the residual error found in *Case 1*. This is the first time the instantaneous pressure field has been resolved for a rotating airfoil. There are two common features in all time steps in Fig. 5.5. One is the region of high pressure close to the leading edge of the airfoil and the other is the region of low pressure in the upper part of the blade (where the flow is accelerating). What is perhaps more revealing is that pressure is changing within the recirculating bubble from negative to almost reference pressure. This can be explained by the change from low pressure values near the leading edge (blue) to the reference pressure (green) near mid-cord which would result in flow retardation and recirculation. Further downstream, still on the upper side of the blade, a low pressure region is again found which accounts for the region where vortices detach from the blade as part of shedding onset. Once in

the wake, a low pressure is observed surrounded by near reference pressures (green). This is a complex region shaped by both the long vortex detachment process from the trailing edge and the upper blade and by the shedding of vortices of opposite circulation that follows. A closer wake inspection reveals a local minimum pressure close to the vortex cores. However, due to the high differences in pressure around the blade, that local minimum appears unclear in the contour plot.

The mean pressure field in Fig. 5.6a shows features similar to the instantaneous pressure fields in Fig. 5.5; however, the pressure is filtered during the averaging process. Nevertheless, the contour plot of the pressure root mean square in Fig. 5.6b reveals major variations of the pressure occurring in the wake and the recirculating bubble. These variations reach values near the reference pressure.

Time variations in pressure can be quantitatively evaluated from instantaneous pressure plots around the external boundary as shown in Fig. 5.7. The normalized x-axis shows the line path along the lines corresponding to a-b, b-c, c-d and d-a in Fig. 2.5. The figure shows in b-c the effect from the lower pressure in the upper side of the blade. It also shows in c-d-e the effect from the higher pressure in the lower side of the blade. As expected, only in the wake does the pressure vary significantly during the three consecutive instants in time shown due to the vortices crossing the labeled a-b line. This is described by a sharp and narrow low pressure for $t^* = 0.61$ at $q/h \sim 1$ that changes in time ($t^* = 0.67$ and 0.73). This figure also shows the calculated mean pressure which is in good agreement with the instantaneous measurements except, again, in the wake where the instantaneous pressure fluctuates due to the passing vortices. In addition, the standard deviation plot in Fig. 5.7 shows that the main pressure fluctuations ($\sim 28\%$) occur in the wake region similar to previous observations when evaluating the acceleration and velocities. This good agreement between instantaneous and mean pressures also indicates the robustness of the PPE method

used.

5.2.2 POD analysis

A comparison between both raw and reconstructed pressure from the first 2 most energetic modes is shown in Fig. 5.8. The pressure fields from the phase-averaged POD analysis are filtered, especially in the wake. However, it preserves the main flow features. This is again probably due to the filtering of secondary frequencies that may be presented during the shedding process. The pressure term in the calculated forces contains a high peak frequency at double the shedding frequency (observed in *Case 2*); therefore, by just considering the first 2 modes, results of the calculated pressure at the wake are expected to deviate from the raw data.

5.3 *Case 3*: Stationary airfoil

5.3.1 Raw data

For the case of the stationary airfoil, the pressure shows similar features that the ones obtained for *Case 2* as shown in Fig. 5.9. For the three instantaneous measurements, a high pressure zone at the leading edge as well as the low pressure zone at the upper side of the airfoil are observed. In addition, convected low pressure features are identified at the wake which are coincident to that of the vortex cores.

5.3.2 POD analysis

A comparison between pressure fields from raw and 4-modes POD data is shown in Fig. 5.10. The pressure field seems to be slightly filtered from the POD analysis, preserving the same features observed in the raw case. In comparison to *Case 2*,

differences in pressure at wake are not deviated when compared to the raw data, supporting the need of including secondary frequencies for more accurate calculations.

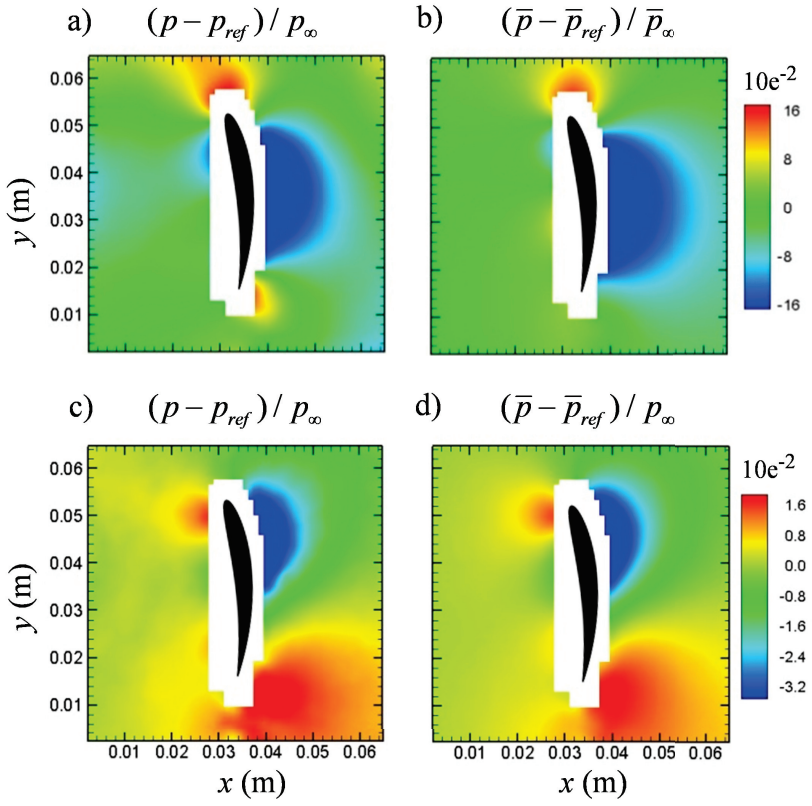

Figure 5.1: Contour plots of the pressure field around the airfoil for *Case 1* for a) instantaneous and b) mean pressure fields obtained from the PPE, and c) instantaneous and d) mean pressure fields obtained from the Bernoulli equation

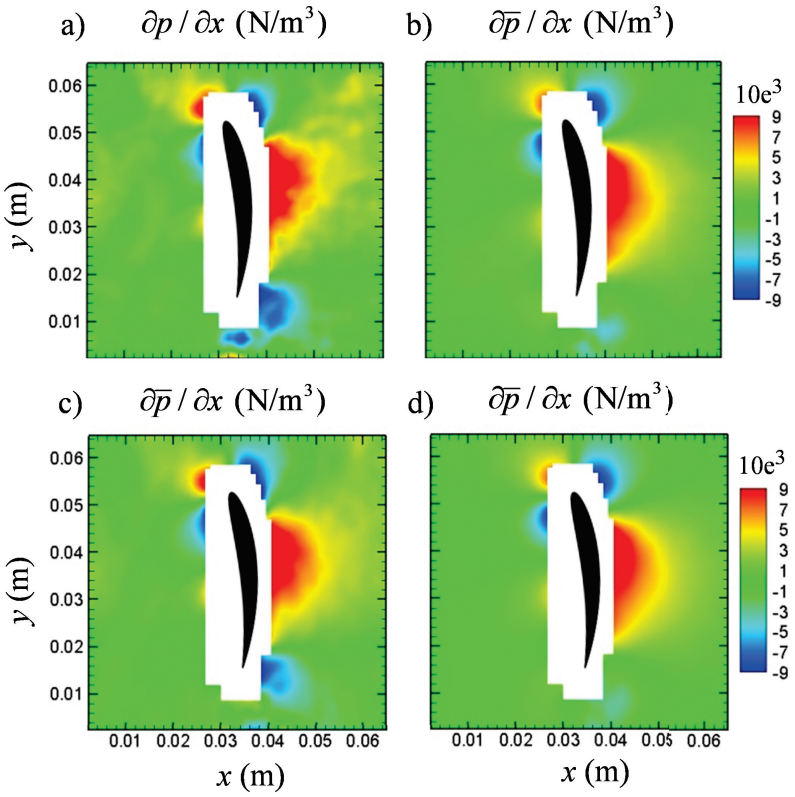

Figure 5.2: Contour plots for *Case 1* of a) instantaneous and b) average pressure gradients in the x-direction calculated from the Navier-Stokes equation and c) instantaneous and b) average pressure gradients in the x-direction calculated from the PPE

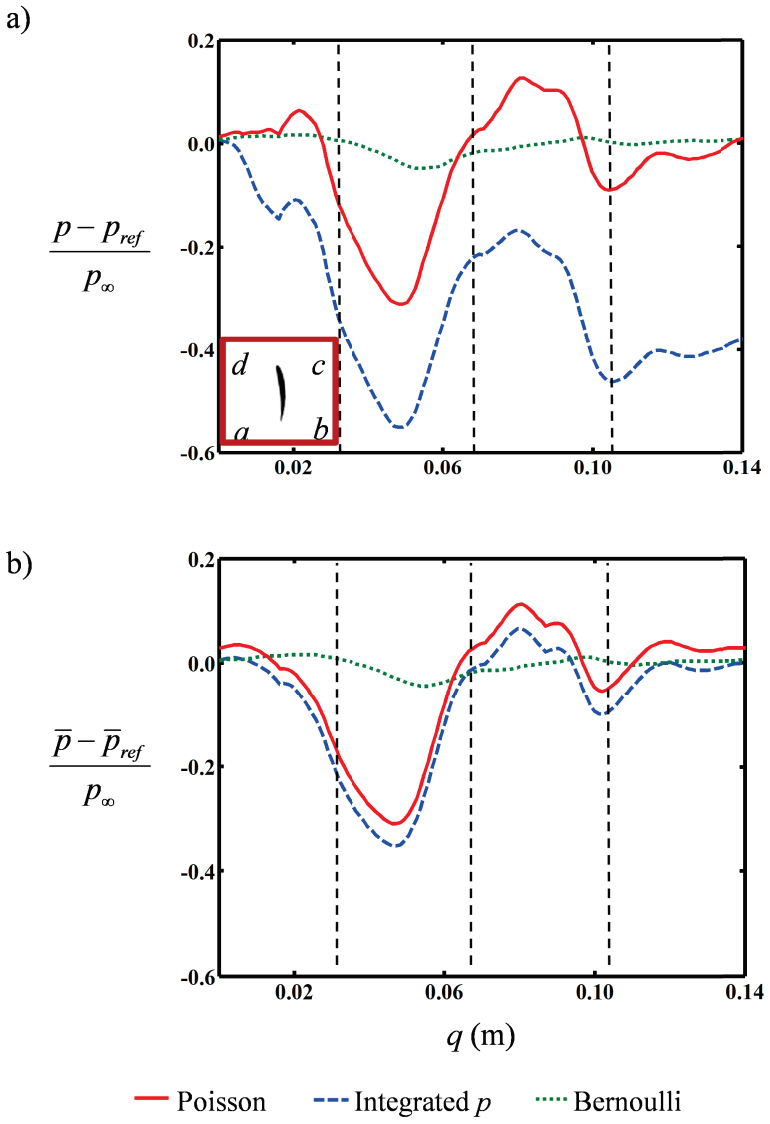

Figure 5.3: a) Instantaneous and b) mean pressure along the external boundaries of the smallest control volume ($52x26mm^2$) for *Case 1*. The origin is at $q = 0$ for all three methods (see Fig. 2.5 to find the corresponding points for *a*, *b*, *c* and *d* in the control volume)

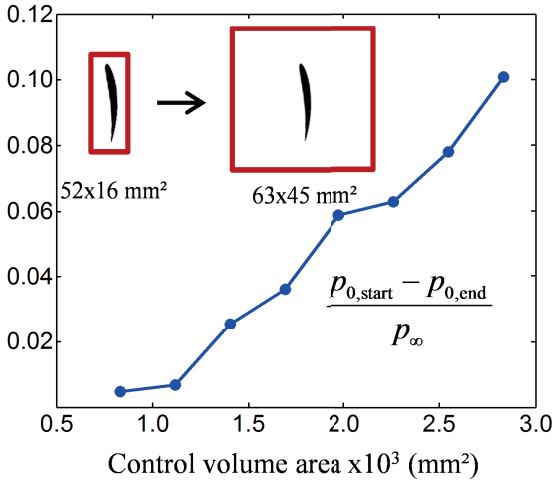

Figure 5.4: Measured error in the spatially integrated pressure method as a function of the size of the control volume for *Case 1*, where p_{0start} and p_{0end} are the calculated pressures at $q = 0$ at the beginning and at the end of the integration respectively

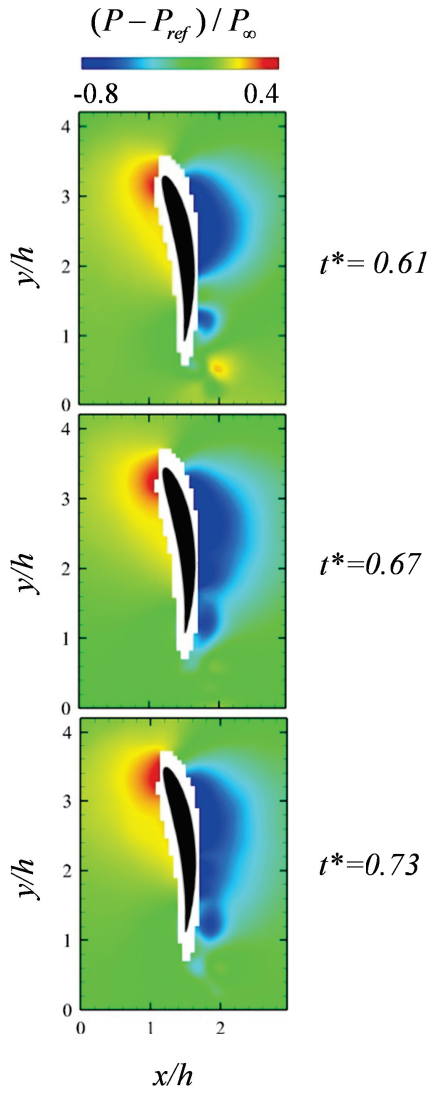

Figure 5.5: Contour plots of three instantaneous time-resolved pressure fields for *Case 2*

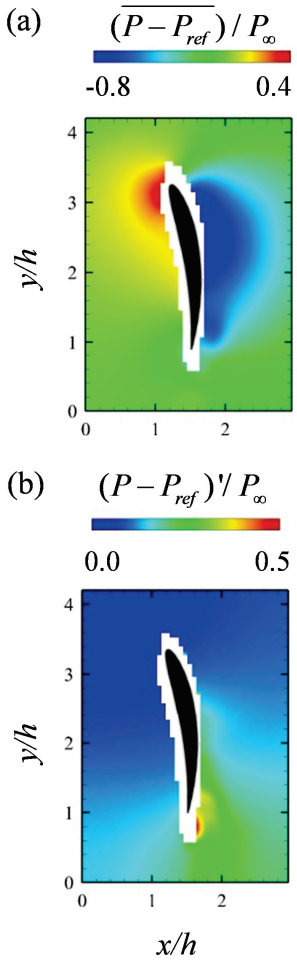

Figure 5.6: (a) Ensemble average and (b) standard deviation contour plots of the pressure field for *Case 2*

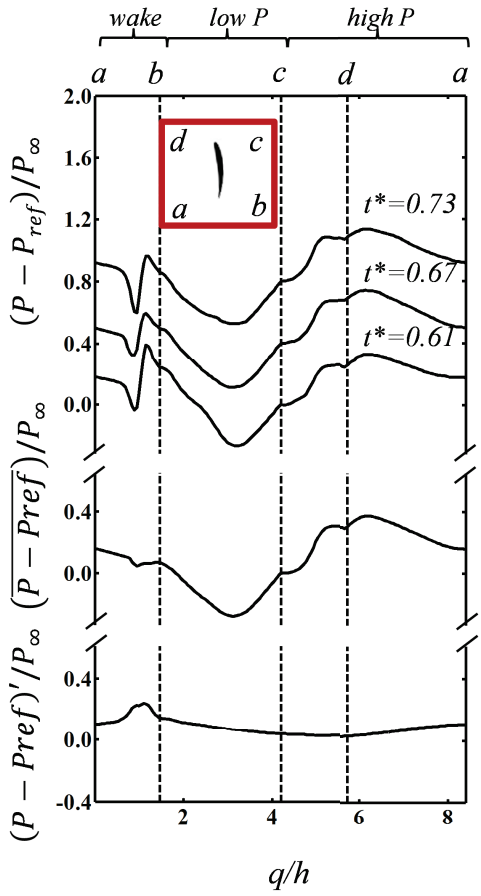

Figure 5.7: Calculated pressure along the boundary of the control volume for *Case 2*. Each plot includes the results for three consecutive instantaneous measurements, the ensemble average and the standard deviation. A 0.4 offset of is used to separate the three instantaneous cases

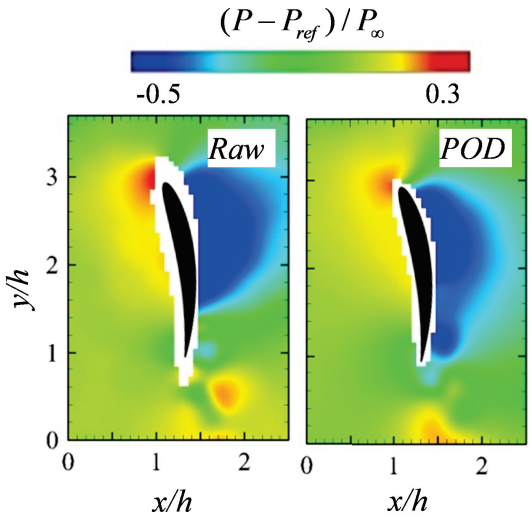

Figure 5.8: Comparison between raw and 2-modes POD pressure fields for *Case 2*

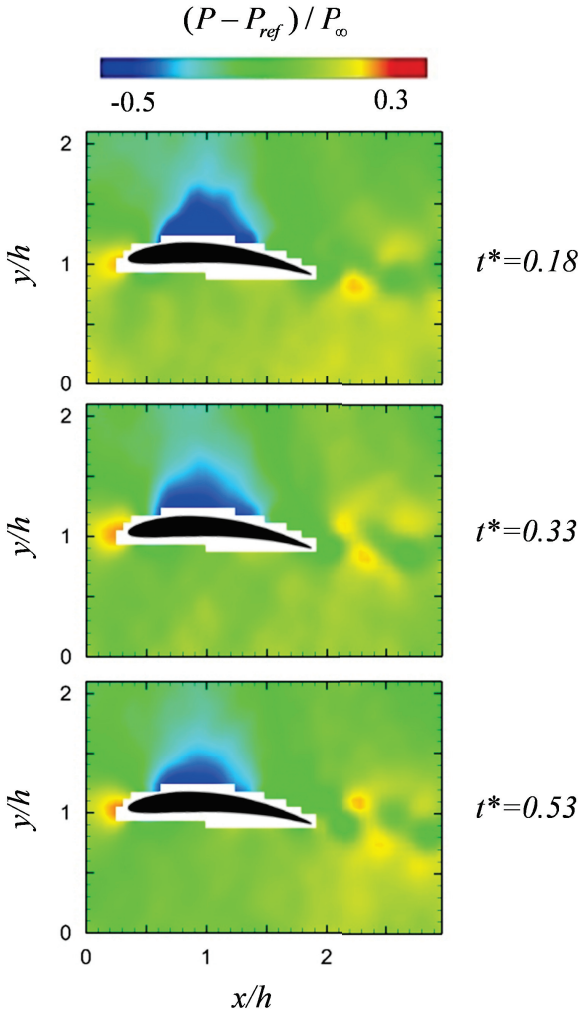

Figure 5.9: Contour plots of three instantaneous time-resolved pressure fields for *Case 3*

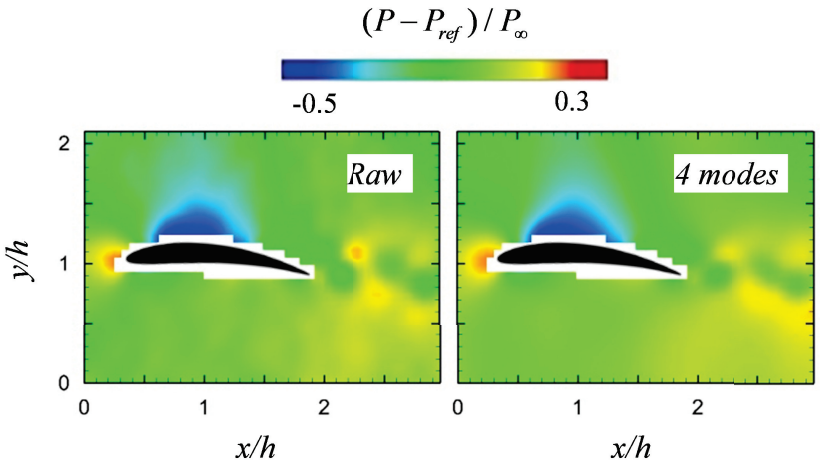

Figure 5.10: Comparison between raw and 4-modes POD the pressure fields for *Case 3*

Chapter 6

Force evaluation

In this chapter, aerodynamic forces created by moving and stationary airfoils are calculated and discussed for the three cases of study. The contribution of each term in the integral momentum equation is also evaluated. In addition, the robustness of the modified PPE method is demonstrated by showing the independence of the calculated forces with both control volumes size and origin of the coordinates system. Moreover, the PPE method is compared to other methodologies used in the past. Calculated forces are combined with flow structures observations to disclose relations vortex-force. This allows us to create a model of that relationship by identifying minimum and maximum forces with the shape of the wake simultaneously as shown in the next figure. The proposed model is briefly explained here and will be disclosed and further discussed in this chapter. The model shows how the vortex formation, growth and release affect the force fluctuations. The Δ symbol refers to the incremental value about the mean force. The arrows close to those incremental values of the force in this figure indicate the direction of the force fluctuations about the mean value. Plus and minus signs inside the vortex indicate the sign of the vorticity. Maximum drag is found when the trailing vortex reaches it maximum size. Maximum lift follows after the trailing edge vortex is detached and the suction side vortex is initially formed within the recirculating area. Then, minimum local drag is found when the suction side vortex grows about the half of its maximum size. Subsequently, maximum local drag occurs when the suction side vortex reaches its maximum size. Afterwards, an

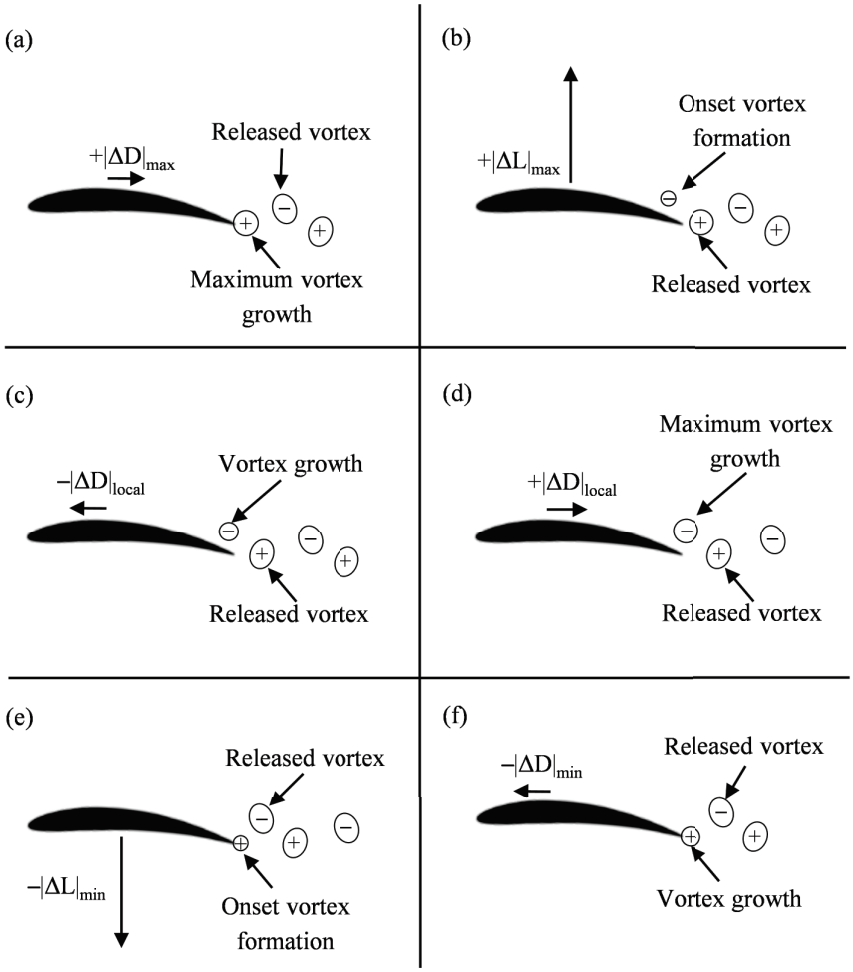

Model showing the relation between force fluctuations and the shape of the wake for one shedding cycle for (a) absolute maximum drag, (b) maximum lift, (c) local minimum drag, (d) local maximum drag, (e) minimum lift and (f) absolute minimum drag

initial trailing edge vortex formation and a release of the suction side vortex cause minimum lift values. Finally, minimum drag is found when the trailing edge vortex grows about the half of its maximum size.

6.1 *Case 1*: High-rpm water turbine

The quasi-instantaneous forces created by the rotor blade per unit length are resolved by the integral momentum method described in Sec. 2.6. Once the pressure on the

boundaries is known, an analysis of the contribution of each integral in Eq. 2.19 to the calculation of the tangential and normal forces is performed. The contribution to the normal force was 36, 2, 62 and $\sim 0\%$ for the unsteady term, the convective term, the pressure term and the viscous term respectively. The contribution to the tangential force was 21, 69, 10 and $\sim 0\%$ for the unsteady term, the convective term, the pressure term and the viscous term respectively. This dimensional analysis shows the importance of the unsteady, convective and pressure terms in a stationary reference frame, while the viscous term is negligible.

Forces generated by the blade can now be evaluated using Eq. 2.19. These are tabulated in Table 6.1 for the three methods discussed above (PPE, Bernoulli and integrated-pressure) as well as for the BEM theory. The table shows mean and the standard deviation for the tangential and normal force coefficients exerted by the blade for the smallest control volume (since the integrated pressure method error is smaller at smaller control volumes for better comparison). Although there is no exact theoretical solution known, the BEM theory, which is a modified 2D model, has been widely accepted as a good estimation in wind turbines design. For the present study this model was revised to include Prandtl (Prandtl & Betz, 1927) and Glauert (Glauert, 1935) corrections. Using the calculated forces from this theory as a reference, the results obtained by the three methods will be discussed.

First, the calculated mean normal forces are considered. Both results from the Poisson and spatially integrated pressure methods are 14% and 15% lower than the one predicted by the BEM theory. These lower values are typical when compared to the ideal 2D conditions from the theory and the propagation error from PIV. On the other hand, the Bernoulli method largely under predicts the normal force since the acceleration term is neglected and it is not recommended for these measurements.

Considering that the blade is rotating free at a constant speed, the total tangential

force when integrating over the full length of the blade should be zero. This means that while the inner part of the turbine produces a positive tangential force per unit length, the outer part produces a negative force per unit length. Measurements are taken at $85\%R$ where a likely negative or close to zero force is expected. The calculated mean tangential force from the PPE method is in good agreement with the small negative force predicted by the BEM theory. In addition, a good agreement is obtained from the mean force from the integrated pressure method. However, more deviated results are obtained from the Bernouilli equation.

There is a large standard deviation (RMS) in the calculated instantaneous forces when using the integrated pressure method due to the error associated with accurately resolve the pressure at the boundaries. On the other hand, the Bernoulli method had the smallest standard deviation of the three methods but it does not resolve the actual temporal variations of the velocity resulting in the pressure and the forces being under resolved. Therefore, neither method is recommended for any instantaneous force calculations. For the Poisson method, the ± 0.10 and ± 0.04 standard deviations in the calculated instantaneous forces is likely due to the small vortex shedding. Otherwise, these results are within half standard deviation from the BEM theory and it is proposed for measurement of mean forces.

When using the integral momentum theorem, the calculated forces should be independent of the control volume size used for the measurements as long as the control volume encloses the entire cross section of the airfoil and extends beyond the boundary layer. To test for any effect that the control volume size might have on the calculated forces, the measurements are repeated for eight different size volumes that ranged from 63×45 mm for the largest to 52×16 mm for the smallest. Results are shown in Fig. 6.1 for the mean tangential and normal forces as well as their standard deviations

as a function of the volume size. Both forces calculated from the Bernoulli and the integrated pressure methods are dependent on the volume size for the range of volumes considered which makes the methods inaccurate. These two methods show a larger standard deviation for bigger control volumes. In addition, the integrated pressure method only approaches the tangential and normal forces obtained from the Poisson method for the smallest control volumes close to the airfoil. This is supported by the results shown in Fig.5.4, where the reference pressure is almost recovered for small volumes. Only the modified PPE method satisfies the condition that the calculated tangential and normal forces and their standard deviation should be independent of the control volume size as observed in Fig. 6.1. For this method, the variation in the calculated forces is small with a standard deviation of 0.03 and 0.02 for the tangential and normal forces respectively. This shows the method's stability for calculating blade forces. When combined with the earlier observations about the quality of the pressure and pressure gradient fields as well as the error analysis, it shows that the PPE method is a robust method for force measurements.

6.2 *Case 2*: Low-rpm water turbine

6.2.1 Raw data

The instantaneous load per unit length on the blade is obtained from the integral momentum PPE method described in Sec. 2.6. The integration is performed on the control area labeled *a-b-c-d* in Fig. 2.5. Three typical time series of the normalized instantaneous normal and tangential forces, C_n and C_t, are shown in Fig. 6.2.

Time-resolved series expands above half a shedding cycle (limited by the size of the field of view). It shows during that time the normal force varying up to $\sim 40\%$ while the tangential force remains relatively constant ($\sim 10\%$). A closer inspection of the

integral momentum equation terms shows how they contribute to the total forces. These terms are the acceleration, pressure and convective term, and they are also plotted in Fig. 6.2. For the normal force, the convection term, C_{nc}, has a negligible contribution, while the acceleration term, C_{na}, is important and has a near constant value. Nevertheless, the largest contribution to C_n is from the pressure term, C_{np}, with C_n closely following the same trend as C_{np}. For the tangential force, C_t, the main contribution is from the convective term, C_{tc}. Both contributions C_{ta} and C_{tp} are small but they show opposing trends and when one increases the other decreases and vice versa. This opposing behavior, circled in Fig. 6.2 for clarity, was characteristic of most time series in the present study and has also been observed in the literature for vortex shedding on a square cylinder (Kurtulus *et al.*, 2006). A closer inspection at the instantaneous vorticity fields reveal that this opposing behavior between C_{ta} and C_{tp} can be associated with the time period when vortices are released (detached) from the trailing edge of the airfoil. These observations are typical for all the time series evaluated and should be considered a common signature during vortex shedding. The importance of the unsteady, convective and pressure terms can also be shown from averages values. For instance, the main contributions to the normal force were 39 and 60 % for unsteady and pressure terms respectively. In the case of the tangential forces, the main contributions were 20, 63 and 17 % for unsteady, convective and pressure terms respectively.

When using the integral momentum PPE equation, the calculated forces should be independent of the control area size used for areas enclosing the blade cross-section and extending beyond the boundary layer. To test the independence of the method from the control area selected, the forces are calculated for nine areas ranging in size from $82 \times 60\, mm^2$ to $55 \times 23\, mm^2$. The instantaneous values of the force coefficients are shown in Fig. 6.3a. They reveal independency of the control volume size with a maximum measured variation between control volumes for all the sets of 0.07 and

0.05 for the normal and tangential force coefficients respectively. The mean and standard deviation of the force coefficients are shown in Fig. 6.3b. The standard deviation between all calculated mean forces for the different control volumes is 0.04 and 0.02 for the tangential and normal force coefficients respectively, which are small compared to the mean value of the forces, ensuring the area independence of this method. A closer inspection at the integral momentum equation terms shows how they contribute to the forces for the different areas selected. Although the force is independent of the control volume, the different terms in the equation are not. As a matter of fact when solving the integral momentum equation for larger areas, the acceleration term becomes more important and the pressure term contribution to the total force is smaller while the convective term remains small. Physically this can be explained by the fact that the pressure and convective term are line integrals that only need to be solved around the boundary while the acceleration term is a surface integral that needs to be solved in the entire area. As such, if the area enclosing the blade is large enough, the effect of pressure and convective terms will only be weakly felt at the boundaries. On the other hand, the acceleration term, which is written as a surface integral over the entire domain, can only increase as the domain increases.

Additionally, forces are calculated by using three other derived momentum equations as described in Sec. 2.6. These three methods are the *Noca* method or impulse momentum equation, the *Wu(adv.)* method or vorticity advection momentum equation and the *Bound* method or "flux" momentum equation and they are compared to the PPE method. Figure 6.4 shows the normal and tangential force coefficients for the four methods and for two different locations of the origin of the coordinates system. The changes in the origin of the coordinates systems is tested since Noca *et al.* (1999) reported anomalous changes in the forces due to this feature. The deviations were reported to be caused by the arm-moment introduced in calculating the moment of vorticity or velocity. Fluctuations in the normal force seems to be highly affected by

placing the origin at the wake for the *Noca* and *Wu(adv.)* cases compared to the origin at the center of the wake. On the other hand, higher fluctuation occur in the *Bound* method for the tangential force when the origin is located at the center of the airfoil compared to locating the origin at the wake edge. However, the PPE method is independent of the origin of the coordinates system. In addition, the smallest fluctuations are also found by using the PPE method for both tangential and normal forces.

To further validate the results, the tangential and normal forces measured are compared in Table 6.2 along with the theoretical model (BEMT). The model uses the BEM theory with the airfoil aerodynamic data collected from XFOIL. Similar models are widely used as a first estimation during the wind turbine design. From this table, theory and PPE results show a good agreement for the normal force (< 0.5 RMS) and more deviated results for the tangential force (< 1.6 RMS). It is reasonable to expect these variations in the forces considering that the BEM theory is a modified 1D model with some 2D and 3D corrections that cannot fully resolve the 2D flow and the complex features observed such as the shedding in the wake and the recirculating region. In short, the BEM theory has its limitations and it should not be taken as the actual force. The other three methods show high deviated mean results as well as high RMS values in addition to the origin of the coordinates system location dependence, which indicates that these three methods should not be used for these kind of measurements.

Although not showed for brevity, changes in the size of the control volume also affected the force fluctuations obtained by the other three methods, while the PPE method remained independent. In the next section, an impact of the size of the control volume size is analyzed.

In addition, forces from Wu(dif.) or vorticity diffusion momentum equation (Eq.

2.25) were calculated. Results showed an almost zero value for both tangential and normal forces. This can be explained by looking at Wu *et al.* (2007), since high vorticity difussion values happens within a small area close to the surface of the cylinder. Therefore, in this kind of experiments is difficult to capture any diffusion of the vorticity since the resolution needed to capture those features is high close to the surface of the object. However, it may be suitable for numerical simulations, where the area close to the object can be fully resolved.

Although not shown for brevity, similar results to the ones obtained for *Case 1* are found when applying the Bernoulli or the integrated pressure methods.

6.2.2 POD analysis

From the last section, the calculated force fluctuations values were unrealistic due to error propagation (up to 33% RMS using the PPE method). This was also observed by Charonko *et al.* (2010), who used a POD reconstructed velocity field to analyze the pressure. The error is noticeable reduced by using this method and it is applied in the present manuscript. Forces are calculated from the phase-averaged POD velocity field. Figure 6.5 shows the normal force coefficient for 1.5 shedding cycles and four different control volume sizes by just changing the location of the wake edge ($y/h|_{wake}$). Since the only frequency addressed by this method is the shedding frequency, all force functions will be periodic at this frequency and just one whole cycle is needed to characterize force fluctuations. This figure shows the similarity of the other three methods when calculating the normal force. However, even though the fluctuations are smaller than the ones found for the raw case, they still differ from the PPE method. In addition mean value, amplitude and phase are dependent of the size of the control volume for the three methods. On the other hand, mean value, amplitude and phase of the force calculated from the PPE method remains almost independent

of the control volume size and the RMS are noticeably reduced compared to the raw data case.

Larger differences between the other three methods are found when calculating the tangential force as shown in Fig. 6.6. In this case, the *Noca* method is more approximated to the solution obtained from the PPE. The other two methods produces more unrealistic results since negative values are obtained. The tangential force obtained by the PPE method seems to be almost constant when the wake edge is chosen to be very close to the airfoil trailing edge. This might be due to the higher resolution needed to resolve vortex formation. However, the calculated mean tangential force also seems independent of the control volume selected and slightly higher fluctuations are observed for wake edge locations far from the airfoil trailing edge.

Tangential and normal forces calculated from the POD method are compared in Table 6.3 along with the theoretical model (BEMT). In this case, theory and PPE results are in good agreement for both normal and tangential forces. The agreement is improved when compared to the agreement between raw data and theory. Mean forces slightly fluctuate around the theoretical values for different control volumes selected, supporting the force independent with the size of the control volume. The semi-amplitude of the periodic signal is also highly decreased compared to the raw data, producing more realistic results. Even though the other 3 methods decreases their RMS compared to the ones obtained from the raw data, unrealistic results are still produced. This is indicated by the high semi-amplitude of the force signals as well as their dependence with the control volume size.

6.3 *Case 3*: Stationary airfoil

6.3.1 Raw data

A similar analysis to the calculated forces for *Case 2* is also applied to the stationary airfoil (*Case 3*). Forces are calculated by just using the *PPE* and the *Noca* methods, since the other two methods (*Wu(adv.)* and *Bound* methods) have similar responses than the *Noca* method. Figure 6.7 shows the normal force coefficient for the two methods and four different locations of the wake edge of the control volume ($x/h|_{wake}$) and for three complete shedding cycles. As observed in *Case 1*, the smallest fluctuations are found for the PPE method as well as independence of the control volume selected. Higher fluctuations are found in the Noca method, especially for larger control volumes. In addition, fluctuations in the normal force are found by changing the origin of the coordinates system for the *Noca* case, while the PPE method remains independent.

The tangential force is shown in Fig 6.8 for the two methods and four different locations of the wake edge of the control volume. Smaller deviations are found for both methods compare to the normal force. In addition, both methods are in better agreement for this calculated force. Again, independence is found for the mean value of the tangential force with the size of the control volume by using the PPE method.

To further validate the results, tangential and normal forces are compared in Table 6.4 along with the numerical model (XFOIL). From this table, theory and PPE results show a good agreement for the normal force ($<$ 1.5 RMS) and the tangential force ($<$ 1.8 RMS). The RMS in this case is smaller than the one found in *Case 2* for the raw data. The other three methods show larger deviated mean results as well as large RMS values and origin location and control volume size dependence, which again indicates that these three methods should not be used for this kind of measurements.

6.3.2 POD analysis

From the last section, the calculated force fluctuations values were unrealistic due to error propagation. Figure 6.9 shows the normal force coefficient for 1.5 shedding cycles and four different control volume sizes by just changing the location of the wake edge. Again, just the PPE and Noca's method are considered since the other two methods give similar results to the ones calculated by Noca. Even though the RMS decreases for the Noca's method, mean value, amplitude and phase are still dependent of the size of the control volume. On the other hand, the mean value, amplitude and phase of the force calculated from the PPE method remains almost independent of the control volume size and the RMS are noticeably reduced compared to the raw data case.

The calculated POD tangential forces are shown in 6.10 for the same two methods explained above and four different positions of the wake edge. The *Noca* method in this case is more approximated to the solution obtained from the PPE. The force from the PPE method seem to be almost constant when the wake edge is chosen to be close to the airfoil trailing edge. Similarly to *Case 2*, this might be due to the higher resolution needed to resolve vortices formation. However, the calculated mean tangential force seems independent of the control volume selected and slightly higher fluctuations are observed for wake edge locations far from the airfoil trailing edge.

Tangential and normal forces calculated from the POD method are compared in Table 6.5 along with the numerical model (XFOIL). In this case, theory and PPE results are in good agreement for both normal and tangential forces. The agreement is similar to the comparison between raw data and theory. The RMS of the forces decreases compared to the raw data. However, the other three methods slightly decrease their RMS compared to the ones obtained from the raw data and unrealistic results are still produced.

6.3.3 Realtionship between vortical structures and forces

Several observations of the vortex shedding process and simultaneous calculations of the forces are needed to explain the physical process that relates the role of vortices on the force fluctuations. The evolution of lift, drag and circulation coefficients with time for three shedding cycles is shown in Fig. 6.11a, 6.11b and 6.11c respectively. Forces are calculated from the original velocity field (first row) and the modified velocity field from POD by using 10 modes (second row), 4 modes (third row) and 2 modes (fourth row). Lift, drag and circulation coefficients are fluctuating in a periodic way, consistent with that of the vortex shedding. The three POD cases show these variations clearly, since raw data contains errors that propagate as explained in Sec. 2.7 and the POD filters the velocity fields by just taking the main modes of the flow. Lift and circulation coefficients show a sinusoidal behavior at the shedding frequency. However, drag coefficient seems to fluctuate not just at the shedding frequency but also at double the shedding frequency with non-symmetric variations (except for the 2 modes case which only includes the contribution from the modes with the shedding frequency). For symmetric bodies in symmetric flows, variations of drag should occur symmetrically at double the shedding frequency rate. Lift, drag and circulation mean values remain almost constant while amplitude and noise decrease by decreasing the number of modes. In addition, the instantaneous values for lift and drag not only were independent of the size of the control volume selected, but also they were in phase. However, even though the amplitude and frequency for the calculated circulation are almost identical for different control volumes, the phase is essentially dependent on the x/h position of the right edge of the control volume $x/h|_{wake}$ (wake edge). In other words, the phase that simultaneously relates circulation with forces need to be found. One way of finding the right choice of the control volume's wake edge position $x/h|_{wake}$ for circulation calculations is by looking

at the zero phase differences between lift and circulation, since the lift is independent of the control volume selected and proportional to the circulation (Kutta-Joukowski theorem). However, since the circulation is periodic, there are multiple choices of the wake edge positions separated by $2\pi x/h$ (for distances where the edge of the control volume is close enough to the airfoil that vortex decay is negligible). The closest $x/h|_{wake}$ for what the circulation is in phase with the lift coefficient is close enough to the airfoil to differentiate between attached and detached vortices. This selection is also capturing the earliest deflection of the streamlines occurring close the trailing edge of the airfoil. Moreover, any $x/h|_{wake}$ selection that includes the exact same variations of streamlines will be in phase with the lift and also will give the same circulation values, this is, every $2\pi x/h$. This can be explained by looking at the total vorticity included in calculating the circulation (Eq. 2.28), since every shedding cycle two vortices of opposite circulation values are shed into the wake.

To identify the main frequencies of the force signals, a power spectral density analysis is performed. The dominant frequency for the lift signal is the shedding frequency as shown in Fig. 6.12a for the four different cases, indicating high-amplitude periodic fluctuations every shedding cycle. Additionally, a secondary small peak at double the shedding frequency indicates very small amplitude and periodic changes of the lift every half shedding cycle. The power spectra for the 10 modes case is almost identical than the original case in terms of energy content and energy features in agreement with Holmes *et al.* (1998). For these two cases, a low frequency forming peak is shown, indicating that very slow fluctuation of the lift will occur as well, in agreement with the frequencies observed in modes 5, 6 and 8. There is also two peaks reveled at high frequencies ($15f_{shed}$ and $19\mathrm{f_{shed}}$) with smaller energy clearly seen for the 10 POD modes case. Those two peaks are probably coming from the instability created within the separated shear layer (modes 5, 7 and 8), attributed to Kelvin-Helmoltz instability and observed in airfoils wake development (Yarusevych *et al.*, 2006). However, the

temporal and spatial resolutions for this experiment do not resolve properly those vortices created within the shear layer. Nevertheless, the POD method does a great work capturing those features. For the drag signal, the PSD reveals three main peaks as shown in Fig. 6.12b. There is a low frequency peak compared to the shedding frequency, which is probably amplified from the low frequencies found in the velocity in the x-direction and reveals very slow variation of the drag force in time at that frequency (modes 5, 6 and 8). In addition, two main frequencies with about the same energy content are found for the drag signal consistent with those found for the velocity in the x-direction. One peak is found at the shedding frequency and hence, periodic variations are expected every shedding cycle at the shedding frequency. The other peak occurs at double the shedding frequency and therefore, periodic changes are also expected every half shedding cycle. For symmetric bodies in symmetric flows, this last frequency should be dominant. Again, the power spectra of the original and the 10 modes cases are almost identical for the drag coefficient. Moreover, two small high-frequency peaks are found as the ones found in the PSD of the lift coefficient. The peak in the PSD of the circulation (Fig. 6.12c) corresponds to the shedding frequency. For an airfoil in steady motion the circulation should be constant (Kelvin theorem). However, due to vortex shedding, the circulation around the airfoil for a fixed control volume is periodically changing at the shedding frequency rate.

In order to identify the value of the forces with the shape of the wake, the vortical structures are found by using the Q-identification method (Hunt *et al.*, 1988), since vorticity fields obscure vortex formation and evolution (unclear due to the negative vortex formation within the recirculating area). Instantaneous values of the Q-field and streamlines around the airfoil are shown in Fig. 6.13 for six times instances within one shedding cycle. The number on the upper right corner of the Q-field plots corresponds to the time indicated with the same number in the force figures (Fig. 6.11). Six different times are selected corresponding to maximums and minimums

drag and lift values. Starting at the time ($t = 0$) where lift and drag correspond to the mean values and advancing in time, an absolute maximum drag is found first (Fig. 6.11a). The wake at this time ($t = 0.18$) shows a maximum vortex growth at the trailing edge (positive vortex) which just started its detaching movement from the airfoil as suggested by the streamlines. A maximum lift (Fig. 6.11b) follows just a few moments after reaching maximum drag. The wake at this time ($t = 0.33$) shows the initial formation of a vortex on the upper side of the airfoil within the shear layer (negative vortex) as well as the downstream motion of the trailing edge vortex. In addition, the downwards deflection of the streamlines around the airfoil is a maximum suggesting maximum circulation and demonstrating the proportionality between lift and circulation. At time $t = 0.53$, a minimum local drag is found as shown in Fig. 6.11c. The wake at this time shows the growing process of the negative vortex as well as a change in the streamlines from downward to slightly upward close to the airfoil. A maximum local drag follows at time $t = 0.70$ (Fig. 6.11d). At this time the wake shows a maximum growth negative vortex in its initial detaching movement. Minimum lift is reached at $t = 0.81$ as shown in Fig. 6.11e. The wake at this time shows the initial formation of a positive vortex at the trailing edge as well as the downstream motion of the detached negative vortex. The streamlines at this time are highly deflected upward, indicating minimum circulation. Finally, absolute minimum drag is reached at $t = 0.91$ as shown in Fig. 6.11f. At this time the wake shows the growth of the positive vortex and a relaxation of the streamlines moving downwards.

Figure 6.11 also reveals that drag fluctuations are driven by skin friction (shear stress) rather than pressure since the streamlines are tangential to the airfoil for maximum drag and more perpendicular for minimum drag. However, variations in lift fluctuations are driven by pressure rather than shear stress since maximum lift is obtained when the streamlines are tangential to the airfoil. This is supported by the maximum lift at the time of initial formation of the upper side vortex (minimum pressure at the

core) and minimum lift after initial formation of the trailing edge vortex. In addition, drag is greater affected by the vortex at the trailing edge than the vortex at the shear layer, since local minimum and maximum values are found when the upper vortex is being shed and absolute minimum and maximum values are found when the trailing edge vortex is being shed.

By observing Figs. 6.11 and 6.13, the role of vortices in the force fluctuations can be sketched as shown in Fig. 6.14. The main purpose of the sketch is to identify the value of the forces with the shape of the wake simultaneously. Figures 6.14a-6.14f show the location of the vortices in the wake and their approximate shape and size within one shedding cycle. The number on the upper right corner corresponds to the time indicated with the same number in the force figures (Fig. 6.14). The model shows how the vortex formation, growth and release affect the force fluctuations. The Δ symbol refers to the incremental value about the mean force. The arrows close to those incremental values of the force in this figure indicate the direction of the force fluctuations about the mean value. Plus and minus signs inside the vortex indicate the sign of the vorticity. Maximum drag (Fig. 6.14a) is found when the trailing vortex reaches it maximum size. Maximum lift (Fig. 6.14b) follows after the trailing edge vortex is detached and the suction side vortex is initially formed within the recirculating area. Then, minimum local drag (Fig. 6.14c) is found when the suction side vortex grows about the half of its maximum size. Subsequently, maximum local drag (Fig. 6.14d) occurs when the suction side vortex reaches its maximum size. Afterwards, an initial trailing edge vortex formation and a release of the suction side vortex cause minimum lift values (Fig. 6.14e). Finally, minimum drag (Fig. 6.14f) is found when the trailing edge vortex grows about the half of its maximum size.

Table 6.1: Mean and standard deviation of tangential and normal force coefficients for *Case 1*. Experimental and theoretical results are shown for the smallest control volume ($52 \times 26mm^2$) considered. Normal and tangential forces refer to the force in the x-direction and in the y-direction respectively

	BEMT	*Poisson*		*Bernoulli*		*Integrated p*	
		Mean	RMS	Mean	RMS	Mean	RMS
C_t	-0.005	-0.001	0.045	0.041	0.026	0.007	0.093
C_n	0.298	0.256	0.106	0.021	0.040	0.252	0.219

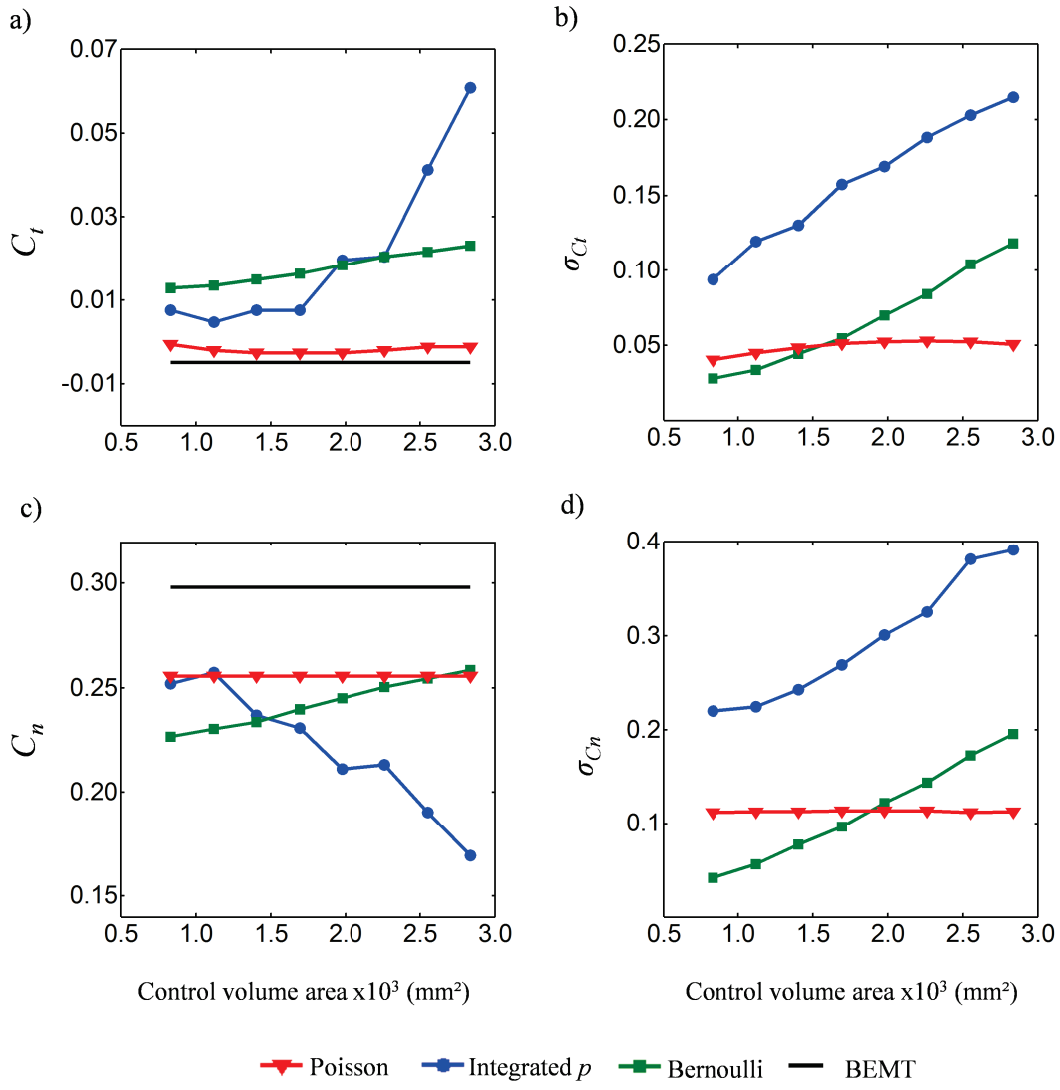

Figure 6.1: Impact of the selected control volume on a) the mean and b) the standard deviation of the tangential force coefficient and on c) the mean and d) the standard deviation of the normal force coefficient for the three methods considered for *Case 1*

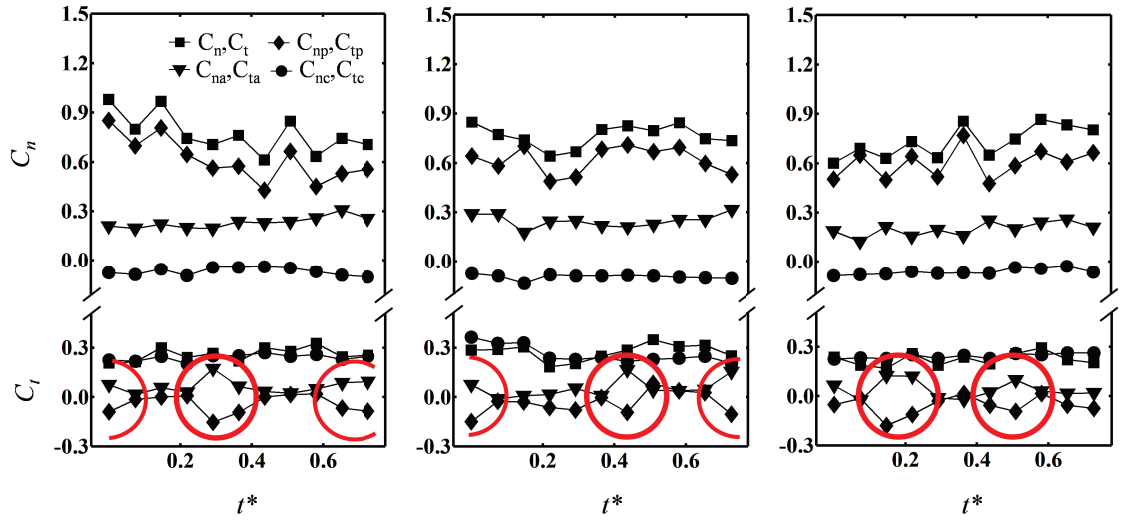

Figure 6.2: Calculated instantaneous forces on the blade shown as a function of time for *Case 2*. These results are for three typical runs and include the normalized instantaneous normal and tangential forces, C_n and C_t. The contribution to the forces from the acceleration, pressure and convective terms are also shown

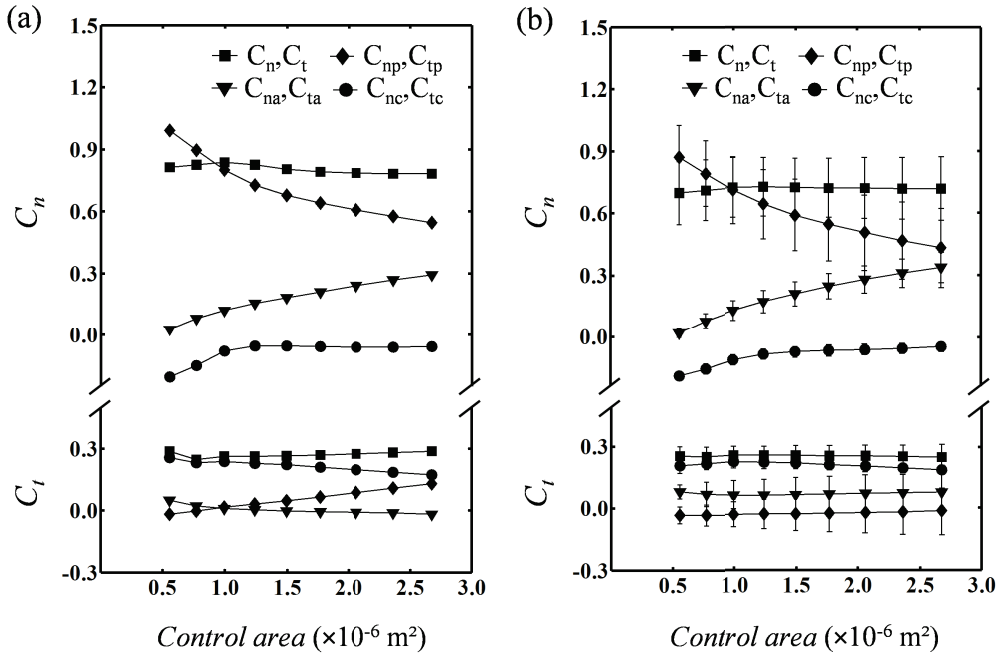

Figure 6.3: Effect of the size of the control volume in the calculation of the instantaneous normal and tangential force coefficients for (a) instantaneous and (b) mean values for *Case 2*. The contribution of each term used in calculating the coefficients is also shown

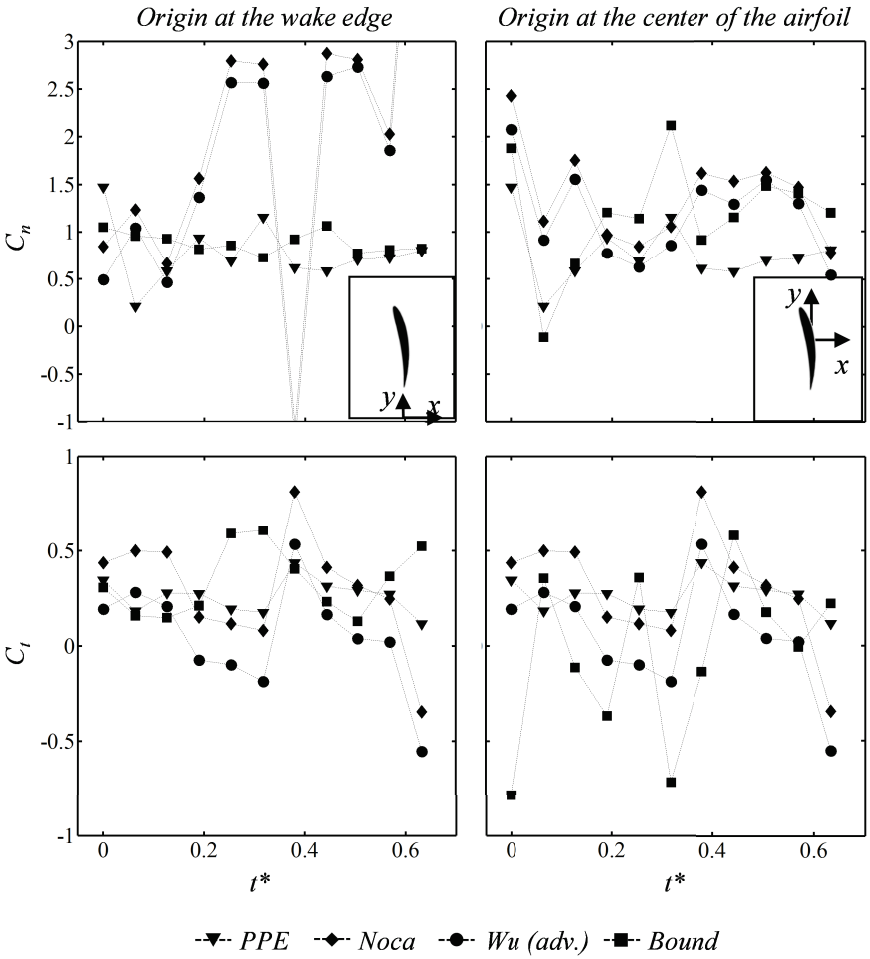

Figure 6.4: Calculated instantaneous forces as a function of time from four different methods as explained in Sec. 2.6 for *Case 2*. The forces are calculated by placing the origin of the coordinates system at both the center of the wake edge and the center of the airfoil. *PPE* stands for pressure Poisson equation, *Noca* for impulse momentum equation, *Wu(adv.)* for the vorticity advection momentum equation and *Bound* for the "flux" momentum equation

Table 6.2: Mean and standard deviation of tangential and normal force coefficients from the raw data for *Case 2*. Experimental and theoretical (*BEMT*) results are shown for the smallest control volume ($52 \times 26mm^2$) considered. The effect of the position of the origin of the coordinate system is analyzed for both center of the airfoil and center of the wake edge of the control volume. Forces are calculated from the four different methods described in Sec. 2.6

Origin at the center of the airfoil

C_t	*BEMT*	*PPE*	*Noca*	*Bound*	*Wu (adv.)*
Mean	0.10	0.26	0.29	-0.04	0.05
RMS	-	0.09	0.30	0.44	0.28
C_n					
Mean	0.65	0.77	1.38	1.18	1.18
RMS	-	0.33	0.49	0.59	0.47

Origin at the center of the wake edge

C_t	*BEMT*	*PPE*	*Noca*	*Bound*	*Wu (adv.)*
Mean	0.10	0.26	0.29	0.34	0.05
RMS	-	0.09	0.30	0.18	0.28
C_n					
Mean	0.65	0.77	2.06	0.88	1.85
RMS	-	0.33	1.80	0.11	1.81

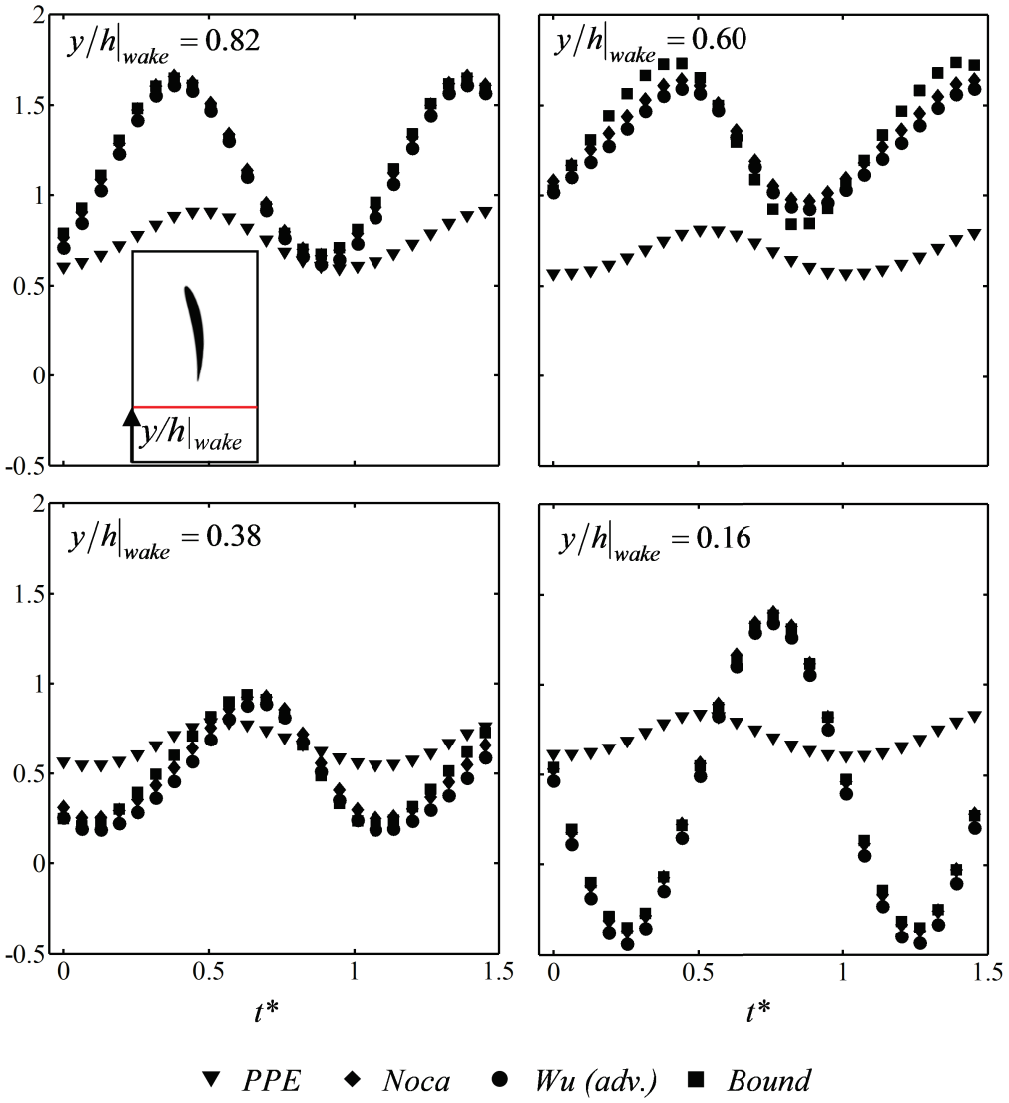

Figure 6.5: Calculated instantaneous normal force coefficient (C_n) as a function of time from POD phase-averaged measurements by using the four methods described in Sec. 2.6 for *Case 2* (The legend is explained in Fig. 6.4). The effect of the size of the control volume is also shown by looking at four different locations of the wake control volume edge $y/h|_{wake}$

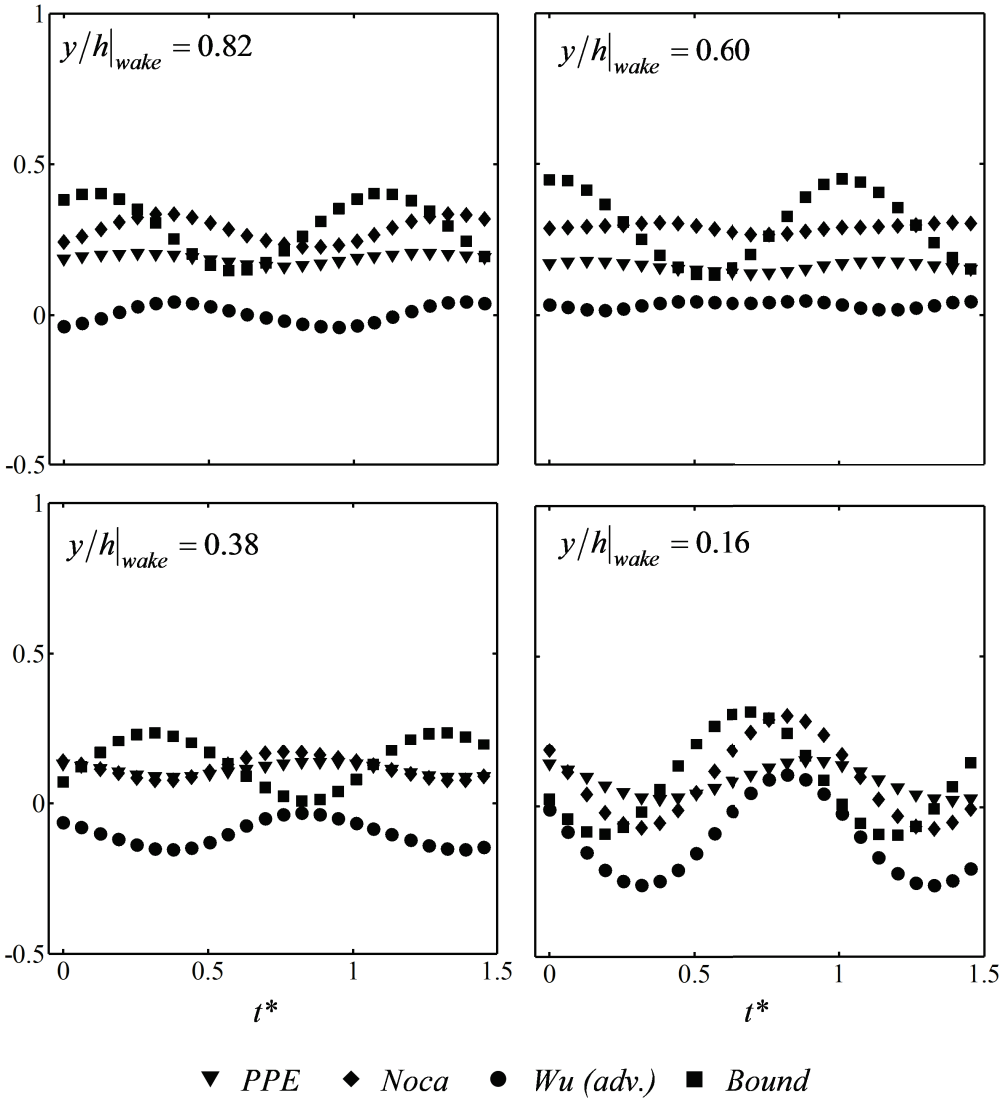

Figure 6.6: Calculated instantaneous tangential force coefficient (C_t) as a function of time from POD phase-averaged measurements by using the four methods described in Sec. 2.6 for *Case 2* (The legend is explained in Fig. 6.4). The effect of the size of the control volume is also shown by looking at four different locations of the wake control volume edge $y/h|_{wake}$

Table 6.3: Mean and semi-amplitude of the tangential and normal force coefficients from POD phase-averaged data for *Case 2*. Experimental and theoretical (*BEMT*) results are shown for the origin of the coordinate system at the center of the airfoil. The effect of the position of the wake control volume edge $y/h|_{wake}$ is also shown. Forces are calculated from the four different methods described in Sec. 2.6

$y/h|_{wake} = 0.82$

C_t	*BEMT*	*PPE*	*Noca*	*Bound*	*Wu (adv.)*
Mean	0.10	0.18	0.28	0.27	0.01
$A/2$	-	0.02	0.05	0.12	0.04
C_n					
Mean	0.65	0.75	1.16	1.16	1.12
$A/2$	-	0.15	0.50	0.49	0.50

$y/h|_{wake} = 0.60$

C_t	*BEMT*	*PPE*	*Noca*	*Bound*	*Wu (adv.)*
Mean	0.10	0.16	0.29	0.29	0.03
$A/2$	-	0.02	0.02	0.16	0.02
C_n					
Mean	0.65	0.69	1.30	1.29	1.26
$A/2$	-	0.12	0.34	0.45	0.33

$y/h|_{wake} = 0.38$

C_t	*BEMT*	*PPE*	*Noca*	*Bound*	*Wu (adv.)*
Mean	0.10	0.11	0.12	0.12	-0.10
$A/2$	-	0.03	0.05	0.12	0.06
C_n					
Mean	0.65	0.67	0.59	0.57	0.54
$A/2$	-	0.12	0.34	0.37	0.35

$y/h|_{wake} = 0.16$

C_t	*BEMT*	*PPE*	*Noca*	*Bound*	*Wu (adv.)*
Mean	0.10	0.09	0.12	0.11	-0.08
$A/2$	-	0.06	0.19	0.20	0.18
C_n					
Mean	0.65	0.72	0.51	0.51	0.45
$A/2$	-	0.11	0.88	0.87	0.89

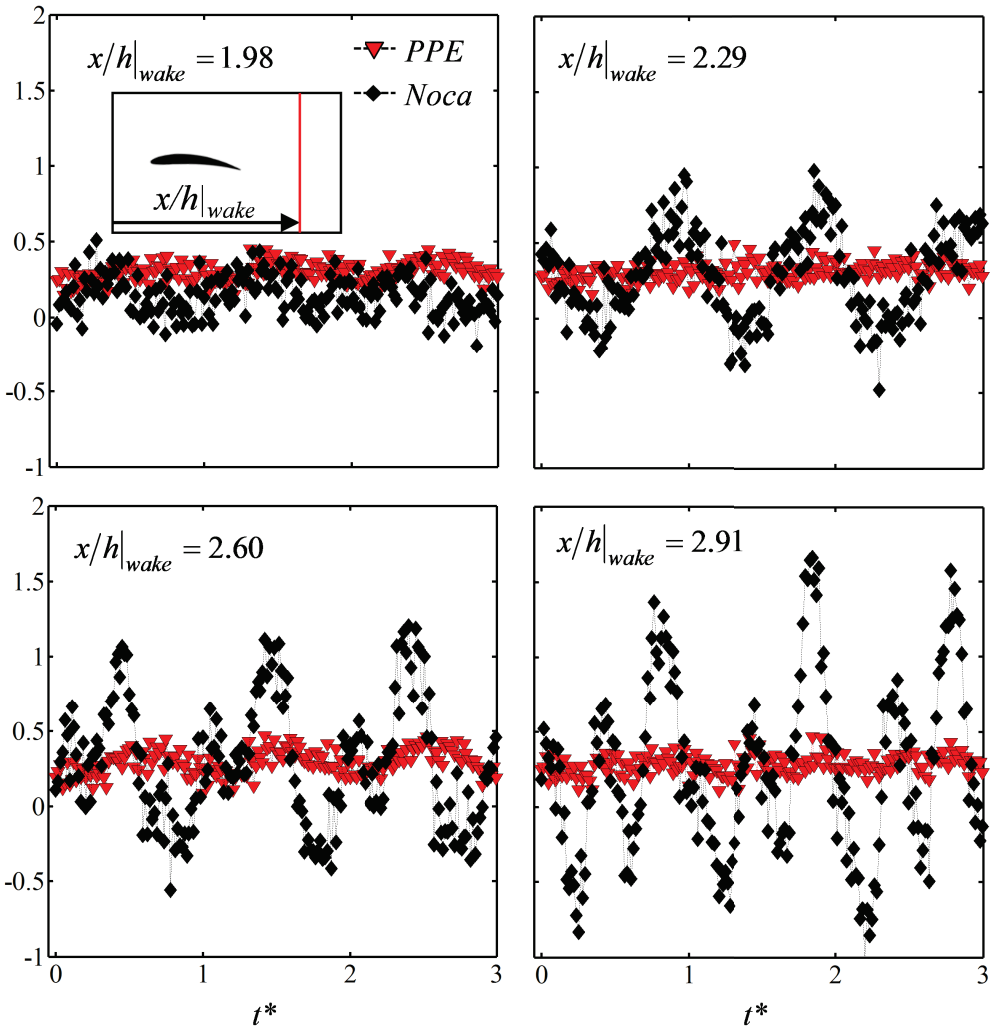

Figure 6.7: Calculated instantaneous lift coefficient (C_l) as a function of time from raw measurements by using the *PPE* and *Noca* methods described in Sec. 2.6 for *Case 3*. The effect of the size of the control volume is also shown by looking at four different locations of the wake control volume edge $x/h|_{wake}$

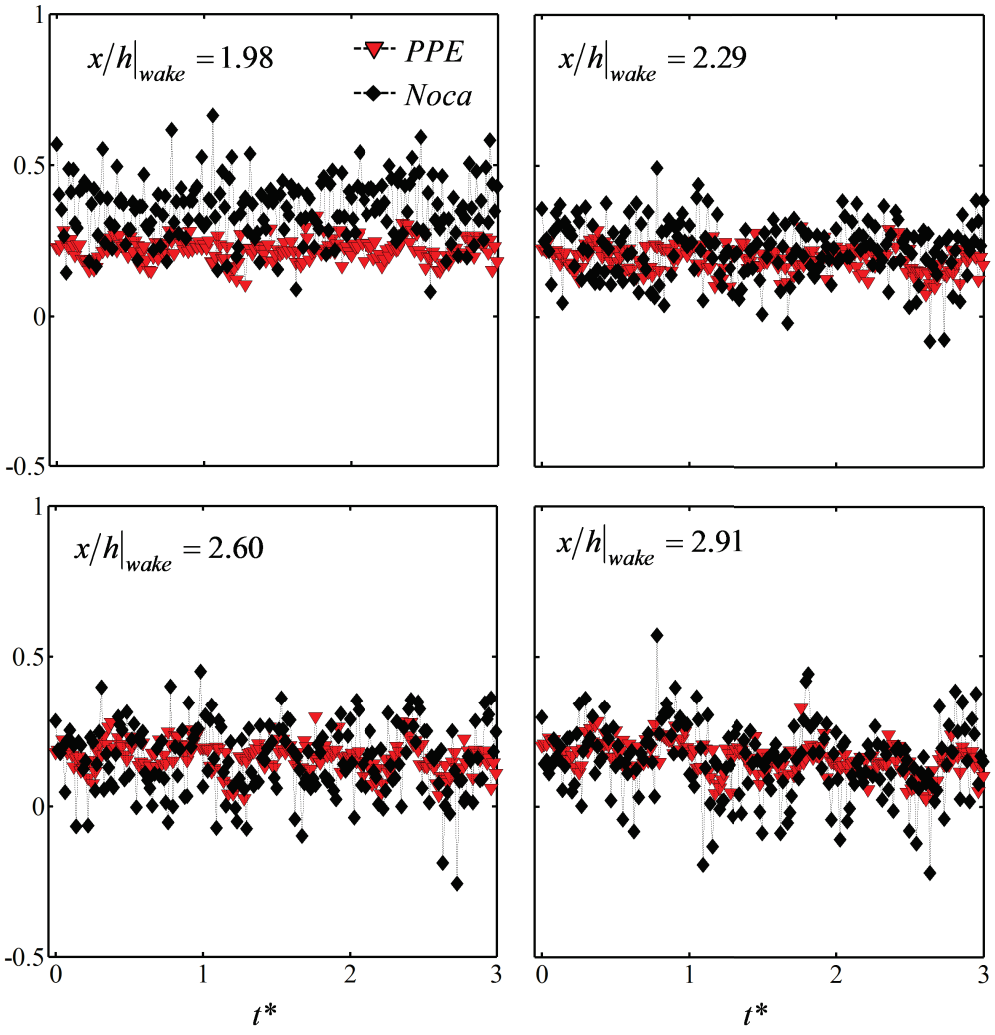

Figure 6.8: Calculated instantaneous drag coefficient (C_d) as a function of time from raw measurements by using the *PPE* and *Noca* methods described in Sec. 2.6 for *Case 3*. The effect of the size of the control volume is also shown by looking at four different locations of the wake control volume edge $x/h|_{wake}$

Table 6.4: Mean and RMS of the lift and drag force coefficients from raw data for *Case 3*. Experimental and theoretical (*XFOIL*) results are shown for the origin of the coordinates system at the center of the airfoil. The effect of the position of the wake control volume edge $x/h|_{wake}$ is also shown. Forces are calculated from the four different methods described in Sec. 2.6

$x/h|_{wake} = 1.98$

C_l	*XFOIL*	*PPE*	*Noca*	*Bound*	*Wu (adv.)*
Mean	0.43	0.30	0.15	0.15	0.22
RMS	-	0.07	0.14	0.12	0.14
C_d					
Mean	0.11	0.20	0.34	0.34	0.27
RMS	-	0.04	0.10	0.13	0.10

$x/h|_{wake} = 2.29$

C_l	*XFOIL*	*PPE*	*Noca*	*Bound*	*Wu (adv.)*
Mean	0.43	0.30	0.28	0.28	0.35
RMS	-	0.06	0.27	0.19	0.28
C_d					
Mean	0.11	0.17	0.19	0.19	0.17
RMS	-	0.04	0.11	0.15	0.10

$x/h|_{wake} = 2.60$

C_l	*XFOIL*	*PPE*	*Noca*	*Bound*	*Wu (adv.)*
Mean	0.43	0.29	0.29	0.29	0.35
RMS	-	0.08	0.38	0.27	0.39
C_d					
Mean	0.11	0.14	0.13	0.12	0.14
RMS	-	0.05	0.11	0.18	0.11

$x/h|_{wake} = 2.91$

C_l	*XFOIL*	*PPE*	*Noca*	*Bound*	*Wu (adv.)*
Mean	0.43	0.28	0.21	0.21	0.28
RMS	-	0.06	0.48	0.42	0.49
C_d					
Mean	0.11	0.13	0.12	0.12	0.14
RMS	-	0.06	0.12	0.25	0.12

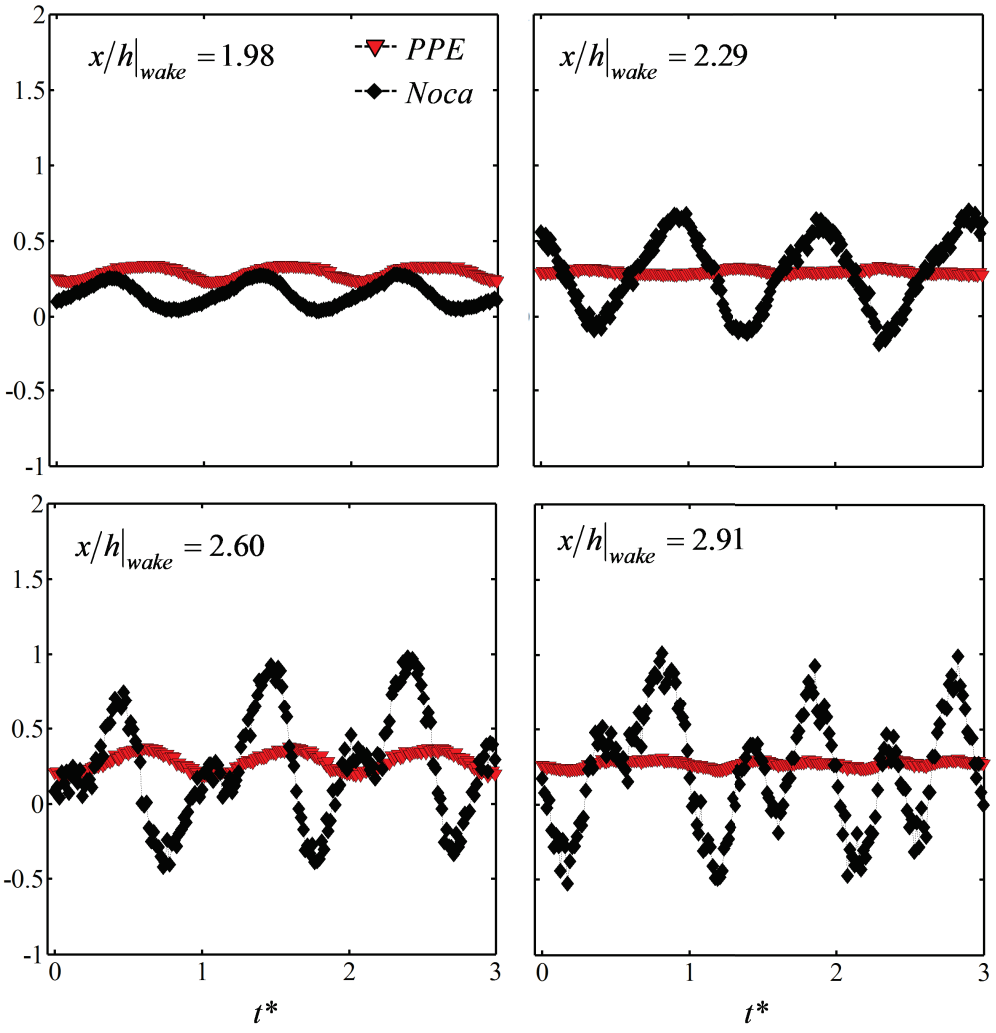

Figure 6.9: Calculated instantaneous lift coefficient (C_l) as a function of time from the 4-modes POD measurements by using the *PPE* and *Noca* methods described in Sec. 2.6 for *Case 3*. The effect of the size of the control volume is also shown by looking at four different locations of the wake control volume edge $x/h|_{wake}$

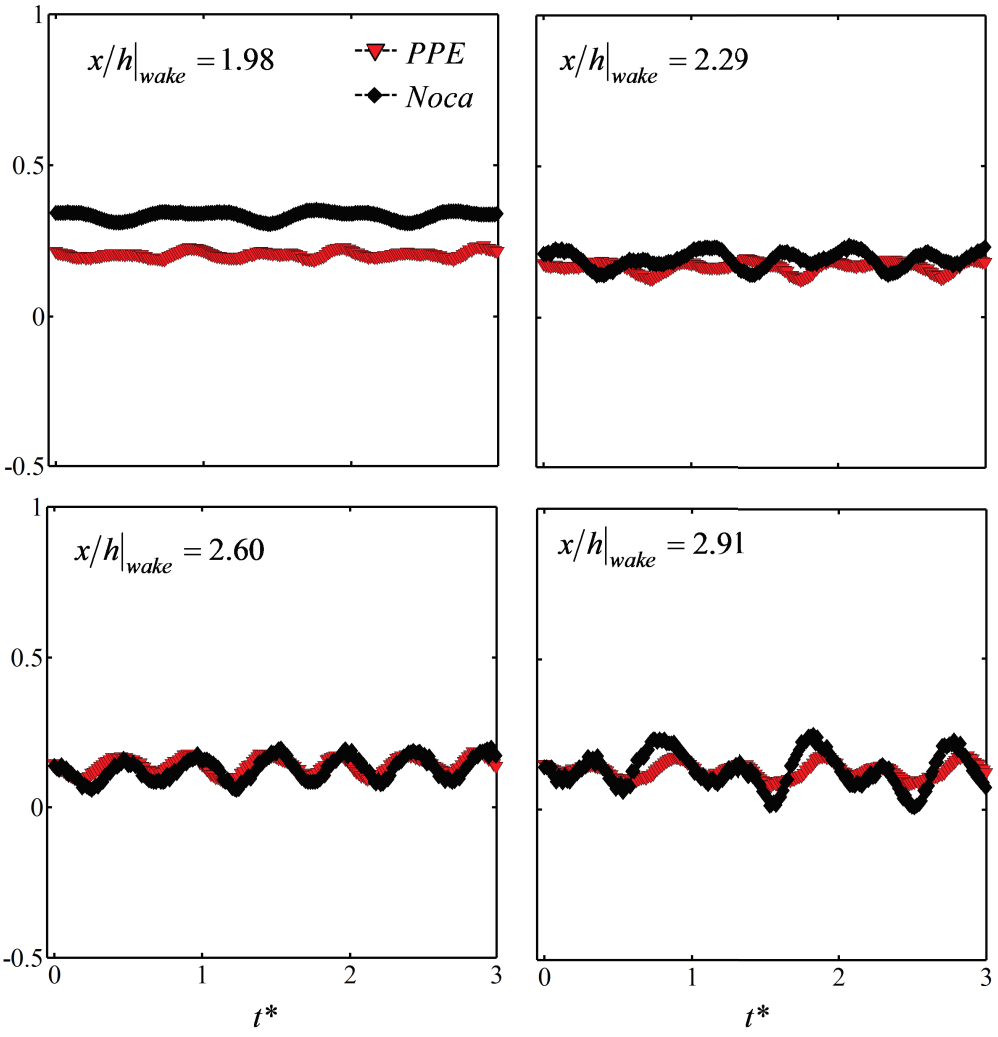

Figure 6.10: Calculated instantaneous drag coefficient (C_d) as a function of time from the 4-modes POD measurements by using the *PPE* and *Noca* methods described in Sec. 2.6 for *Case 3*. The effect of the size of the control volume is also shown by looking at four different locations of the wake control volume edge $x/h|_{wake}$

Table 6.5: Mean and RMS of the lift and drag force coefficients from 4-modes POd data for *Case 3*. Experimental and theoretical (*XFOIL*) results are shown for the origin of the coordinates system at the center of the airfoil. The effect of the position of the wake control volume edge $x/h|_{wake}$ is also shown. Forces are calculated from the four different methods described in Sec. 2.6

$x/h|_{wake} = 1.98$

C_l	*XFOIL*	*PPE*	*Noca*	*Bound*	*Wu (adv.)*
Mean	0.43	0.29	0.15	0.15	0.22
RMS	-	0.03	0.07	0.05	0.08
C_d					
Mean	0.11	0.20	0.33	0.33	0.27
RMS	-	0.01	0.01	0.02	0.01

$x/h|_{wake} = 2.29$

C_l	*XFOIL*	*PPE*	*Noca*	*Bound*	*Wu (adv.)*
Mean	0.43	0.29	0.28	0.28	0.35
RMS	-	0.02	0.25	0.14	0.25
C_d					
Mean	0.11	0.17	0.19	0.19	0.16
RMS	-	0.02	0.03	0.07	0.03

$x/h|_{wake} = 2.60$

C_l	*XFOIL*	*PPE*	*Noca*	*Bound*	*Wu (adv.)*
Mean	0.43	0.28	0.28	0.28	0.35
RMS	-	0.06	0.35	0.24	0.36
C_d					
Mean	0.11	0.14	0.13	0.13	0.14
RMS	-	0.03	0.04	0.11	0.03

$x/h|_{wake} = 2.91$

C_l	*XFOIL*	*PPE*	*Noca*	*Bound*	*Wu (adv.)*
Mean	0.43	0.28	0.20	0.20	0.27
RMS	-	0.02	0.42	0.36	0.42
C_d					
Mean	0.11	0.13	0.12	0.12	0.14
RMS	-	0.02	0.06	0.21	0.04

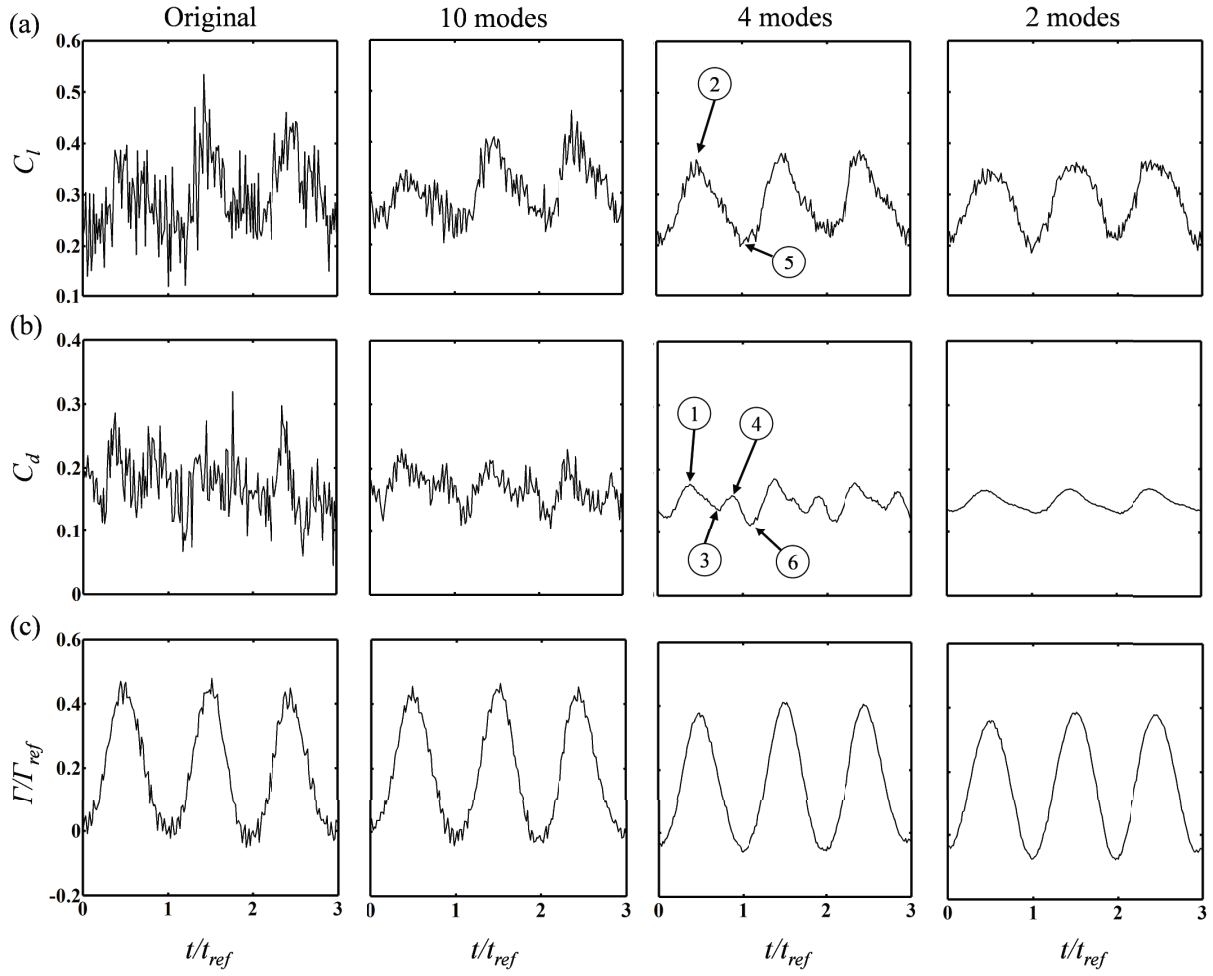

Figure 6.11: Evolution of (a) lift, (b) drag and (c) circulation coefficients obtained from the original velocity field (first column) and modified velocity field from POD by using 10 modes (second column), 4 modes (third column) and 2 modes (fourth column) for *Case 3*

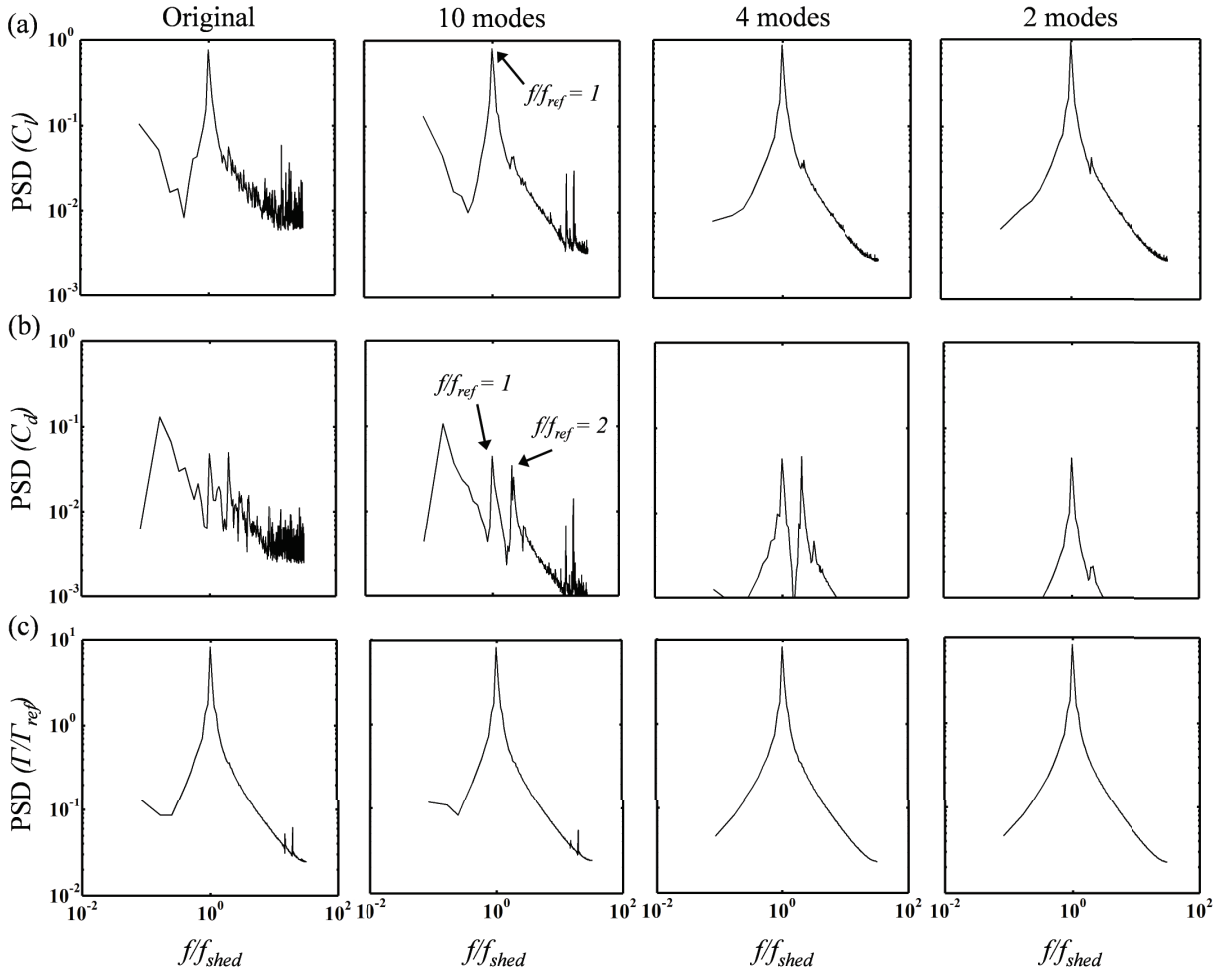

Figure 6.12: Power spectral density of (a) lift, (b) drag and (c) circulation coefficients obtained from the original velocity field (first column) and modified velocity field from POD by using 10 modes (second column), 4 modes (third column) and 2 modes (fourth column) for *Case 3*

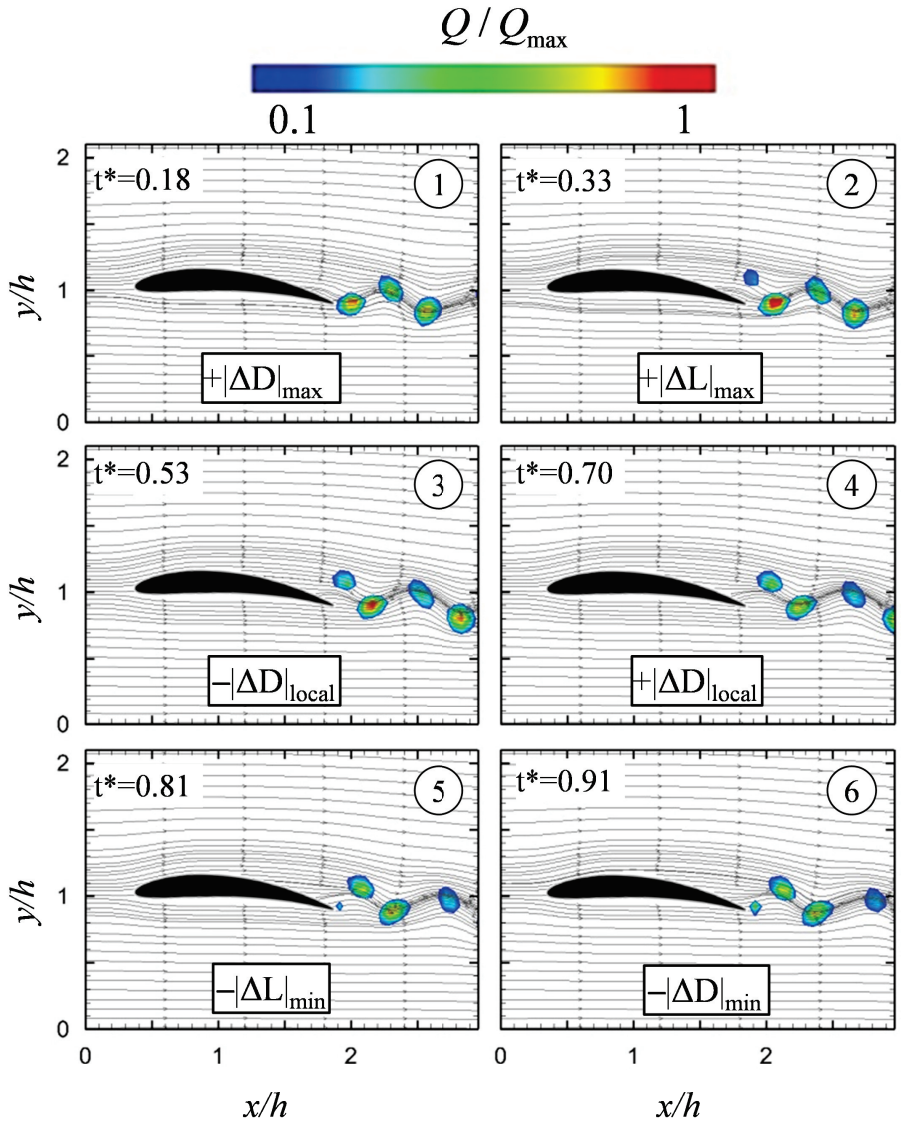

Figure 6.13: Evolution of the Q-field and streamlines within one shedding cycle for (a) absolute maximum drag, (b) maximum lift, (c) local minimum drag, (d) local maximum drag, (e) minimum lift and (f) absolute minimum drag for *Case 3*

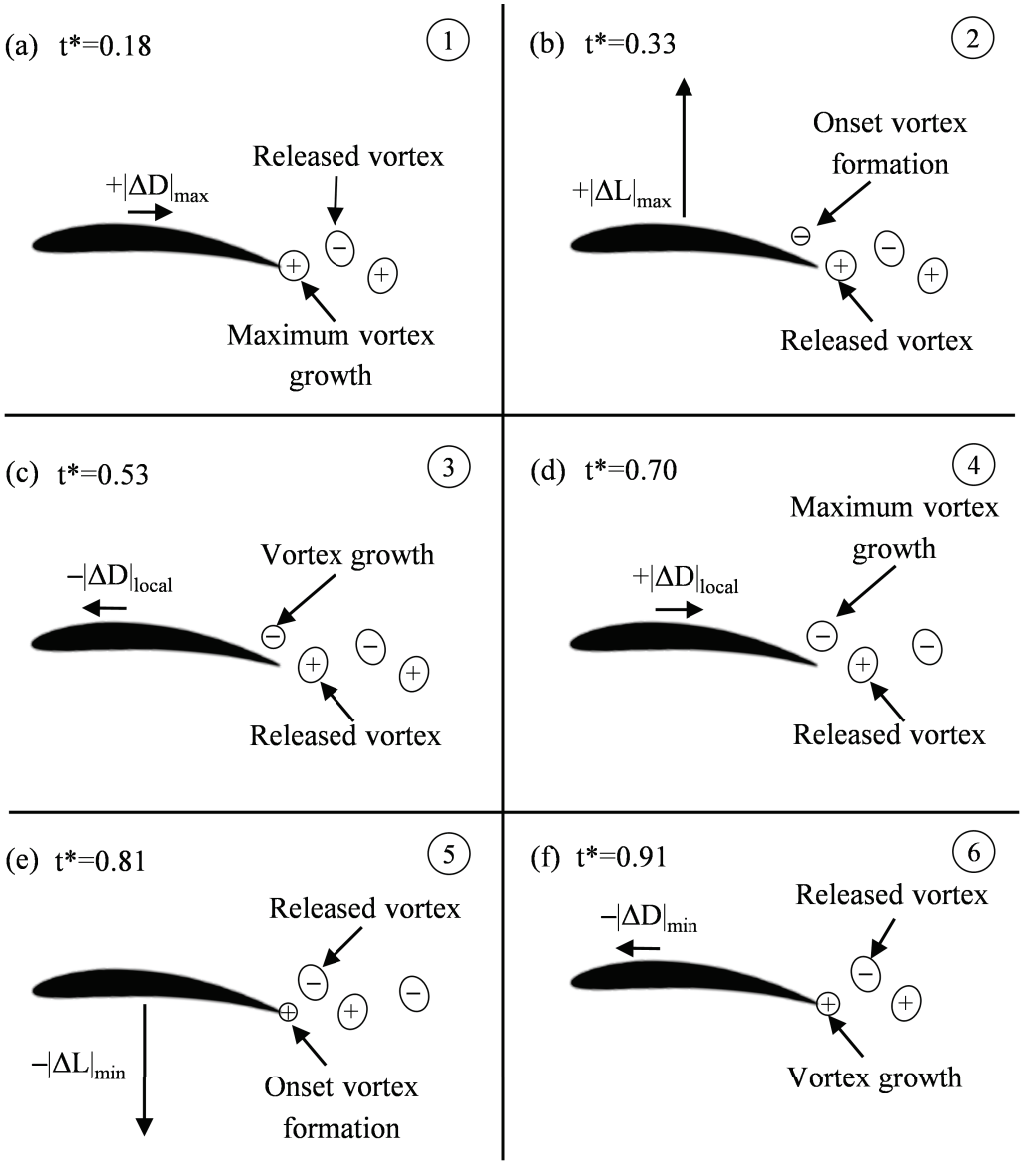

Figure 6.14: Sketch showing the relation between force fluctuations and shape of the wake for one shedding cycle for (a) absolute maximum drag, (b) maximum lift, (c) local minimum drag, (d) local maximum drag, (e) minimum lift and (f) absolute minimum drag for *Case 3*

Chapter 7

Concluding remarks

Aerodynamic unsteady forces in stationary and rotating wings are analyzed in this dissertation by using a combination of TR-PIV and POD techniques. A modified pressure Poisson equation is used to solve for the pressure field. This is needed to resolve the integral conservation of momentum equation. The role of flow structures in force fluctuations is also studied in this manuscript. A POD analysis of the flow is performed to elucidate relations between flow structures and forces in the wing. The main contributions to calculating forces from PIV are summarized next.

Method

1. Development of a new method to calculate the acceleration term in quasi-steady flows for stationary frames of reference from regular (non-time-resolved) PIV. The acceleration is shown to be important in force calculations for stationary frames of reference and cannot be neglected. The method is validated by comparing the pressure obtained in both moving and fixed frames. It is also shown that the acceleration term should not be neglected in unsteady flows when working in neither rotating or moving frames of reference, since it contributes to the total force fluctuations. Therefore, the quasi-steady assumption should not be applied to unsteady flows, even for rotating frames of reference.

2. A modified PPE that includes the continuity equation is developed to solve for the

pressure. If the continuity equation was not satisfied, the PPE would give unrealistic results due to higher error after convergence of the system of equations. This error would result in a larger uncertainty and a non-independence of the calculated forces. In addition, it is shown that the two other techniques used in the past for calculating the pressure field, the Bernoulli equation and the spatially integrated pressure, are not recommended for use with unsteady flows as suggested by the results. The Bernoulli equation fails to include the rotational part of the flow as well as the unsteady term (underestimating the pressure). The integrated pressure method reveals cumulative propagated directional error and is unable to recover the original pressure along the closed path. However, the results suggest that mean pressure values can be obtained using this last technique for a high number of sampled velocity fields.

3. A robust methodology is developed to calculate forces in either stationary or moving wings. The independence of the method with the control volume and origin of the coordinates system selected, demonstrate its robustness when compared to other methodologies described in the past. Frequency, phase, amplitude and mean values of the forces are independent of those parameters. In addition, extensive validation and error analysis show the stability of the method as well as the level of uncertainty for the different cases of study. This also provides a better understanding of the temporal and spatial resolution required to achieve higher accuracy.

Integration PIV-POD analysis

1. A method that combines PIV and POD techniques is used to model time-resolved forces from non-TR-PIV measurements. When temporal resolution is limited, the phase-averaged POD method can be used to create an approximated force function which is continuous in time when just the first two modes of the flow are dominant such as the case of vortex shedding. This hybrid method allows calculating the acceleration term needed in the integral momentum equation for instantaneous force

computations. It resolves the time derivative from to the relation between shedding frequency, time and phase.

2. The integration of POD and PIV is used to accurately calculate force fluctuations. This reveals clearer force behaviors since the calculated raw forces are difficult to interpret. A PSD analysis comparing raw and POD forces shows an almost identical energy content, suggesting that the POD approximation can be used to disclose main flow features and derived parameters.

Force-vortex relations

1. Force fluctuations are due to variations in the wake and the recirculating bubble only. This is shown by the RMS and spectral analysis. Both reveal constant properties of the flow features around the airfoil, except for the wake and the recirculation area where fluctuations are $> 30\%$ (> 3 orders of magnitude in PSD).

2. Evaluation of vorticity and Q fields reveal that vortex grow and formation take the larger part of the full shedding cycle.

3. A spectral analysis of the calculated forces suggests symmetric periodic lift, drag and circulation variations at the shedding frequency. Moreover, lift, drag and circulation signals are in phase, which supports lift-circulation proportionality. However, non-symmetric drag fluctuations are found at double the shedding frequency within a shedding cycle. For instance, when a positive or negative circulation vortex detaches, different values in the maximum and minimum drag are obtained. In addition, slow drag and lift variations at a very low frequency are also disclosed from the spectral analysis. Moreover, two small energy peaks at high frequencies are found most probably due to the Kelvin-Helmoltz instability generated in the separated shear layer.

4. Deflection of streamlines suggest drag fluctuations due to skin friction and lift fluctuations due to pressure. Max and min lift for initial formation of upper and

lower vortex respectively. Absolute min and max drag with trailing edge vortex formation. Relative min and max drag with upper vortex formation.

5. Role of vortices in force variations is also revealed and a model relating force fluctuations with vortex shedding is obtained. Maximum drag is found when the trailing edge vortex reaches its maximum size. Maximum lift follows after the trailing edge vortex is detached and the suction side vortex is initially formed. Minimum local drag is obtained when the size of the suction side vortex is about half of its maximum size. Maximum local drag is found when the suction side vortex reaches its maximum size. Maximum lift occurs after the suction side vortex is detached and the formation of the trialing edge vortex is initiated. Finally, minimum drag is obtained when the size of the trailing edge vortex is about half of its maximum size. These relations can be useful in CFD modeling and flow control.

Bibliography

Abdallah, S. 1987 Numerical solutions for the pressure poisson equation with neumann boundary conditions using a non-staggered grid, i. *Journal of computational physics* **70** (1), 182–192.

Adrian, R. J. 2005 Twenty years of particle image velocimetry. *Experiments in Fluids* **39** (2), 159–169.

Anderson, J. D. 2001 *Fundamentals of aerodynamics*, , vol. 2. McGraw-Hill New York.

Bahaj, A.S., Molland, A.F., Chaplin, J.R. & Batten, W.M.J. 2007 Power and thrust measurements of marine current turbines under various hydrodynamic flow conditions in a cavitation tunnel and a towing tank. *Renewable Energy* **32** (3), 407–426.

Barlow, J. B., Rae, W. H. & Pope, A. 1999 *Low-speed wind tunnel testing*.

Baur, T. & Kngeter, J. 1999 PIV with high temporal resolution for the determination of local pressure reductions from coherent turbulence phenomena. In *3rd International Workshop on Particle Image Velocimetry,(Santa Barbara, CA, USA),(1999-9)*.

Bazilevs, Y., Hsu, M. C., Akkerman, I., Wright, S., Takizawa, K., Henicke, B., Spielman, T. & Tezduyar, T. E. 2011*a* 3D simulation of wind turbine rotors at full scale. part i: geometry modeling and aerodynamics. *International Journal for Numerical Methods in Fluids* **65** (1-3), 207–235.

Bazilevs, Y., Hsu, M. C., Kiendl, J., Wchner, R. & Bletzinger, K. U. 2011*b* 3D simulation of wind turbine rotors at full scale. part II: fluidstructure interaction modeling with composite blades. *International Journal for Numerical Methods in Fluids* **65** (1-3), 236–253.

Berkooz, G., Holmes, P. & Lumley, J. L. 1993 The proper orthogonal decomposition in the analysis of turbulent flows. *Annual review of fluid mechanics* **25** (1), 539–575.

Bevington, P. R. & Robinson, D. K. 1969 *Data reduction and error analysis for the physical sciences*, , vol. 336. McGraw-Hill New York.

Bi, W., Sugii, Y., Okamoto, K. & Madarame, H. 2003 Time-resolved proper orthogonal decomposition of the near-field flow of a round jet measured by dynamic particle image velocimetry. *Measurement Science and Technology* **14** (8), L1.

Bourgoyne, D. A., Ceccio, S. L. & Dowling, D. R. 2005 Vortex shedding from a hydrofoil at high reynolds number. *Journal of Fluid Mechanics* **531**, 293–324.

Boutilier, M. S. H. & Yarusevych, S. 2012 Separated shear layer transition over an airfoil at a low reynolds number. *Physics of Fluids* **24** (8), 084105.

Burton, T. 2011 *Wind energy handbook*. Chichester; New York: Wiley.

Charonko, J. J., King, C. V., Smith, B. L. & Vlachos, P. P. 2010 Assessment of pressure field calculations from particle image velocimetry measurements. *Measurement Science and Technology* **21**, 105401.

Chen, H., Reuss, D. L. & Sick, V. 2012 On the use and interpretation of proper orthogonal decomposition of in-cylinder engine flows. *Measurement Science and Technology* **23** (8), 085302.

Chong, M. S., Perry, A. E. & Cantwell, B. J. 1990 A general classification of three-dimensional flow fields. *Physics of Fluids* **2**, 408–420.

Dong, S., Karniadakis, G. E., Ekmekci, A. & Rockwell, D. 2006 A combined direct numerical simulationparticle image velocimetry study of the turbulent near wake. *Journal of Fluid Mechanics* **569**, 185.

Drela, M. 1989 XFOIL: an analysis and design system for low reynolds number airfoils. In *Low Reynolds number aerodynamics*, pp. 1–12. Springer.

Feng, L., Wang, J. & Pan, C. 2011 Proper orthogonal decomposition analysis of vortex dynamics of a circular cylinder under synthetic jet control. *Physics of Fluids* **23** (1), 014106.

Fitzgerald, E. J. & Mueller, T. J. 1990 Measurements in a separation bubble on an airfoil using laser velocimetry. *AIAA journal* **28** (4), 584–592.

Fujisawa, N., Tanahashi, S. & Srinivas, K. 2005 Evaluation of pressure field and fluid forces on a circular cylinder with and without rotational oscillation using velocity data from PIV measurement. *Measurement Science and Technology* **16**, 989.

Giguere, P. & Selig, M. S. 1999 Design of a tapered and twisted blade for the NREL combined experiment rotor. *NREL/SR* pp. 500–26173.

Glauert, H. 1935 Airplane propellers. *Aerodynamic theory* **4**, 169360.

Graftieaux, L., Michard, M. & Grosjean, N. 2001 Combining PIV, POD and vortex identification algorithms for the study of unsteady turbulent swirling flows. *Measurement Science and Technology* **12** (9), 1422.

Gurka, R., Liberzon, A., Hefetz, D., Rubinstein, D. & Shavit, U. 1999 Computation of pressure distribution using PIV velocity data. In *Workshop on Particle Image Velocimetry*.

Hand, M. M., Simms, D. A., Fingersh, L. J., Jager, D. W., Cotrell, J. R., Schreck, S. & Larwood, S. M. 2001 Unsteady aerodynamics experiment phase vi: Wind tunnel test configurations and available data campaigns. *Tech. Rep.*. NREL/TP-500-29955, National Renewable Energy Lab., Golden, CO.(US).

Hansen, M.O.L., Srensen, J.N., Voutsinas, S., Srensen, N. & Madsen, H.Aa. 2006 State of the art in wind turbine aerodynamics and aeroelasticity. *Progress in Aerospace Sciences* **42** (4), 285–330.

Hart, D. P 2000 PIV error correction. *Experiments in fluids* **29** (1), 13–22.

Holmes, P., Lumley, J. L. & Berkooz, G. 1998 *Turbulence, coherent structures, dynamical systems and symmetry*. Cambridge university press.

Huang, R. F., Wu, J. Y., Jeng, J. H. & Chen, R. C. 2001 Surface flow and vortex shedding of an impulsively started wing. *Journal of Fluid Mechanics* **441**, 265–292.

Hunt, J. C., Wray, A. A. & Moin, P. 1988 Eddies, streams, and convergence zones in turbulent flows. In *Studying Turbulence Using Numerical Simulation Databases, 2*, , vol. 1, pp. 193–208.

Jardin, T., David, L. & Farcy, A. 2009 Characterization of vortical structures and loads based on time-resolved PIV for asymmetric hovering flapping flight. *Experiments in Fluids* **46** (5), 847–857.

Jeong, J. & Hussain, F. 1995 On the identification of a vortex. *Journal of Fluid Mechanics* **285** (69), 69–94.

de Kat, R & Ganapathisubramani, B 2013 Pressure from particle image velocimetry for convective flows: a taylors hypothesis approach. *Measurement Science and Technology* **24** (2), 024002.

de Kat, R. & van Oudheusden, B. W. 2011 Instantaneous planar pressure determination from PIV in turbulent flow. *Experiments in Fluids* **52** (5), 1089–1106.

Kundu, P. K., Cohen, I. M . & Dowling, D. R. 2012 *Fluid mechanics*. Waltham, MA: Academic Press.

Kurtulus, D. F., Scarano, F. & David, L. 2006 Unsteady aerodynamic forces estimation on a square cylinder by TR-PIV. *Experiments in Fluids* **42** (2), 185–196.

Lee, T. & Su, Y. Y. 2012 Low reynolds number airfoil aerodynamic loads determination via line integral of velocity obtained with particle image velocimetry. *Experiments in Fluids* **53** (5), 1177–1190.

Lighthill, J. 1986 An informal introduction to theoretical fluid mechanics .

Lin, J.-C. & Rockwell, D. 1996 Force identification by vorticity fields: techniques based on flow imaging. *Journal of Fluids and Structures* **10** (6), 663–668.

Liu, X. & Katz, J. 2006 Instantaneous pressure and material acceleration measurements using a four-exposure PIV system. *Experiments in Fluids* **41** (2), 227–240.

Lumley, J. L. 1967 The structure of inhomogeneous turbulent flows. *Atmospheric turbulence and radio wave propagation* pp. 166–178.

Mohebbian, A. & Rival, D. E. 2012 Assessment of the derivative-moment transformation method for unsteady-load estimation. *Experiments in Fluids* **53** (2), 319–330.

Murai, Y., Nakada, T., Suzuki, T. & Yamamoto, F. 2007 Particle tracking velocimetry applied to estimate the pressure field around a savonius turbine. *Measurement Science and Technology* **18**, 2491–2503.

Noca, F., Shiels, D. & Jeon, D. 1999 A comparison of methods for evaluating time-dependent fluid dynamic forces on bodies, using only velocity fields and their derivatives. *Journal of Fluids and Structures* **13** (5), 551–578.

Oudheusden, B. W., Scarano, F., Roosenboom, E. W. M., Casimiri, E. W. F. & Souverein, L. J. 2007 Evaluation of integral forces and pressure fields from planar velocimetry data for incompressible and compressible flows. *Experiments in Fluids* **43** (2-3), 153–162.

Oudheusden, B. W. van, Scarano, F., Hinsberg, N. P. van & Watt, D. W. 2005 Phase-resolved characterization of vortex shedding in the near wake of a square-section cylinder at incidence. *Experiments in Fluids* **39** (1), 86–98.

Pope, S. B 2000 *Turbulent flows*. Cambridge university press.

Prandtl, L. & Betz, A. 1927 *Vier abhandlungen zur hydrodynamik und aerodynamik*. Selbstverlag des Kaiser Wilhelm-Instituts fr Strmungsforschung.

Ragni, D., Ashok, A., van Oudheusden, B. W. & Scarano, F. 2009 Surface pressure and aerodynamic loads determination of a transonic airfoil based on particle image velocimetry. *Measurement Science and Technology* **20**, 074005.

Ragni, D., Oudheusden, B. W. & Scarano, F. 2011 3D pressure imaging of an aircraft propeller blade-tip flow by phase-locked stereoscopic PIV. *Experiments in Fluids* **52** (2), 463–477.

Rodriguez, I., Borell, R., Lehmkuhl, O., Perez Segarra, C. D. & Oliva, A. 2011 Direct numerical simulation of the flow over a sphere at re = 3700. *Journal of Fluid Mechanics* **679**, 263–287.

Schmid, P. J., Violato, D. & Scarano, F. 2012 Decomposition of time-resolved tomographic PIV. *Experiments in Fluids* **52** (6), 1567–1579.

Sezer-Uzol, N. & Long, L. N. 2006 3-d time-accurate CFD simulations of wind turbine rotor flow fields. *AIAA paper* **394**.

Shen, W. Z., Mikkelsen, R., Srensen, J. N. & Bak, Christian 2005 Tip loss corrections for wind turbine computations. *Wind Energy* **8** (4), 457–475.

Shenoy, A. R. & Kleinstreuer, C. 2008 Flow over a thin circular disk at low to moderate reynolds numbers. *Journal of Fluid Mechanics* **605**.

Simms, D. A., Schreck, S., Hand, M. M. & Fingersh, L. J. 2001 NREL unsteady aerodynamics experiment in the NASA-Ames wind tunnel: A comparison of predictions to measurements. *Tech. Rep.*. National Renewable Energy Laboratory, Golden, CO.

Sirovich, L. 1987 Turbulence and the dynamics of coherent structures. i-coherent structures. II-Symmetries and transformations. III-Dynamics and scaling. *Quarterly of applied mathematics* **45**, 561–571.

Sotiropoulos, F. & Abdallah, S. 1991 The discrete continuity equation in primitive variable solution of incompresible flow. *Jouurnal of Computational Physics* **95**, 212–227.

Tangler, J. L 2002 Nebulous art of using wind-tunnel airfoil data for predicting rotor performance: Preprint. In *Presented at the 21st ASME Wind Energy Conference, Reno, NV (US), 01/14/200201/17/2002*.

Taylor, J. R. 1997 *An introduction to error analysis: the study of uncertainties in physical measurements*. University science books.

Unal, M. F., Lin, J.-C. & Rockwell, D. 1997 Force prediction by PIV imaging: a momentum-based approach. *Journal of Fluids and Structures* **11** (8), 965–971.

Villegas, A., Cheng, Y., del Campo, V. & Diez, F. J. 2010 Characterization of low reynolds number wind turbine aerodynamics by BEM theory and PIV measurements. In *ASME 2010 3rd Joint US-European Fluids Engineering Summer Meeting*.

Villegas, A & Diez, F. J. 2014*a* Evaluation of unsteady pressure fields and forces in rotating airfoils from time-resolved PIV. *Experiments in Fluids* **55** (4), 1–17.

Villegas, A. & Diez, F. J. 2014*b* On the quasi-instantaneous aerodynamic load and pressure field measurements on turbines by non-intrusive PIV. *Renewable Energy* **63**, 181–193.

Viterna, L. A. & Corrigan, R. D. 1982 Fixed pitch rotor performance of large horizontal axis wind turbines. *Large Horizontal-Axis Wind Turbines* **1**, 69–85.

Wang, S., Zhang, X., He, G. & Liu, T. 2013 A lift formula applied to low-reynolds-number unsteady flows. *Physics of Fluids* **25** (9), 093605.

Westerweel, J. 1997 Fundamentals of digital particle image velocimetry. *Measurement Science and Technology* **8**, 1379.

Wu, J. C. 1981 Theory for aerodynamic force and moment in viscous flows. *AIAA Journal* **19** (4), 432–441.

Wu, J.-Z., Lu, X.-Y. & Zhuang, L.-X. 2007 Integral force acting on a body due to local flow structures. *Journal of Fluid Mechanics* **576**, 265.

Wu, J. Z., Pan, Z. L. & Lu, X. Y. 2005 Unsteady fluid-dynamic force solely in terms of control-surface integral. *Physics of Fluids* **17** (9), 098102.

Yarusevych, S., Sullivan, P. E. & Kawall, J. G. 2006 Coherent structures in an airfoil boundary layer and wake at low reynolds numbers. *Physics of Fluids* **18** (4), 044101.

Yarusevych, S., Sullivan, P. E. & Kawall, J. G. 2009 On vortex shedding from an airfoil in low-reynolds-number flows. *Journal of Fluid Mechanics* **632**, 245.

Appendix A

Frames of reference

The reason for the differences observed in the unsteady accelerations between the two reference frames can be explained more intuitively from the velocity field images in Fig. A.1. For comparison purposes a point A is shown in both reference frames. In Fig. A.1a the point is fixed with respect to the inertial frame and in A.1b is fix with respect to the rotating frame. Clearly, in Fig. A.1a Point A changes velocities between times t_1 and t_2 as the rotor moves up in the field of view. In the other hand, in Fig. A.1b the velocity of point A remains constant between t_1 and t_2 as it moves with the reference frame fix in the blade. This shows the importance of the unsteady term in the inertial frame. Mathematically, this difference is shown by Eq. 2.1 which relates the acceleration in inertial and non-inertial frames. Considering that the velocity between both frames can be related by $\vec{u} = \vec{u}' + \vec{\Omega} \times \vec{r}'$, the terms in Eq. 2.1 can now be grouped and simplified at the time both coordinate systems are coincident. The result can be written in Cartesian coordinates as

$$\begin{aligned} \frac{\partial u}{\partial t} &= -\Omega \left({r_z}' \frac{\partial u'}{\partial y'} - {r_y}' \frac{\partial u'}{\partial z'} \right) \\ \frac{\partial v}{\partial t} &= -\Omega \left({r_z}' \frac{\partial v'}{\partial y'} - {r_y}' \frac{\partial v'}{\partial z'} \right) \\ \frac{\partial w}{\partial t} &= -\Omega \left({r_z}' \frac{\partial w'}{\partial y'} - {r_y}' \frac{\partial w'}{\partial z'} \right) \end{aligned} \tag{A.1}$$

where $\vec{r}' =< {r_x}', {r_y}', {r_z}' >$ is the position vector. Both sides of this expression can be experimentally evaluated and compared as shown in Fig. A.2. The acceleration term is calculated using the terms from the right hand side of Eq. A.1 $\partial \bar{u}/\partial t|_{Derived}$

in Fig. A.2a, and also calculated directly from PIV measurements $\partial\bar{u}/\partial t|_{PIV}$ in Fig. A.2b. Both Figs. A.2a and A.2b are in good agreement. It can also be shown that the pressure is an invariant of the coordinate system used. For instance, Fig. A.3 shows the mean pressure field around the airfoil calculated in a fixed reference frame and in a moving reference frame. The good agreement between both contour plots verifies this invariant identity.

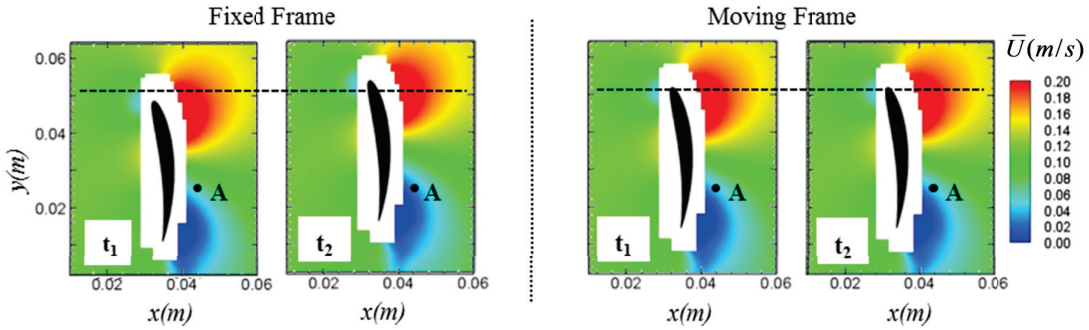

Figure A.1: Contour plot of the instantaneous axial velocity field around the rotating airfoil showing the rotor and a point A a) in a laboratory reference frame and b) in a moving frame. In a) the point changes velocities between times t_1 and t_2 as the rotor moves up in the field of view. In b) the velocity of point A remains constant between t_1 and t_2 as it moves with the reference frame fix in the blade.

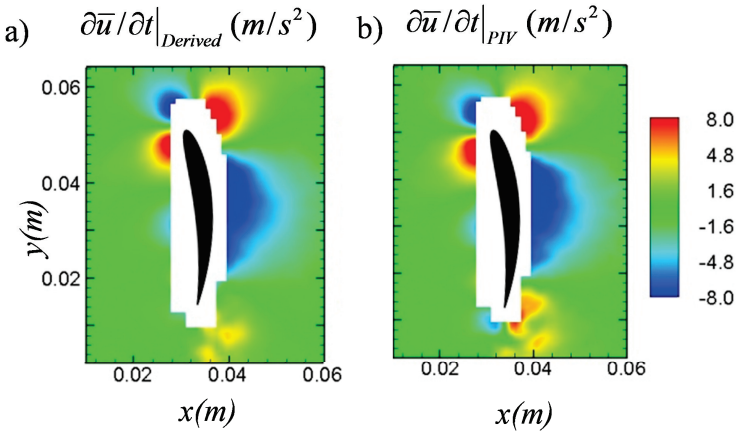

Figure A.2: Mean acceleration a) derived from Eq. A.1 and b) measured from PIV results

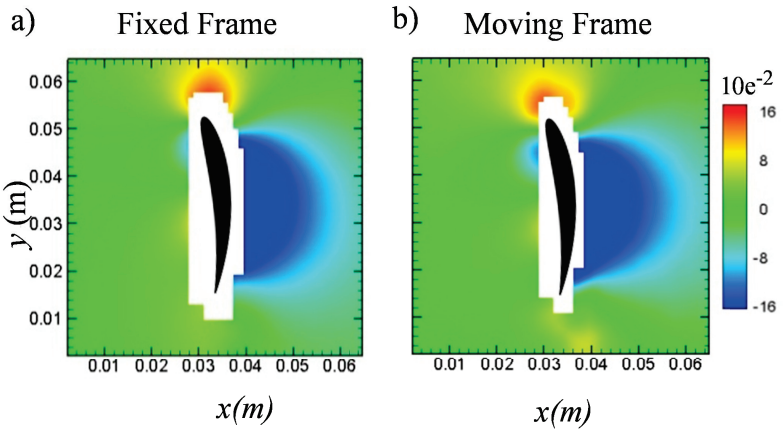

Figure A.3: Contour plot of the mean pressure field around the airfoil calculated a) in a fixed reference frame and b) in a moving reference frame